A study on Electron Beam Melted Ti-6Al-4V

Safdar, Adnan

2012

[Link to publication](#)

Citation for published version (APA):
Safdar, A. (2012). *A study on Electron Beam Melted Ti-6Al-4V*. [Doctoral Thesis (compilation), Solid Mechanics]. Lund University.

Total number of authors:
1

A Study on Electron Beam Melted Ti-6Al-4V

Adnan Safdar

Division of Solid Mechanics

Department of Construction Sciences

Faculty of Engineering, Lund University,
Lund, Sweden.
June 2012

School of Technology & Society

Malmö University

Dedicated

to the biggest inspiration of my life

my father

Prof. Dr. Safdar Ali Kayani (late)

Acknowledgments

Abstract

The work presented in this dissertation is concerned with the microstructures and surface roughness of test slabs of Ti-6Al-4V produced by one of powder based Additive Manufacturing (AM) technique namely electron beam melting (EBM). The effects of process parameters of a EBM system and geometry factors of a EBM build such as slabs' thickness and height etc. on the microstructure and the surface roughness of the EBM produced Ti-6Al-4V have been investigated. The processing parameters of the EBM system include beam current, scan speed, offset focus and scanning length. In this study three different batches of samples were prepared. Microstructures of EBM built Ti-6Al-4V were studied using optical microscopy (OM), scanning electron microscopy (SEM), transmission electron microscopy (TEM), and X-ray diffraction (XRD). Confocal microscopy (CM) and image analysis codes ImageJ's routine SurfCharJ were used to quantify the surface roughness of the test slabs. The microstructures of EBM built Ti-6Al-4V in general consist of columnar grains of prior β phase. Inside the columnar grains there is a typical ($\alpha+\beta$) microstructure of titanium alloys containing Widmanstätten α platelets and rod-shaped β phase. Grain boundary (α_{GB}) layer has also been observed on the grain boundaries of prior β columnar grains. By using TEM, the β phase in EBM built Ti-6Al-4V has been identified as a rod-like structure located on the grain boundaries of the fine α grains and they often grow along the build direction. The size of the β rods is about 200 nm and the distance between the β rods is ranged between 0.5-2 μm. Chemical compositions for different phases have been measured by TEM/EDX and volume fraction of the β phase in the EBM Ti-6Al-4V has been determined to be 2.7%. The phase transformation sequence in EBM built Ti-6Al-4V has been discussed according to processing history and microstructures observed. It has been observed that, the size, number and geometry of prior β columnar grain depend on the sample thickness and other process parameters setting. The diameter of columnar grain varies between 2-70 μm. The increase in size, number and regularity of columnar grains has been observed with increase in sample thickness, beam energy density and the scanning length. While with increase in height of the build it decreases. The length and smoothness of α platelets increases with increase in diameter of prior β columnar grain. The β phase rods are unaffected by sample thickness and process parameter settings. The sample thickness and beam energy density has a strong effect on the surface roughness of the test slabs. The value of surface roughness coefficient R_a for different test slabs varies between 1-20 μm. It is observed that the surface roughness of the test slab increases with increase in thickness of the slab and beam energy density. Response surface methodology is applied to model the effect of process parameter on surface roughness of EBM parts. Phase field modelling approach has been successfully applied to study the microstructure development in EBM built Ti-6Al-4V.

Paper A:

A. Safdar, L-Y. Wei, A. Snis, Z. Lai

Evaluation of Microstructural Development in Electron Beam Melted Ti-6Al-4V

Paper B:

A. Safdar, H.Z. He, L-Y Wei, A. Snis, Luis E. Chavez de Paz

Effect of Process Parameters Settings and Thickness on Surface Roughness of EBM Produced Ti-6Al-4V

Paper C:

A. Safdar, L-Y Wei, H.Z. He, A. Snis,

Effect of Process Parameters Settings and Thickness on Microstructures of EBM Produced Ti-6Al-4V

Manuscript form

Paper D:

A. Safdar, P. Ståhle, M. Fisk,

Phase field modelling of phase transformation in electron beam melted Ti-6Al-4V

Manuscript form

Contents

1. Introduction:

Mechanical properties such as low density, excellent high temperature mechanical properties and good corrosion resistance in almost all environments make titanium and its alloys the material of choice in high performance industries. Although titanium and its alloys were first developed and studied extensively by the aerospace industry, they have found applications in other industries requiring high performance materials such as power generation plants, heat exchangers, automotive, naval and offshore petroleum and gas exploration. Aerospace industry consumes about 70% of the world's titanium production for aero engine components such as casings, compressor blades and rotors (A. Suáreza, 2011). Non industrial applications of Titanium alloys includes fashion Jewelry and sports goods manufacturing industries where light weight and sufficient strengths are of major interest like tennis racquets, golf clubs and racing bicycles etc. Although titanium is not a rare metal but, the high cost of processing titanium metal (Lutjering, 2003) has limited its application to selected industries.

Titanium and its alloys have also found applications in biomedical applications as hard tissue replacement due to excellent biocompatibility, specific strength and corrosion resistance (Niinomi, 1998). In comparison to other metallic materials like stainless steel and Co-Cr alloys, better biocompatibility is the result of instant formation of TiO_2 layer resulting in high corrosion resistance and low toxicity in fluid body environment (S. Ponader, 2007).

Among all the titanium alloys, Ti-6Al-4V is by far the most commonly used titanium alloy accounting for 50% to 70 % of total titanium output in the world (A. Suáreza, 2011; L. Zeng, 2005). It is a two phase $(\alpha + \beta)$ alloy. The microstructures of Ti-6Al-4V are processing history and heat treatment dependent (Lutjering, 1998). The mechanical properties of Ti-6Al-4V show strong dependence on the metallurgical microstructures. The control of texture and microstructures is necessary to control the physical and mechanical properties of Ti-6Al-4V (L. Zeng, 2005). Due to the presence of two phases and transformation between two phases provides an opportunity to prepare functional parts with tailor made combination of microstructures and properties.

The extensive use of Ti and its alloys especially Ti-6Al-4V, in many industries like aerospace, where reliability and functionality of the components are of major interest, requires better understanding of the process and procedures by which these components are fabricated. The high cost of raw material also requires the processes that are cost and material efficient, in order to keep the final price of the components affordable.

Over the past two to three decades, many solid freeform fabrication techniques have been investigated to fabricate fully dense and near net shape metal parts for a variety of applications, in a way that material efficiency and lead-time are improved, targeting reductions in the cost of fabrication and lead-time compared to conventional methods. Direct digital manufacturing (DDM) is the next embodiment of solid free form fabrication (SFF), additive manufacturing (AM) or rapid prototyping (RP). The basic concept behind all additive manufacturing techniques is to take mass produced raw materials, and through the use of an innovative processing technique, generate a finished component minimizing the use of specialized or dedicated tools. In comparison to conventional methods all the DDM methods have the advantage of reduced material waste, shorter lead times, and minimum or zero tooling cost (S.S. AL-BERMANI, 2010). AM process provides an

opportunity to build complex geometries like downward facing surfaces and functional parts as single unit, avoiding machining and welding etc. (Cormier, et al., 2004). The free form nature of the AM methods attracts the application in addition to conventional industries like medical implant, energy and aerospace, as well as in fields such as sports goods, modern art sculptures and fashion jewelry manufacturing.

The results presented in this dissertation are part of my Ph.D. studies conducted at Division of Materials Sciences at Malmö University between Oct 2007 and April 2012. The main focus of the study is to evaluate the microstructures of Ti-6Al-4V produced by one of AM method namely Electron Beam Melting (EBM). The effect of different process parameter setting on microstructures and surface roughness of EBM produced Ti-6Al-4V were also studied. Phase field modeling approach has been used to simulate the phase transformation sequences in EBM built Ti-6Al-4V.

This dissertation present background and introduction of titanium and its alloys - especially Ti-6Al-4V- in chapter 2. Chapter 3 provides an overview of AM method EBM. Chapter 4 elaborates the different experimental and numerical methods used in this study. In chapter 5 summaries of work performed and results obtained during the study has been presented.

During this study three different batches of samples (Build-I, Build-II and Build-III) were prepared and microstructures of EBM built Ti-6Al-4V were studied using standard equipment like Optical Microscope (OM), Scanning Electron Microscope (SEM), Transmission Electron Microscope (TEM), and X-ray diffraction (XRD). Surface roughness of the samples was studied using Confocal Microscope (CM). Image analysis codes were used for the quantification of roughness coefficients and surface response methodology was used to model the effect of process parameters on surface roughness of the produced parts. Phase field modeling approach is implemented in an attempt to simulate the microstructural development in the process.

Chapter 2

Titanium and its Alloys

This chapter provides an overview of Titanium metal and its alloys, physical metallurgy and applications.

2.1 Titanium:

Titanium (Ti) is a nonferrous light transition metal with silver metallic appearance. Its atomic number is 22 and atomic weight is 47.90. The crystal structures and crystal parameters of α and β phases of titanium are illustrated in Fig. 2.1.1 (Lutjering, 2003). It is present in earth crust at a level of about 0.6% and hence is the fourth most abundant structural metal after aluminium (Al), iron (Fe) and magnesium (Mg). Titanium usually occurs in mineral sands containing ilmenite ($FeTiO_3$) and rutile (TiO_2) (Lutjering, 2003). Pure titanium undergoes an allotropic transformation from hexagonal closed packed (HCP) α phase to body centered cubic (BCC) β phase at temperature of 882 ± 2 ^{o}C known as β transus temperature. The exact transformation temperature is strongly influenced by the purity of the metal. The transformation from β phase to α phase depends upon the cooling rates. For rapid cooling the transformation is martensitic, while fro slow cooling rates it is diffusion based nucleation and growth process.

Selected physical and thermal properties are given in Table 2.1.1.
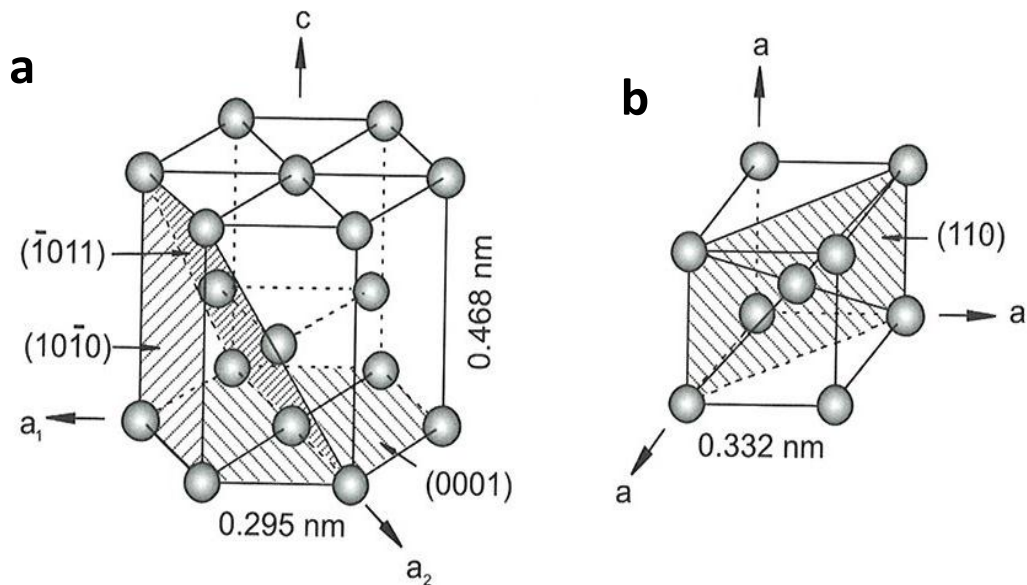
Figure 2.1.1: Unit cells of a) α phase Ti,   b) β phase Ti. (Lutjering, 2003)

Table: 2.1.1: Selected room temperature physical and thermal properties of Ti (Lutjering, 2003)

Property	
Density	4500 kg/ m^3
Isotopes	^{46}Ti, ^{47}Ti **^{48}Ti** ^{49}Ti ^{50}Ti
Melting temperature	1670 ^{o}C
Boiling temperature	3287 ^{o}C
Specific Heat Capacity	0.54 J/ g. K
Thermal Conductivity	21.9 W/ m K
Electrical resistivity	56 $\mu\Omega$ cm
Young's Modulus	116 GPa
Vickers Hardness	970 MPa

2.2 Alloys of Titanium:

The β transus temperature of the pure Ti can be adjusted by addition of alloying elements. The alloying elements which raise the β transus temperature are known as α stabilizers. While the alloying elements that reduces the β transus temperature are known as β stabilizers. Primary α stabilizer element includes aluminium (Al), oxygen (O) and Nitrogen (N), while β stabilizer elements are vanadium (V), niobium (Nb), and molybdenum (Mo). In some alloys both α and β phases are present concurrently, in contrast to only one phase at room temperature. Hence Titanium alloys are categorized in three groups as α, β and ($\alpha + \beta$) alloys depending upon the type and amount of alloying elements. If alloyed with α stabilizer then it is categorized as an α alloy while in case of a β stabilizer alloying element, it is categorized as a β alloy. Some elements like zirconium (Zr) and silicon (Si) are also alloyed to improve the mechanical properties rather than to affect the β transus temperature or room temperature microstructures. The effect of some common alloying elements and their stabilizing effect on β transus temperature is presented in Fig. 2.2.1 and Table 2.2.1, while different alloys and respective β transus temperatures are listed in Table 2.2.2.

2.2.1 α Alloys:

Pure titanium and its alloys with non-transitional metals elements like aluminium (Al), tin (Sn) and oxygen (O) etc. are categorized as α alloys. In the alloys the stabilizers can either be alloyed individual or in combination of more than one element. The room temperature crystal structures of an α alloy are HCP. α alloys are normally associated with reduced ductility, high creep resistance and high density. α alloys are mainly used in chemical and process engineering industries due to better creep properties and corrosion resistance. α alloys exhibits comparatively lower specific strength.
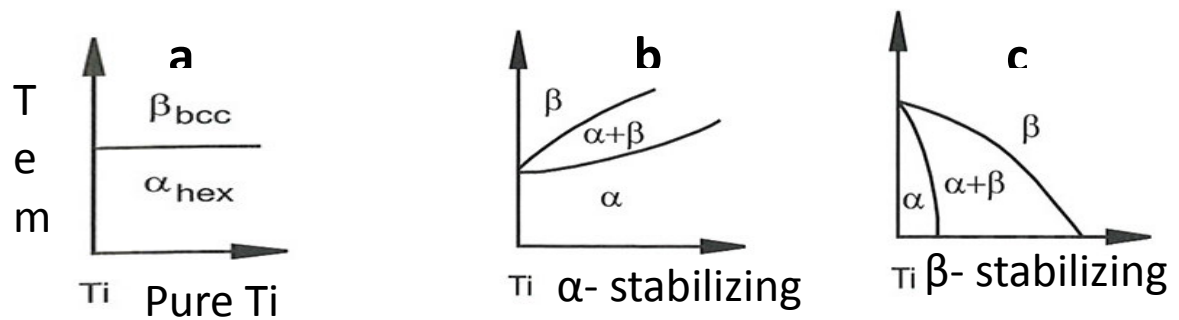
Figure 2.2.1: Influence of alloying element on β transus temperature (Lutjering, 2003).

Table 2.2.1: Common alloying elements and their Stabilizing effects

Alloying Element	Range (wt%)	Stabilizer
Aluminium	2-7	α
Tin	2-6	α
Vanadium	2-20	β (15% to obtain room temperature β phase (Lutjering, 2003)
Molybdenum	2-20	β (10% to obtain room temperature β phase (Lutjering, 2003)
Zirconium	2-8	Strengthening of both phases
Silicon	0.2-1	Improve creep resistance

Table 2.2.2: Commercial titanium alloys

Category	Alloy with composition	β-Transus Temperature ^{o}C (Lutjering, 2003)
α	Ti-0.2 Pd	915
α	Ti-0.3Mo-0.8 Ni	880
α	Ti-5Al-2.5Sn	1040
β	Ti-10V-2Fe-3Al	800
β	Ti-13V-11Cr-3Al	700
β	Ti-3Al-8V-6Cr-4Mo-4Zr	730
α+ β	Ti-6Al-4V	995
α+ β	Ti-6Al-4V ELI	975
α+ β	Ti-6Al-1V-1Mo	1040
α+ β	Ti-6Al-6V-2sn	945

2.2.2 β Alloys:

When Titanium is alloyed with transition metals like vanadium (V), niobium (Nb) and molybdenum (Mo), the alloys are categorized as β alloys. β alloys are normally associated with higher strength and lower ductility and corrosion resistance as compared with α alloys. The use of β alloys is very limited but is steadily increasing in the applications where high yield strength and low modulus of elasticity are of major interest like springs etc.

2.2.3 α+β Alloys:

The alloys which contain one or more α stabilizing element together with one or more β stabilizing elements, and the room temperature microstructures are combination of both phases, are categorized as $(\alpha + \beta)$ alloys. The amount of each phase depends upon the amount of respective stabilizing element. $(\alpha + \beta)$ alloys provides an opportunity to have properties in between the α and β alloys. Ti-6Al-4V is the currently most used alloy. This alloy has exceptionally good balance of strength, ductility, fatigue and fracture properties but has limitation of usage in environments where maximum temperature is about 300 $^{\circ}$C (Lutjering, 2003).

2.3 Ti-6Al-4V:

Ti-6Al-4V falls in the category of $(\alpha + \beta)$ alloys. It was developed in 1950 at Illinois Institute of Technology USA. It is by far the most commonly used and extensively studied titanium alloys (A. Suáreza, 2011; Lutjering, 2003). Some physical mechanical and thermal properties of Ti-6Al-4V are listed in Table 2.3.1. A vertical section of phase diagram for titanium alloys of Ti-6AL-xV (x is wt%) is presented in figure 2.3.1 (M. Peters, 2003).

The microstructures of titanium alloys are primarily described by the amount and arrangement of α and β phases. The room temperature microstructures consist mainly of HCP α phase and some retained BCC β phase. The microstructures and mechanical properties of $(\alpha + \beta)$ Ti alloys depend upon the processing history and heat treatment (Lutjering, 1998). Thus the final equilibrium state microstructures can be categorized in to different groups depending upon the cooling rate and thermal processing history e.g. grain boundary allotriomorph α, globular or primary α, Widmanstätten α platelets, transformed β phase, and possibly martensitic α' phase. For slow cooling rates from above β transus temperature, the β phase transforms in to globular type of α. In the case of moderate to high cooling rates the prior β phase transforms in to α platelets growing from grain boundary of prior β grain to the inside of grain. The length and thickness of the platelets is determined by the cooling rate (Lutjering, 2003). In the case of rapid cooling (quenching) with cooling rate above the 410 $^{\circ}$C /s (T. Ahmed, 1998) the prior β phase transformes in to the martensitic α'phase. In Ti-6Al-4V, the martensitic phase is either HCP α' phase or orthorhombic α'' phase depending upon the composition of the β phase before quenching. HCP α' phase is enriched in β stabilizing element. The ageing in the range between the β transus and martensitic start temperature (Ms) results in decomposition of the HCP α' martensitic phase in to equilibrium α and β phases. Ageing at about 700 $^{\circ}$C for about thirty minutes will fully decompose the α' phase in to the equilibrium α and β phases (F.X. Gil

Mur, 1996). Fig. 2.3.2 represents the different microstructures resulting from different cooling rates (M. Peters, 2003).

Table 2.3.1: Some physical properties of Ti-6Al-4V (Lutjering, 2003; Lutjering, 1999)

β-Transus Temperature	995 ±5 ^{o}C
Density	4500 Kg / m^{3}
Melting Temperature	1604-1660 ^{o}C
Linear thermal expansion coefficient	9.0 x 10^{-6} K^{-1}
Thermal Conductivity	7 W m^{-1} K^{-1}
Specific heat capacity	0.530 J g^{-1} K^{-1}
Electrical Resistivity	1.67 μ Ω m
Tensile Strength	900-1200 MPa
Young's Modulus	950 MPa
Elastic Modulus	115 GPa
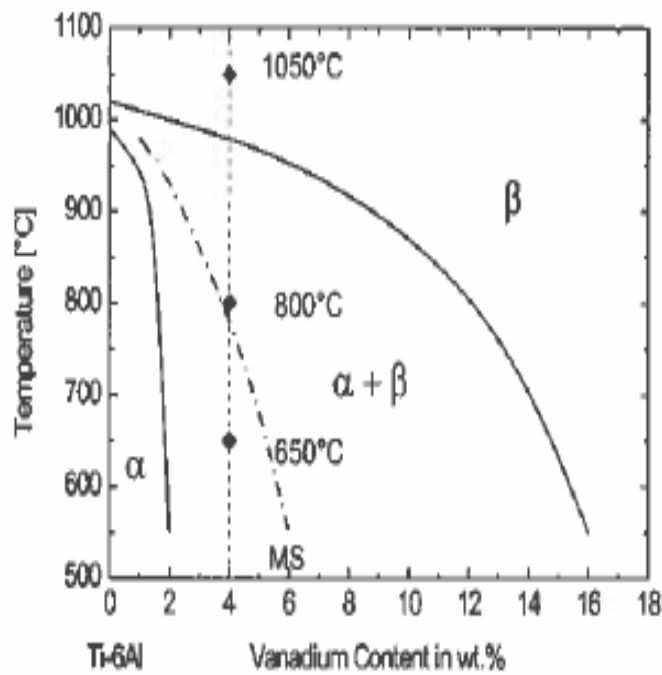
Figure 2.3.1: Vertical section of phase diagram for Ti alloys of type Ti-6AL-xV (M. Peters, 2003)
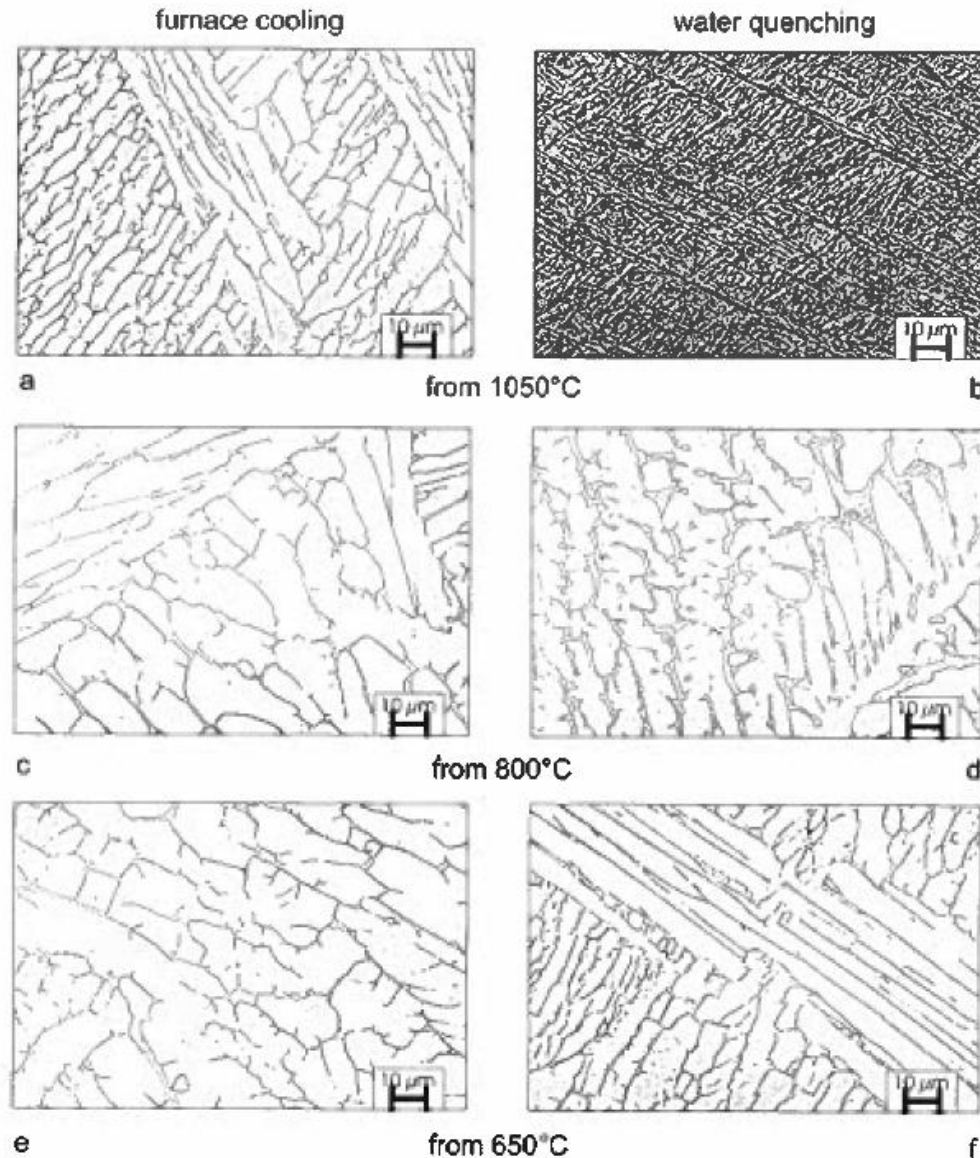
Figure 2.3.2: Microstructures of Ti-6Al-4V after slow cooling (50 $^{\circ}$C /h) and water quenching from 1050 $^{\circ}$C, 800 $^{\circ}$C and 650 $^{\circ}$C (M. Peters, 2003).

2.4 Applications of Ti Alloys:

The low density, excellent high temperature mechanical properties and good corrosion resistance of titanium alloys have led to a diversified range of successful applications for the demanding performance and reliability requirements of the aerospace, naval, medical, petrochemical, nuclear and power generation industries. (A. Suáreza, 2011). In addition to high performance industries titanium alloys also found application in jewelry, and sports goods manufacturing. Table 2.4.1 provides a list of industrial and other uses of titanium and its alloys.

Table 2.4.1: Application of Titanium alloys in different industries.

Industry	Application
Aerospace	Gas Turbine engines, Airframe
Chemical process & power generation industry	Heat Exchanger, Containers, Petrochemical industry, Steam turbine blades
Marine & offshore Applications	Offshore petroleum & gas exploration
Medical Implants	Hip and dental implants
Sports and Leisure	Golf club head, Tennis rackets, Jewelry etc

Chapter 3
Direct Digital Manufacturing (DDM)

The high performance engineering alloys used in aerospace, biomedical and other industrial application are typically accompanied by high price tag. Conventional methods used for fabrication metallic components include wrought or cast forgings and ingots. In conventional fabrication methods it is very difficult to obtain a complex functional part as single geometric unit, thus requiring the joining of two or more parts by welding etc. During the final step of fabrication different types of precision and multiaxis CNC machining is also required in order to obtain required geometry of the functional part. These sorts of methods involved a lot of mostly non-recyclable waste of about 85% (S.M. Gaytan, 2009).

Over the past three decades many solid free form fabrication (SFF) techniques have been investigated to fabricate high performance alloys by focusing reduction in cost and waste materials. Direct digital manufacturing (DDM) is the next embodiment of solid free form fabrication (SFF), additive manufacturing (AM) or rapid prototyping (RP). Different DDM techniques include direct light fabrication (DLF), LASER engineering net shape (LENS), direct LASER deposition (DLD) and electron beam melting (EBM). First model of SFF or additive manufacturing was patented in 1986 by Charles Deckard (Deckard, 1986).

The basic concept behind all additive manufacturing methods is to take mass produced raw material, and through the use of an innovative processing technique, generate a finished component minimizing the use of specialized or dedicated tools. In comparison to conventional methods all the DDM methods have the advantage of reduced material waste, shorter lead times, and minimum or zero tooling cost and most importantly high component complexity (S.S. AL-BERMANI, 2010). One of the advantages of AM process is the possibility to build complex geometries like downward facing surfaces and complex functional parts as single unit, avoiding machining and welding etc (Cormier, et al., 2004).

Majority of the DDM/ AM techniques like DLD, SMD and LENS etc. uses LASER as power source to melt the metallic powder or wire. For optical energy such as a LASER beam, the reflectance for metals at room temperature is very high. Thus, quite a sufficient portion of the incidence energy, up to 65% (S.S. AL-BERMANI, 2010) is reflected out of the melt pool and lost to the atmosphere. This prohibits some reflective materials from being effectively deposited with a LASER, hence reducing the material coupling efficiency of the process. The power spectrum limitation of LASER based systems also makes its use limited to materials with relatively low melting temperatures.

3.1 Electron Beam Melting (EBM):

Arcam, founded in 1997, has developed a unique DDM/ AM technology for direct digital manufacturing of fully dense or near net shape parts from metal powder. The EBM technology has the ability to build dense parts with similar or better properties to any wrought method. The EBM process is fully computer controlled automatic system with no human interaction during the build process. The EBM systems are highly power efficient

(Cormier, et al., 2004), and the high vacuum in the build chamber provides oxygen free environment which ensures the purity of material in the part and precise geometry. EBM process possess high coupling efficiency with deposited materials and thus applicable to many materials including highly reflective materials such as aluminum (Cormier, et al., 2004). The wide range of power spectrum of an electron beam, in principle makes possible to melt every metal irrespective of the melting temperature.

EBM system's technical data is presented in table 3.1.1. The EBM system consists of an electron beam generating system (Electron Gun), a build chamber and a computer system to control the whole process (Fig. 3.1.1a). Fig 3.1.1 (b) illustrates schematically key components of the EBM system. Electron Gun generates an electron beam, which is focused by focusing lenses. The motion of the electron beam on the built table is controlled by the deflection coils.

A beam of high energy electrons is produced in the electron gun when a current is passed through a tungsten filament. This causes the filament to heat up and emit electrons. The power of the beam is controlled by the current in the filament. A $60\,kV$ accelerating voltage is applied to the anode beneath the electrode, thus accelerating the emitted electrons in the desired direction with velocities ranging from 0.1 to 0.4 times the velocity of light. This beam is focused by the combination of electrostatic and electro-magnetic lenses on to the build table with power density of up to $100\,kW/cm^2$ (S.S. AL-BERMANI, 2010; L.E. Murr, 2009). The vacuum level inside the electron gun is approximately $1x10^{-6}\,mbar$ to prevent scattering of the electron beam due to collisions with gas atoms. During the whole build, the sharply focused electron beam scans the build table with controllable speed known as scan speed. The beam current and scan speed are carefully chosen in such a way that sufficient heat is generated to melt the powder. The interaction between electrons in the beam and the powder surface in the building tank, results in X-rays emission. The steel chamber walls and leaded glass view ports are designed to contain these X-ray emissions inside the build chamber.

The buildup process starts with a 3-dimensional Computer Aided Design (CAD) model. This model is sliced into thin layers of $100\,\mu m$. The system physically reproduces the computer slices layer by layer, by melting the metal powder. During the buildup process an approximately $100\,\mu m$ thin layer of powder is spread over the build table by fetching the powder from the containers. The build table is made of a stainless steel plate. This helps to remove the built part from the build table as, during cooling, the interface between the base plate and component becomes brittle and thermal mismatch stresses enable parts to be easily removed manually. The motion of electron beam is controlled by deflection coils according to the CAD file. When the electrons collide with metal atoms in the powder bed, their velocity is decreased. In doing so, their kinetic energy is converted into thermal energy. This results in melting and fusing of the metal powder. After successful melting of one layer the build table is lowered according to the thickness of next layer. A new layer of powder is then spread over the lowered table and already built part. The scanning process is repeated and powder is melted. The same sequence is repeated
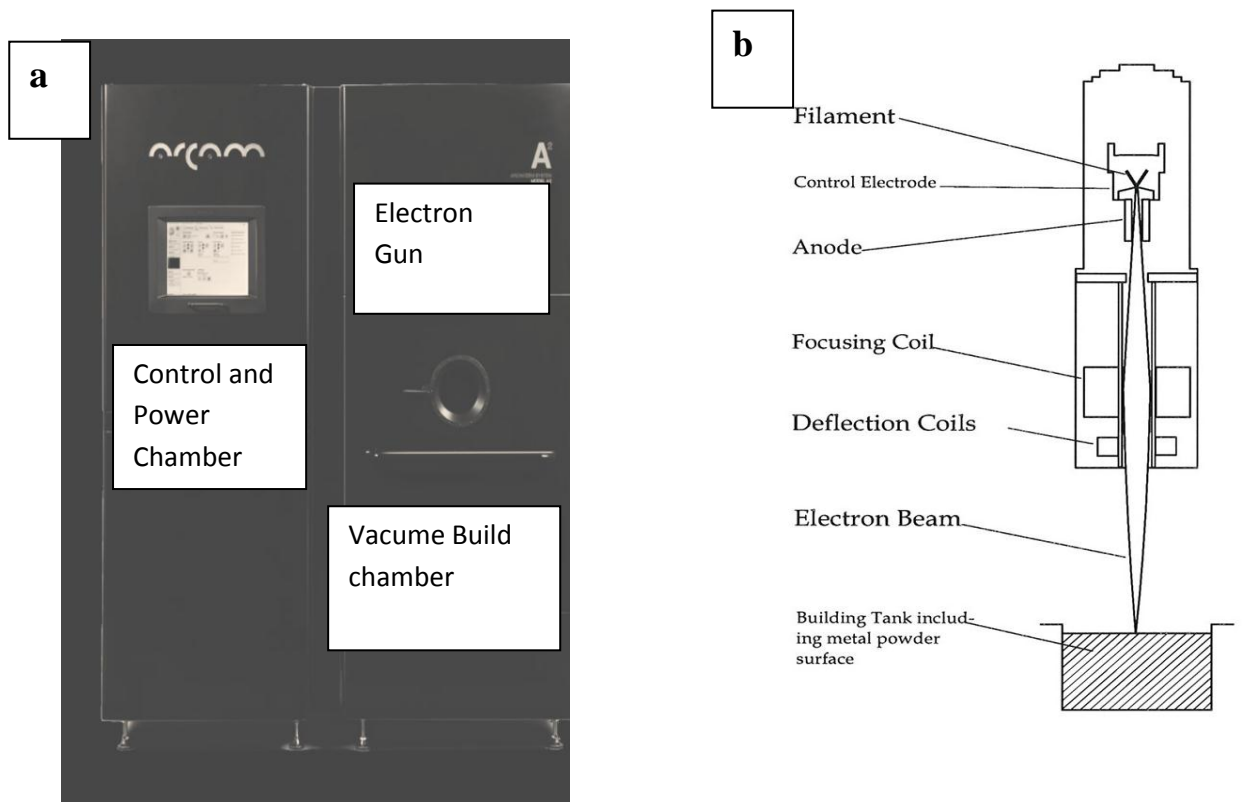
Figure 3.1.1: a) EBM system A2 (Arcam, 2008) , b) schematic representation of EBM System components (Operational Manual, 2008)

Table 3.1.1: Technical data of Arcam's EBM system (Arcam, 2008)

Parameter / Model	Arcam A1	Arcam A2
Max build Size	200 x 200 x 180mm (w x d x h)	200x200x300mm (w x d x h) and 300 x 200 mm Ø (Two replaceable chambers)
Size and Weight	1850x900x2200 mm, 1420 Kg	1850x900x2200 mm, 1420 Kg
Power supply	3 x 400 V, 32 A, 7KW	3 x 400 V, 32 A, 7KW
Accuracy of the part	$\pm$ 0.2 mm	$\pm$ 0.025 mm
Beam Power	50-3000 W	50-3000 W
Beam size	0.2 – 1.0 mm	0.2 – 1.0 mm
No of beams spot	Up to 100	Up to 100
Build rate	55/ 80 cm^3/h (for Ti-6Al-4V)	
Scan speed	Up to 8000 m/ sec	Up to 8000 m/ sec
Cooling	Active	Automatic
Process computer	PC	PC
Certification	CE	CE

until the build is finished. During the whole duration of built up, the build chamber and power bed is kept at elevated temperature of about $700 + 25\,^oC$ by pre- heating sequence before final melting. This isothermal hold during the build has two advantages i.e. a relatively high temperature in build chamber improves the build rate and secondly it caters the needs of annealing.

In EBM systems each component/ part is built in two steps. Firstly the outer part or boundary is melted and is referred to as "Contour" (Fig. 3.1.2). The contour provides an interface between the actual build and the surrounding powder. Contour melting also provides an opportunity to have good surface structure. In the second step of melting the actual part is built within the contours. This part is normally referred to as "Squares" (Fig. 3.1.2).

EBM process is a complex procedure depending upon different processing parameter of the system, ranging from beam power and beam size to scan speed and scanning direction. The final microstructures of EBM built Ti-6Al-4V or any material are the result of complex combination of different processing parameters of the system. There is a possibility to obtain somewhat different microstructures in EBM built Ti-6Al-4V parts built with different sets of processing parameters. This is possible due to the fact that different sets of processing parameters provide somewhat different built environments and cooling conditions.
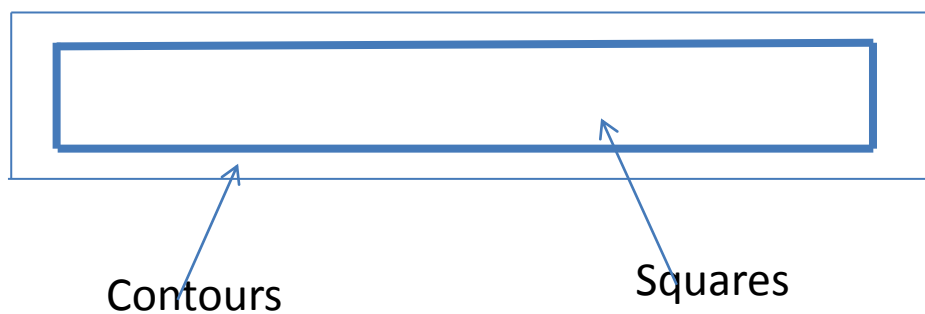
Figure 3.1.2: Schematic illustration of EBM build.

Chapter 4

Experimental and Numerical Methods

During the course of this work many experimental and numerical methods has been utilized. The microstructure evaluation has been performed by optical and electron microscopy. EDX methods have been used for quantitative compositional analysis. Numerical methods such as response surface methodology and phase field theory have been used for modelling of surface roughness and microstructural evolution respectively.

In this section a brief introduction of instruments and numerical methods has been presented.

4.1 Scanning Electron Microscopy (SEM):

SEM is one of the most versatile instruments available for examination and analysis of microstructural characteristics in the field of materials sciences. The SEM images the sample surface by scanning it with a high-energy beam of electrons. A typical electron microscope consists of many parts including electron gun, electromagnetic lenses and electron detecting systems. The electron gun thermionically emits a beam of electron from usually a tungsten filament that is focused by the electromagnetic lenses to very fine size (of the order of nanometer). This focused beam then interact with the surface of sample and generates different signals which are collected and processed by different detecting systems to generate a representative image on computer screen.

The interaction of a sample surface and focused beam results in two types of electrons emitted from the samples namely secondary electron (SEs) and backscattered electrons (BSEs). SEs are normally electrons with low energy ($< 50\ ev$). These electrons are generated as a result of beam interaction with weakly bounded outer shells of atoms in the surface of samples. SE images (SEIs) are normally of high resolutions. On the other hand BSEs are produced by scattering of the primary electron beam. The number of BSEs increases with increase in atomic number of the target surface. Due to this dependence the BSE image is a useful tool to distinguish between different atomic species in the sample on the basis of brightness in the image. As the BSEs escape from the larger volume then SEs, the imaging resolution is generally lower then of SEIs.

The microstructures and different phases present of the test slabs of all builds were studied using, EVOLS10 Environmental Scanning Electron Microscope (ESEM) operating at 20KV.

4.2 Transmission Electron Microscopy (TEM):

The transmission electron microscope is used to characterize the microstructure of materials with very high spatial resolution. Information about the morphology, crystal structure and defects, crystal phases and composition, and microstructure can be obtained. The transmission electron microscope uses a high energy electron beam transmitted through a very thin sample to image and analyze the microstructure of materials with atomic scale resolution. The electrons are focused with electromagnetic lenses and the image is observed

on a fluorescent screen in back focal plane of objective lens. The electrons are accelerated at several hundred kV, giving wavelengths much smaller than that of light. However, whereas the resolution of the optical microscope is limited by the wavelength of light, that of the electron microscope is limited by aberrations inherent in electromagnetic lenses.

When a focused high energy electron beam passes through the thin sample foil some of electrons are diffracted and some pass through directly to form diffraction spots on fluorescent screen. TEM in materials science is used for both imaging and obtaining diffraction patterns of crystalline materials. Two types of diffraction patterns namely selected area electron diffraction (SAED) and convergent beam electron diffraction (CBED) are obtained from TEM. SAED is obtained by allowing diffracted electrons from selected area of the sample to pass through an aperture to form diffraction spots on back focal plane of objective lens.

Image formation in TEM can be done either by diffracted beam or direct beam. TEM imaging is of two types namely bright field image and dark field image. Bright field image is obtained by direct beam, by blocking all the diffracted electron by means of aperture. While the dark field image is obtained by only allowing one diffracted beam to pass through while blocking all the other diffracted and direct beams.

In this study the surfaces (parallel and perpendicular to build direction) of the sample built in first batch (Build-I), were used to obtain diffraction patterns and images by using a Phillips CM 200 TEM operating at 200KeV.

4.3 Energy dispersive X-Ray (EDX):

The interaction of these high energy electrons with inner shell tightly bounded electrons of the specimen cause the ionization of the sample. When an electron from outer shell jumps to inner shell to fill in the vacancy it emits energy in the form of X rays. The x-rays are called characteristics X-rays. These characteristics X-rays generated during interaction of incident high energy electrons electron beam and material under study in SEM or TEM can be used to obtain quantitative and qualitative information regarding composition of the material. Due to the thin foil specimens used in TEM microscopy TEM has much better spatial resolution in compositional analysis than SEM.

 In the current study microanalysis of both α and β phases by TEM/EDX was performed by using a specimen with a foil plane parallel to the build direction from samples of Build-I. Quantitative results of the β phase were obtained from several β particles that were more or less perpendicular to the foil surface. The TEM/ EDX analysis of a large area of about 10 μm^2 in the thin film was also carried out, which can be treated as an average composition of the specimen, and should be close to the composition of the EBM built alloy.

4.4 X-Ray Diffraction (XRD):

XRD is analytical techniques to obtain information about crystalline and atomic structure of the material. The useful information like crystal structure type and lattice parameters can be obtained from XRD spectrum.

In this study XRD measurements were carried out in Philips X'Pert diffractometer with Cu, K_α radiations. Diffraction spectrum was taken with thin film collimator (TFC) detector. The XRD pattern was obtained with scan step of 0.01^o 2 θ, with counting time of$3s$. The sample used in this study were from Build-I.

4.5 Confocal Microscope (CM):

Confocal microscope (CM) has wide ranging applications in the field of biological micrography. The ability of CM to create an image with in-focus planes appearing as bright spots or areas while out of focus planes as dark spots or areas, leads to its application in analyses of surfaces in materials science. The CM has the ability to obtain a series of optical sections, taken at different focal planes. Therefore CM can generate a "through-focus" image with "infinite" depth of field. This ability helps the confocal microscope in finding a role in imaging non-flat or translucent specimens. CM also has the ability to create topographic maps by constructing an image from a series of optical sections taken of a rough surface (D. A. LANGE, 1993). The actual surface area of the specimen can be estimated by geometric construction of the surface represented by the topographic map. Once surface area is computed, roughness of the surface can be characterized.

In current study as build surfaces of samples from Build-II were studied under Eclipse TE2000 inverted confocal LASER scanning microscope (CLSM) (Nikon Corporation, Japan).

4.6 Quantifications of Surface Roughness:

For quantitative analysis of surface roughness, different Matlab routines developed by different scientists were initially tested but imageJ routine SurfCharJ plugin developed by (G. CHINGA, 2007) for supercalendered papers (SC) was found to be more suitable and consistent in results in present work. The plugin is based on several developed routines for surface assessment, and provides global and local roughness analysis, gradient analysis, domain segmentation, surface leveling and directional analysis (G. CHINGA, 2007). The calculations are based on regression plane calculations. The surface representations are horizontally aligned by subtracting a regression plane from the surface. The regression plane is calculated as

$$Z_{ij}= Z_{ij}^{'}\text{-}(\alpha+\beta_1 x_i+\beta_2 y_j) \qquad (1)$$

where $\mathbf{Z}'$ and $\mathbf{Z}$ are the height values of the surface before and after aligning respectively, α, β_1 and β_2 are the least square estimates and x and y are the coordinates axes. The plugin calculates roughness coefficient R_a and R_q by using the Eq. 2 and Eq. 3 respectively (G. CHINGA, 2007).

$$R_a = \frac{1}{N_x N_y} \sum_{i=0}^{N_x} \sum_{j=0}^{N_y} |Z_{ij}| \qquad (2)$$

$$R_q = \sqrt{\frac{1}{N_x N_y} \sum_{i=0}^{N_x} \sum_{j=0}^{N_y} Z_{ij}^2} \qquad (3)$$

Where $N_x N_y$ are the number of area elements along x-axis and y-axis. While calculating the roughness coefficient value in both cases, the value was calculated for each picture in the stack. The average value of R_a or R_q for each stack is calculated and assigned to it. The average of 4x4 adjacent stacks average value was considered to be the representative value for each sample.

4.7 Response Surface Methodology:

Response surface methodology (RSM) is a collection of mathematical and statistical techniques for empirical model building. It is useful for the modelling and analysis of problem in which a response of interest is influenced by several independent variables and optimization of response being the main objective. For the system in which response is linear function of independent variables, a first order regression model is sufficient to model the system. For a system with "n" number of independent variables $(x_1, x_2..., x_n)$ with single response "Y", the first order response model can be written as

$$Y = \beta_o + \beta_1 x_1 + \beta_2 x_2 + \cdots + \beta_n x_n$$

$$Y = \beta_o + \sum_i^n \beta_i x_i + e \qquad (4)$$

where $i = 1,2,\ldots,n$. The above equation is also known as first order or multiple regression model, where coefficients $\beta_o, \beta_1, \beta_n$ are the regression coefficients. Response surface methodology uses statistical models, and therefore it is an approximation to reality with some errors.

As discussed earlier that EBM system is a complex procedure depending upon variety of independent process parameter like scan speed, beam current and even sample thickness. RSM provides an excellent approach to understand the effect of these parameters on the roughness of produced part.

4.8 Phase Field Modelling:

For materials science and engineering simulation of microstructure development is of great importance and use as microstructures plays an important role in mechanical and physical properties of the material. During microstructure development the system undergoes changes in such a way that the total free energy of the system reduces (Chen, 2002). The field of computational materials science has made tremendous progress due to advancements in computational methods and computational capabilities of the systems.

Conventional approaches to simulate phase transformation treat the boundary between two compositional or structural domains as a sharp interface, across which a field variable

varies discontinuously. An alternative technique for investigating systems involving a phase transition is to treat the system as a whole is known as phase field model (A. A. Wheeler, 1992). The principal characteristic of phase-field models is the diffuseness of the interface between two phases; the interface is described by a steep, but continuous, transition of a phase field variable $\varphi(x,t)$ between two states (Steinbach, 2009). In phase field models the total free energy of the system is formulated as a function of the phase fields and the variation of the free energy with respect to the fields act as driving forces for the evolution over time following the Cahn-Hilliard equation for the conserved order parameters φ. The Cahn-Hilliard equation is a partial differential equation written as

$$\frac{\partial \varphi}{\partial t} = \nabla. D\nabla \left(\frac{\partial f}{\partial t} - \epsilon^2 \nabla^2 \varphi \right) \qquad (5)$$

The second term on right hand side of the equation is a gradient energy term, and "f" is a double well free energy function.

$$f = \frac{1}{2} a^2 \varphi^2 (1 - \varphi)^2$$

The double well free energy function penalizes the intermediate states while the energy gradient term penalizes the sharp changes of φ.

Chapter 5

Summary of Results

5.1 Sample Builds:

In total three batches of samples were built in the current work. All the samples were built from gas atomized Ti-6Al-4V powder of $50 - 100 \ \mu m$ size by using Arcam's S12 EBM system.

The first batch of samples (Build-I) was built for microstructural evaluation of EBM built Ti6Al-4V. In this built hexagonal test bars were produced. The length of each test bar was $100 \ mm$ with the cross sectional diameter of $8 \ mm$ by using standard optimized process parameter settings.

The second batch (Build –II) was built to study the effects of sample thickness and different process parameter settings of the EBM system on surface roughness and microstructures of built Ti-6Al-4V. In Build-II four sets of rectangular test slabs each of contours and squares (Fig. 5.1.1) were produced by melting Ti-6Al-4V powder under different process parameter settings. Each set consists of three slabs of approximately $55mm \ X \ 50 \ mm$ in two directions (*x, y*). Each test slab in the set is of different thickness. Process parameter settings were altered between the four sets according to the description in table 5.1.1.

Third batch of samples (Build-III) was built to study the effect of scanning length on microstructures. This build includes $30 \ mm$ tall samples of $10X10 \ mm$ dimension as per $Fig.$ 5.1.2. In one sequence of sample were build with scan length of $10 \ mm$ and in other part they were built with scan length of $50 \ mm$ by using standard processing parameters. Different colours in Fig. 5.2.2 represent different scan speeds as scan speed is increased at the end of build commonly known as turning point. The speed increase is done in areas where the beam is assumed to hit the heat front from the previous hatch line.
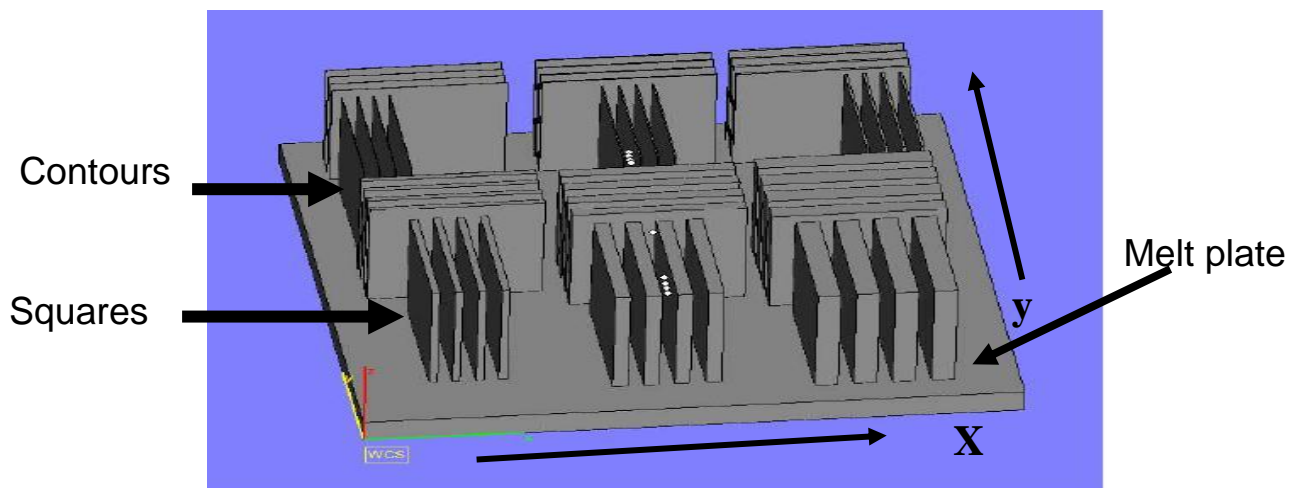
Figure 5.1.1: Schematic representation of **S**ample build up (Build-II)

Table 5.1.1: Parameters settings of different test slabs in Build-II

Test Slab		Scan Speed (mm/s)	Current (mA)	Offset Focus (mA)
Contour 1		250	4	10
Contour 2		250	6	10
Contour 3		250	4	25
Contour 4		250	6	25
Square 1	Contour	180	8	15
	Square	575	9	15
Square 2	Contour	180	8	15
	Square	650	9	15
Square 3	Contour	180	8	30
	Square	575	9	30
Square 4	Contour	180	8	30
	Square	650	9	30

Figure 5.1.2: Schematic representation of samples (Build-III) with different scan length, a) ~ $50mm$ b) $10mm$

5.2 Sample Preparations:

Samples for both optical and electron microscopic studies were prepared by using standard metallographic preparation methods. All surfaces were obtained by mechanical cutting of the test bars under flowing cooling solution.

Samples for optical and SEM studies were first cut into $2\,mm$ thick slices of about $1cm^2$. These samples were then step wise grinded mechanically under flowing water by using silicon carbide papers of grit size from 220 to 800. During the grinding, while changing to finer grit paper, the orientation of the sample was switched by 90° to remove the scratches left by previous paper. These samples were electrochemically polished for $240 - 300\,s$ using Struers double jet unit using electrolyte A3. The electrolyte solution consists of 600ml methanol, $360\,ml$ 2-butoxyethanol and $60\,ml$ perchloric acid. The polishing voltage and current during the electrochemical polishing process were $35V$ and $\sim375mA$ respectively. Some samples for optical microscopic studies were also prepared by mechanical methods

including grinding and polishing. In first step the samples were mounted in plastic resin and then grinded by using silicon carbide papers of grit size from 220 to 800 stepwise in same manner as discussed above, but at the final step they were grinded with $9\ \mu m$ diamond suspension particles to obtain smooth surface. In the final step, the samples were mechanically polished with OP suspension containing $0.04\mu m$ particles of Al_2O_3 with pH of 9.8, for different time durations depending upon surface conditions. The average time of OP polishing was about $240 - 300\ s$.

For TEM studies, the test bars were first sliced into thickness of about $0.2\ mm$ and subsequently grinded to thickness of $0.15\ mm$. These slices were punched to get $3\ mm$ diameter disks. They were electrochemically polished for 50-70 seconds duration by using Struers double jet unit using electrolyte A3. The polishing voltage and current during the electrochemical polishing process were $35V$ and $\sim 125\ mA$ respectively.

In the final step of specimen preparation samples were etched in Kroll's solution (1% HF, 2% HNO_3, balance distilled H_2O) for varying time durations, ranging from $350 - 500\ S$.

For surface roughness studies as build surfaces were used without any grinding or polishing. Samples for surface roughness studies under confocal microscope were stained with propidium iodide (PI).

5.3 Build Defects:

The EBM system due to its nature and mode of operations is susceptible to introduce many defects in the EBM built materials. The sources of these defects can be attributed to the poor beam control resulting in poor melting and undesired porosity. As the energy density of the beam depends upon different process parameter like beam current, offset focus and scan speed the variation in the energy density has the potential to vastly influence the build quality.

In this study a more or less defect free built has been achieved irrespective of parameter settings. The only significant defects were observed when the offset focus was changed from $15\ mA$ to $30\ mA$ in squares samples of S3 and S4 in Build-II. In this case the built with higher offset focus was not fully successful and the samples were quite badly melted, with undesired porosity of about 11 vol % (Fig. 5.3.1 a). Similar build defects have also been reported by (S.M. Gaytan, 2009), for non optimized melting process parameters.

In addition to above mentioned build defect non-uniformly distributed spherical voids (pores) of about 1-6μm in diameter have been observed in all micrographs (Fig. 5.3.1 b). These pores are result of Argon (Ar) gas trapped in the gas atomized Ti-6Al-4V powder (S.M. Gaytan, 2009). Ar is trapped as gas bubble during powder manufacturing. The small size and uneven distribution across the build, has no influence on mechanical properties of EBM built Ti-6Al-4Vparts. These voids can be removed by using single standard HIP process for Ti alloys (S.M. Gaytan, 2009).
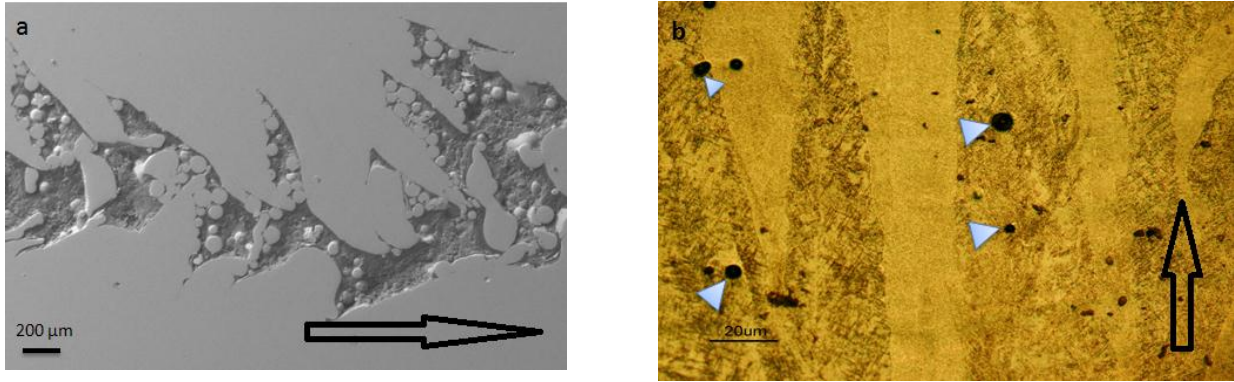
Figure 5.3.1: Example of build defects; a) undesired porosity and un-melted powder particles in sample built with offset focus of 30mA; b) non uniformly porosity due to trapped Ar gas marked with small triangles. (Build direction is marked by block arrow in all micrographs)

5.4 Summary of the Results

5.4.1 Microstructures of EBM built Ti-6Al-4V:

In all the studies un-machined surfaces and un-HIPed samples were studied as the HIPing process.

In general the microstructures of EBM fabricated Ti-6Al-4V consist of very fine microstructure in comparison with the conventional wrought Ti-6Al-4V. The microstructures in EBM Ti-6Al-4V are very similar to the microstructure of Ti-6Al-4V built with other DDM methods (BERND BAUFELD, 2010; Xinhua Wu a, 2004; Lore Thijs, 2012) i.e. containing columnar grains of prior β phase growing along the build direction (Fig 5.4.1.1 a) and Widmanstätten α platelets. Formation of multiple columnar grains of irregular sizes and shapes was observed in planes parallel to build direction. The microstructures inside the columnar grains of prior β phase are typical of any $(\alpha + \beta)$Ti alloy i.e. the Widmanstätten α platelets of different sizes and orientations were observed. In general the size of α-platelets colony is very small and in majority of cases they are present in singular forms. The grain boundary α layer (α_{GB}) was also found to form along the grain boundaries of the prior β grain as marked in Fig. 5.4.1.1(b). The width and thickness of these α platelets ranges from 5–$10\ \mu m$ and $2 - 3\ \mu m$ respectively. Fig. 5.4.1.2 (a) presents the SEM micrographs of surface parallel to the build direction revealing the α and β phases by compositional contrast in a back scattered electrons (BSE) image. Considering the morphology of the β phase in surfaces parallel and perpendicular to the build direction, it can be assumed that the β phase possesses a rod-like shape in EBM produced Ti-6Al-4V.
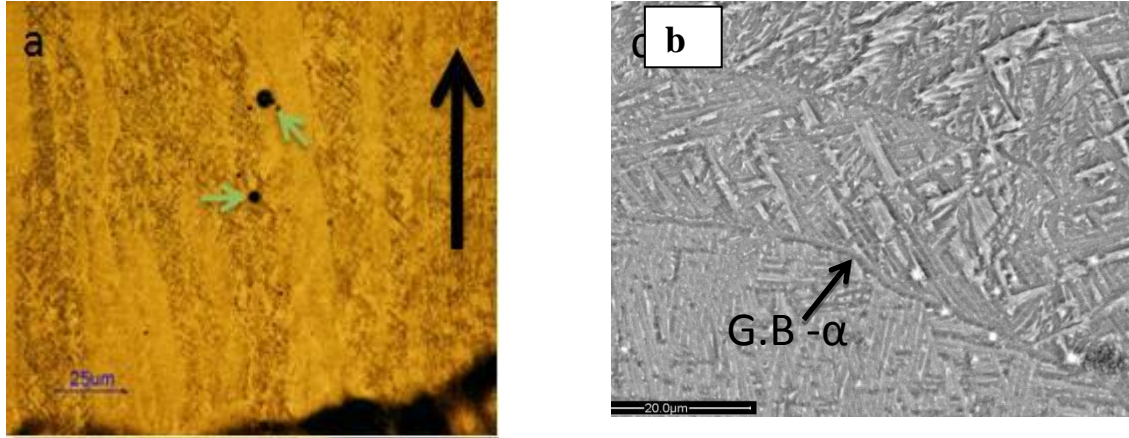
Figure 5.4.1.1: a) Optical micrograph showing a typical columnar microstructure of Ti-6Al-4V produced by EBM method in type I surface where the build direction is marked with arrow, small arrows indicate Ar gas pores; b) SEM/SEI of a typical columnar grain.

The β phase in EBM built Ti-6Al-4V was resolved with TEM. It was observed that, the β phase possesses a rod-like shape in EBM produced Ti-6Al-4V with diameter of about 200nm. A dark field TEM image in Fig. 5.4.1.2 (b) taken by a common diffraction beam of two groups of β particles with different orientations, reveals β rods with orientation parallel to the foil plane (β_L) and more or less perpendicular to the foil plane β_T. In the majority of cases the growing direction of β phase rods is parallel to build direction. Quantitative results of TEM / EDX analysis from the α and β phases are listed in table 5.4.1.1. A large amount of V (β stabilizers), have been detected in β rods, while in the β phase composition of Al, an α stabilizer, is well below the average composition for the alloy. A small amount of iron (Fe) was also detected in the β phase. It has been reported that (Arcam, 2008; S.M. Gaytan, 2009) a small amount of Fe (about $0.07\ wt\%$) is present in the Ti-6Al-4V powder. It is expected that Fe will diffuse in to the β phase during its formation since it is also a β stabilizer. While in α grains the composition of V is below the average composition of the alloy. These results indicate that the $(\alpha + \beta)$ structures are formed by diffusion controlled transformation in which V diffuses to β phase while Al diffuses to α phase. The volume fraction (Vol %) for the rod shaped β phase in the EBM produced Ti-6Al-4V alloy has been calculated to be about 2.7% according to the TEM/EDX results. TEM /EDX result indicates the absence of any martensitic phase.
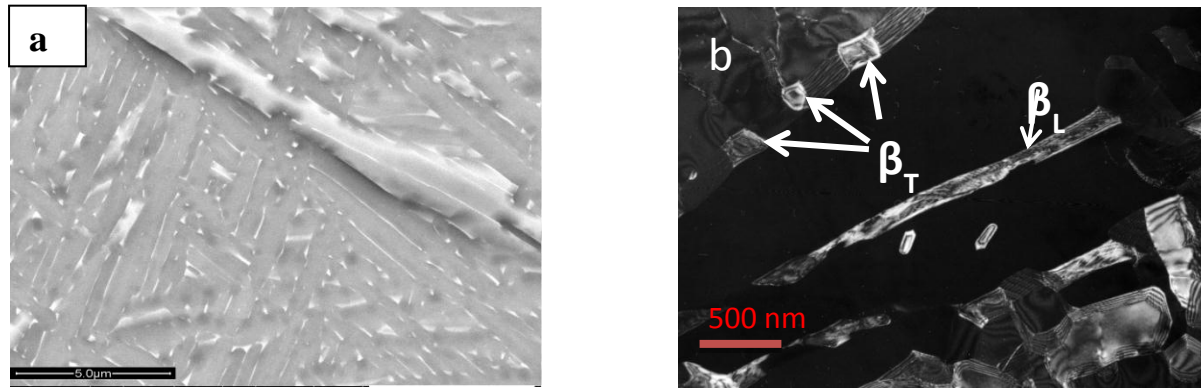
Figure5.4.1.2: **a)** SEM/BSE images showing typical microstructure in surfaces perpendicular to build direction; b) Dark field TEM image of a surface parallel to the build direction.

Table 5.4.1.1: TEM/EDX analysis of phases in the EBM built Ti-6Al-4V

Element / Phase	Ti		Al		V		Fe	
	wt%	at %	wt%	at %	wt%	at %	wt%	at %
α-phase	90.5 ± 0.2	86.6	6.1±0.2	10.4	3.4 ± 0.3	3.0	-	-
β-phase	66.9 ±1.5	67.27	1.9±0.1	3.39	29.5±1.5	27.9	1.67±0.06	1.44
Large Area	90.6	87.24	5.3	9.05	4.1	3.71	-	-

- **:** undetectable

5.4.2   Effect of sample thickness and processing parameters on microstructures:

EBM process is a complex procedure depending upon different processing parameters of the system like beam power, beam size, scan speed, scanning direction and scanning strategy. The final microstructures of EBM built Ti-6Al-4V and many other materials are the result of complex combination of different processing parameters of the system.

To study the influence of different processing parameters, such samples are chosen from Build-II (table 5.1.1, Fig 5.1.1) that have a similar build up environment, except the parameter of interest. Planes parallel to build direction were of major interest and accordingly the thin plane

(of varying thickness) is marked as Surface one (S-I) and 55mm wide plane is marked as surface-II (S-II).

As discussed in section 5.4.1, in general the microstructures of EBM fabricated Ti-6Al-4V, consist of columnar grains of prior β phase growing along the build direction across multiple build layers and widmanstätten α platelets (A. Safdar, 2012; S.S. AL-BERMANI, 2010). These two phenomena were observed in all samples irrespective of process parameter settings or thickness. The size, shape regularity and number of prior β columnar grains are different in samples built under different parameter settings and thickness of test slab. The difference observed in microstructural observations can be attributed to the different factors affecting the microstructural development i.e. the geometrical effects, the power density of the beam and the scanning strategy.

To study the geometrical effect, microstructures of samples build with different thicknesses, and from different positions across the built were studied. In general it was observed that with increasing thickness of the test slab the diameter of prior β columnar grain increases and microstructures become coarser. With the increasing thickness the prior β columnar grains get a more regular shape and have regular orientation along the build direction and the number of prior β columnar grains increases, see Fig. 5.4.2.1. In some cases especially in bottom part of sample many grains are so close that they looks like bunches growing parallel to the built direction (Fig. 5.4.2.3). Similar trends were observed when two surfaces of the same built were compared, with the wider surface (S-II) have the characteristics of thicker sample in comparison to narrower surface (Fig. 5.4.2.1 b and Fig. 5.4.2.3 a). In thicker samples (Fig. 5.4.2.2 (a, b)) the grain boundary α layer (α_{GB}) is quite smooth and regular and α platelets are fairly regularly arranged, although the α platelets are longer and coarser in thicker samples. It was observed that the diameter of prior β columnar grain decreases with the increase in height, and the bunch of columnar grains is quite big in the bottom part (Fig. 5.4.2.3).

In general it has been observed that with increase in energy density the number of columnar grains increases (Fig. 5.4.2.3 a, and 5.4.2.4 a) and the grain boundary get smoother Fig (5.4.2.2 b and 5.4.2.4 b). The bunch size of the columnar grain is higher for built with higher energy density. It has also been observed that with decrease in energy density the columnar grains are somewhat tilted (about 20°) in direction of scanning, while in case of higher energy density they follow the build direction (Fig. 5.4.2.3 a, and 5.4.2.4 a). The grain boundaries α layer is smoother in sample with high energy density, Fig 5.5.2 b, and in case of low energy density the grain boundary α layer is wavy, Fig.5.5.4 b.
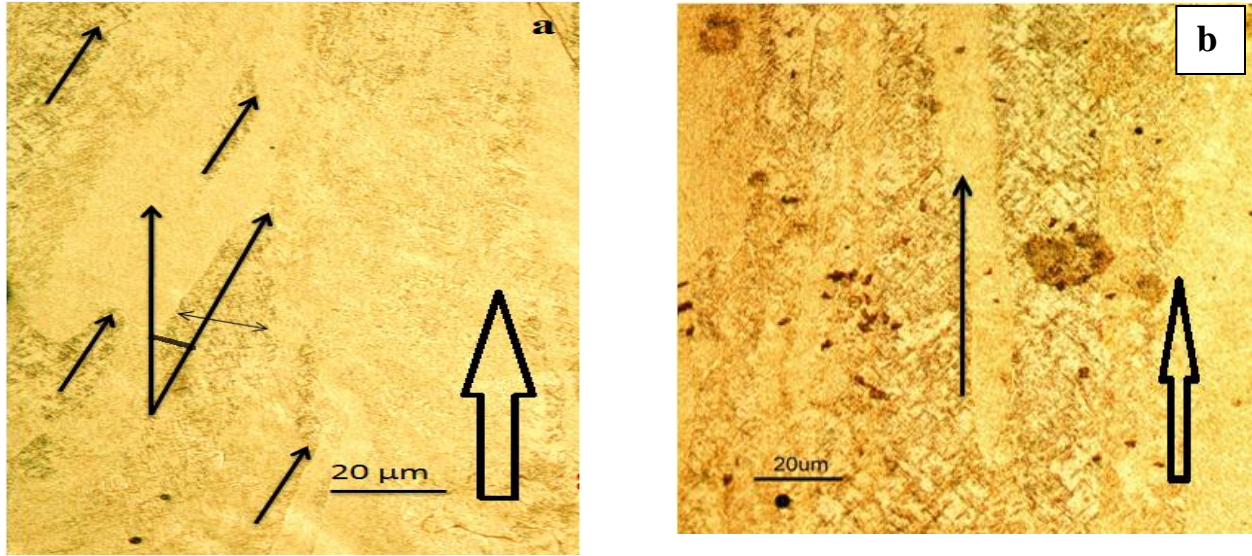
Figure 5 .4.2 .1: Optical Micrograph illustrating the general microstructures of S-I samples build with scan speed of 575 mm/s, current of 9 mA and offset focus of 15 mA and with thickness of a) 3.5 mm, small arrows indicate inclination of grains. b) 7.5 mm
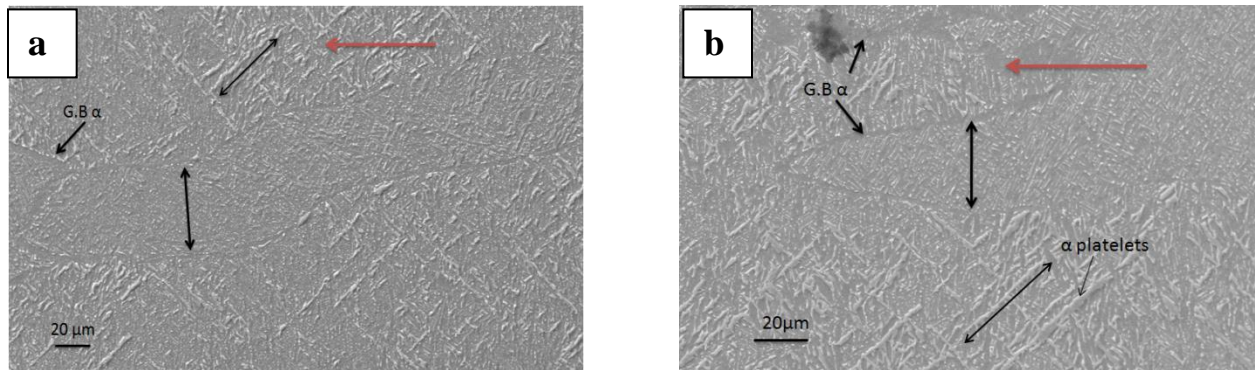
Figure 5.4.2.2: SEM secondary electron image micrograph illustrating the general microstructure in the top part of S-I of samples build with scan speed of 575mm/s, beam current of 9 mA and offset focus of 15 mA and with thickness a) 5.5 mm, b) 7.5 mm. (⟷: width of columnar grain and length of α platelets).
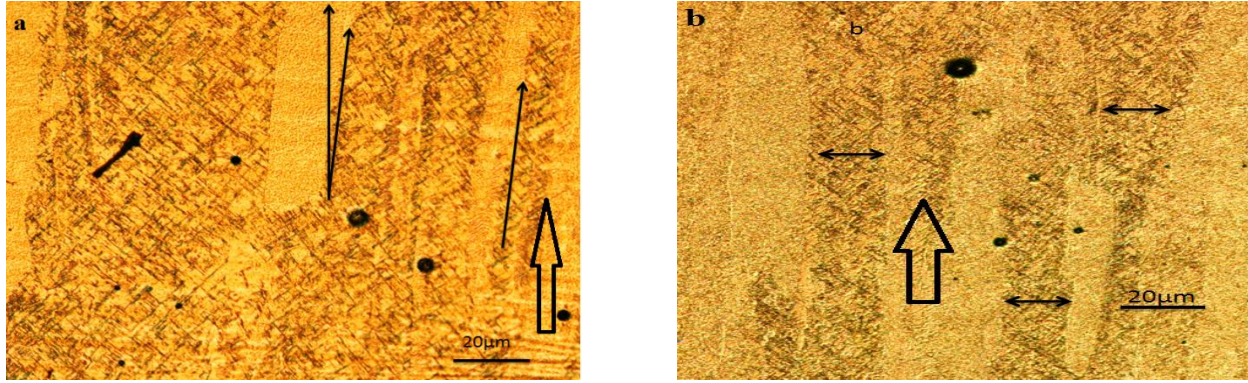
Figure 5.5.3: Optical micrographs illustrating the microstructures of the top and bottom part of S-II in the 7.5 mm thick samples build with beam current of 9 mA, scan speed 575 mm/s and offset focus of 15 mA; a) Bottom part, b) Top part.
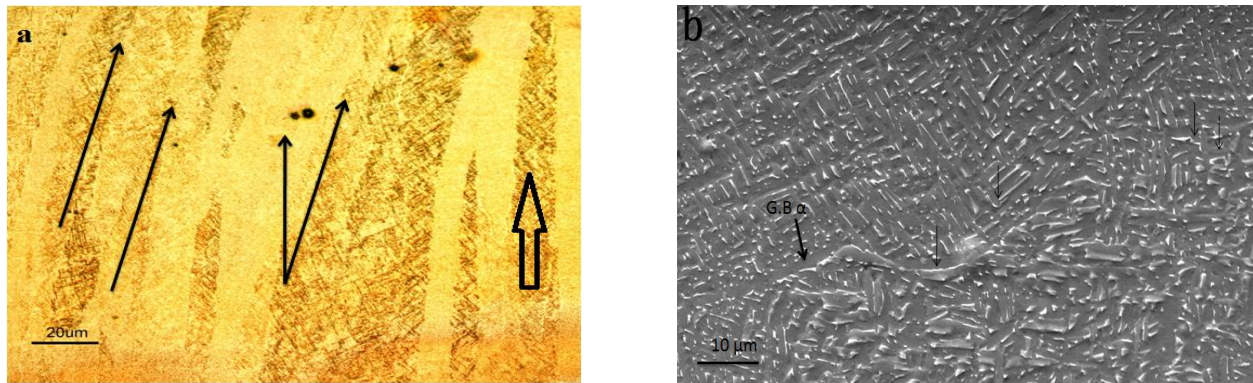
Figure 5.4.2.4: Micrograph illustrating the general microstructures in sample built with low energy density   a) Optical,   b) SEM.

The scanning length has quite an effect on the size and geometry of prior β columnar grains. For the samples with short scanning length the grains are long but are not very thick (Fig. 5.4.2.5 a, b). While for the samples with long scanning length the geometry of the grains is quite irregular. The diameter of columnar grains varies irregularly along the build direction, in some cases the variation is as large as 10 µm. The respective grains boundaries in both cases are quite smooth and regular (Fig. 5.4.2.6 a, b). The effect of the scanning length on α_{GB} width is almost negligible. For the case of low scanning length in some cases relatively bigger α platelets colony size is observed, and α platelets are longer and thicker for shorter scanning length.
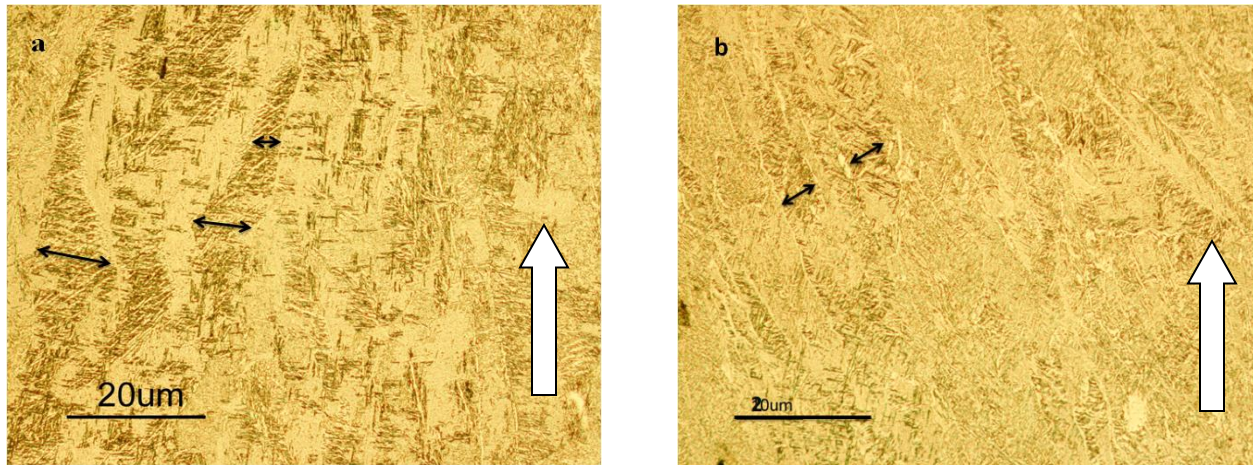
Figure 5.4.2.5: Optical micrograph illustrating the general microstructures of S-II the samples build with scan length of a) 50 mm b) 10 mm
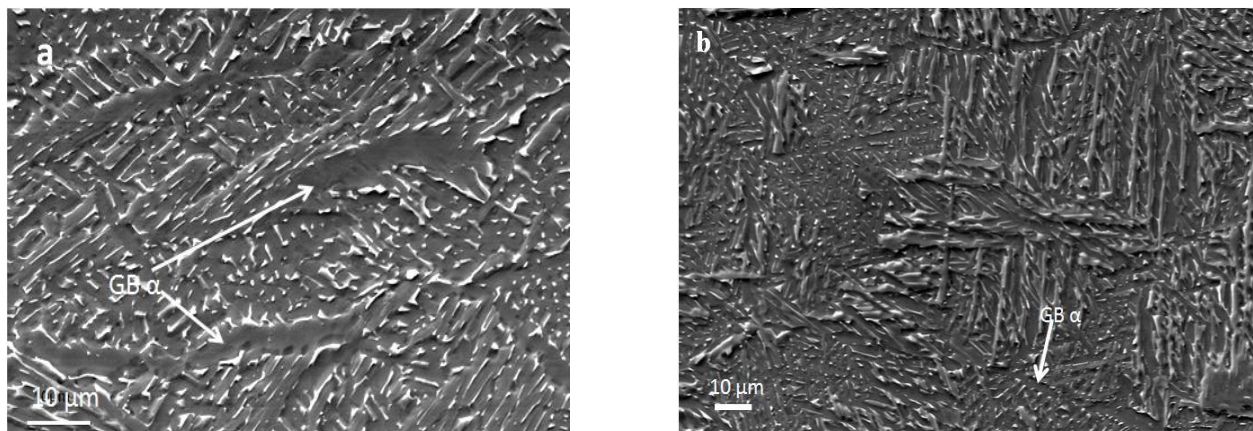
Figure **5.4.2.6***:* SEM micrograph illustrating the general microstructures of S-II the samples build with scan length a) 50mm b) 10 mm.

5.4.3 Effect of sample thickness and processing parameters on surface roughness:

A key issue in materials used in dentistry and orthopedic implants is how material influences and, is influenced by the biological surroundings which results from the contact between the material and biological system (S. Ponader, 2007; Jukka, 1996). The surface properties, surface chemistry, surface energy, topography and roughness of the implant material influence the initial cell response at the cell material interface, ultimately affecting the rate and quality of new tissue formation (D. Deligianni, 2001). Surface roughness is also related to wear and friction properties of the material and hence is related to the life time of the implant. Therefore it is an important property of any material to be considered as biomaterial.

In this study every sample produced by EBM systems has visible and detectable surface roughness. Similar results have been reported by (P. Thomsen, 2008; S. Ponader, 2007) for EBM built Ti-6Al-4V parts, and by (G.P. DINDA, 2008) for DLD fabricated Ti-6Al-4V scaffolds. Fig. 5.4.3.1 a, is a SEM micrograph of the as built surface-II, showing partially melted powder or sintered powder attached to the surface. Some valleys parallel to melt plate have also been observed in surface-II, (Fig. 5.4.3.1 (a)). The width and depth of theses valleys are different at different points. The inter valleys spacing is much larger than the width of each deposited layer of powder during buildup process. A mountain-valley structure is observed in cross-sections of the samples which were cut parallel to build direction Fig. 5.4.3.1 (b), could be one of reason of the surface roughness.

The surface roughness is quantified as described in section 4.6. Fig. 5.4.3.2 represents the R_a results graphically where the average value of R_a at different adjoining areas of the samples is plotted against the area numbers. For every sample sixteen ($4x4$) adjoining areas were selected as representative area for comparative studies. As in all the graphs presented in the Fig. 54.3.2 shows that for every area the value of R_a is always either larger or smaller than the R_a value of corresponding area in second sample, this enables us to make a safe conclusion about which sample has comparatively higher or lower R_a or R_q value.

It was observed that the process parameter settings and sample thickness have a strong effect on the surface roughness of the EBM produced parts. The value of surface roughness variable R_a varies between $1 - 20\ \mu m$ for different samples, depending upon the process parameter setting and thickness. The surface roughness increases with increasing sample thickness and beam energy density which is the function of beam current, offset focus and scan speed. The beam energy density increase with increase in beam current and decreases with increase in scan speed and offset focus.

The first order linear regression equation representing the surface roughness as function of sample thickness (A), beam current (B), scan speed (C) and offset focus (D), on the basis of above method can be written as

$$R_a = 4.85 + 7.8\,A + 4.2\,B - 10.5C - 0.5D$$
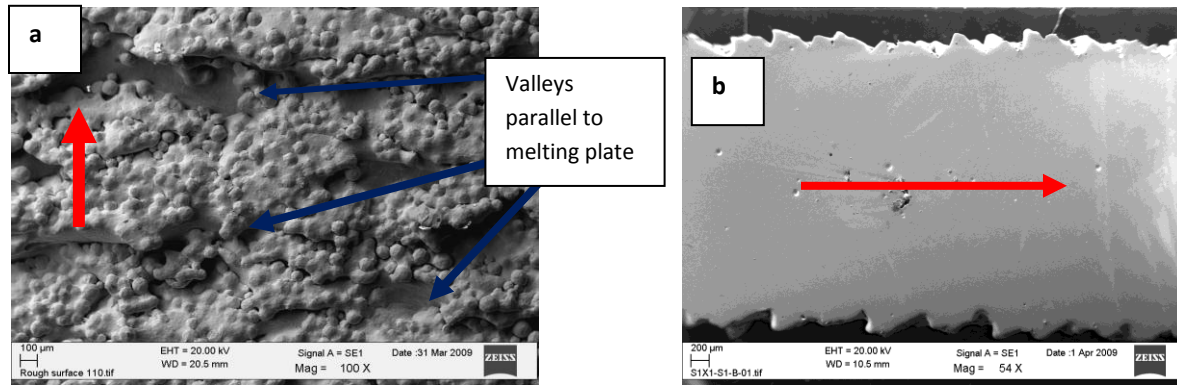
Figure 5.4.3.1: SEM micrograph of surface morphology of the as built slab a) as built S-II b) Cross section of the S-I illustrating inharmonic mountain-valley structure for sample with thickness of 3.5 mm.
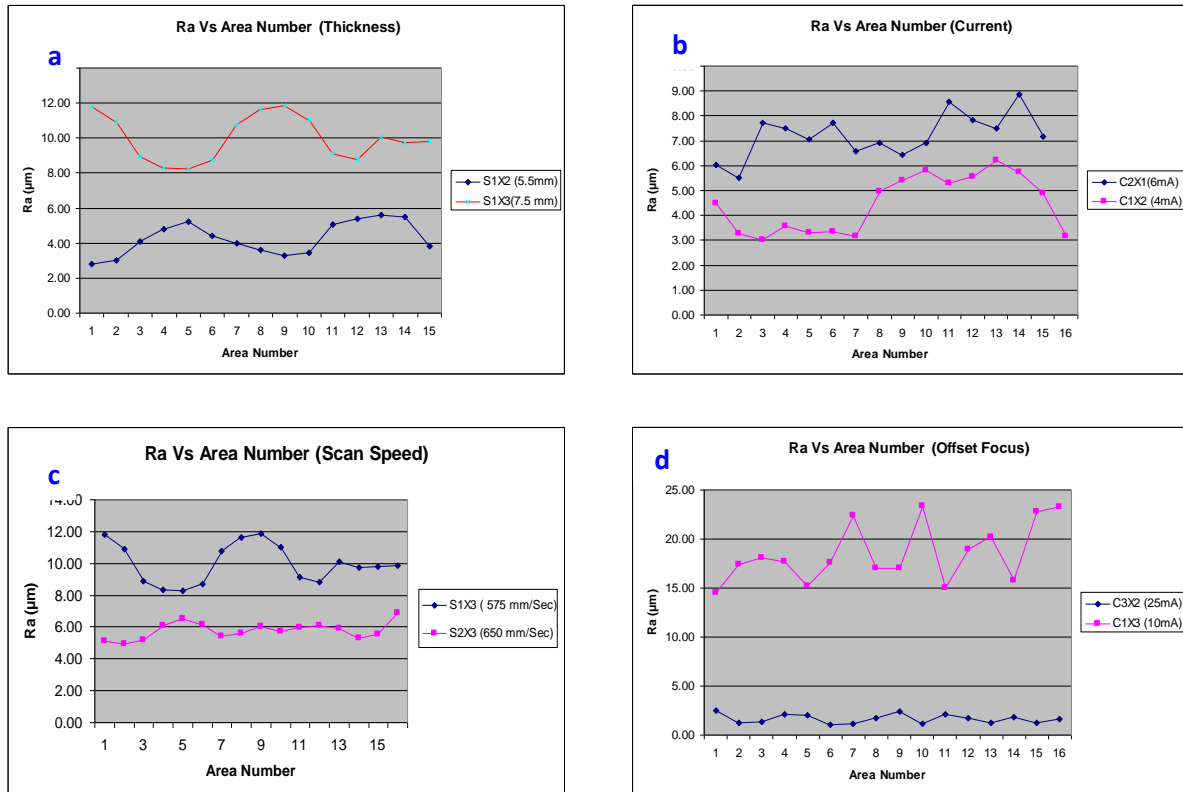
Figure 5.4.3.2: Plot of R_a Vs area number for comparative study of two samples a) thickness of 5.42 mm and 7.42 mm; b) current of $4mA$ and $6mA$; c) scan speed of 575 mm/S and 650 mm/S; d) offset focus of 10 mA and 25 mA.

5.4.4 Phase field modelling of microstructural development:

Heat distribution in the built part plays an important role in microstructural development of EBM built Ti-6Al-4V. During the addition of each layer in the structure the already built part undergoes multiple re-melting and phase transformations depending upon its distance from the top layer before a stable build temperature is achieved. In order to reconstruct the heat treatment history of the layer, the heat flux and temperature distribution in the body is assumed to be governed by Fourier's first and second laws and a relation similar to Rosenthal equation is obtained:

$$T(x, y, x) = \frac{P}{2\pi\lambda r} \, exp\left(\frac{-v(y - r)}{2\kappa}\right)$$

Where P is the power of the beam; v is the scan speed or velocity of the moving source; $\lambda =$ thermal conductivity; $r = \sqrt{x^2 + (vt)^2}$; κ is the material parameter and $\kappa = \lambda/(\rho. \, c_p)$; where ρ is the density and c_p is the specific heat capacity of the material.

The temperature distribution in layers underneath the newly deposited layer is presented in Fig 5.4.4.1.
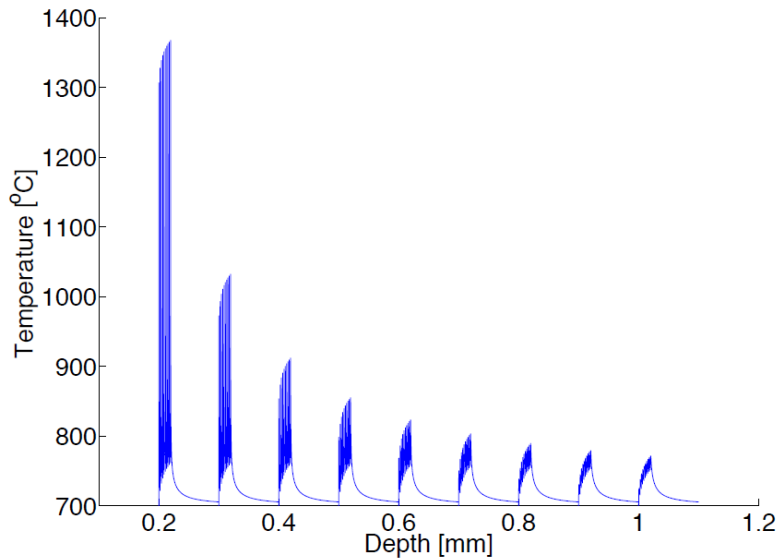
Figure 5.4.4.1: Temperature history from 0.2mm to 1 mm beneath the melted layer.

The simulation of microstructure development in deposited material was carried out using a phase field model. The results are presented in Fig.5.4.4.1. The phase field variable φ varies with compositional difference of vanadium (V) in the phase where $\varphi(x) = \begin{cases} 0, & \beta - phase \\ 1, & \alpha - phase \end{cases}$; The BCC β phase is enriched in V which is β stabilizer (Benoıt Appolaire *, 2005),.

31

In the EBM process the microstructure development takes place in three steps (A. Safdar, 2012). During the first rapid cooling from melting temperature to the isothermal hold at 700 ^{O}C the prior β phase is transformed in to HCP α' phase as cooling rate is well above the required martensite formation rate of 410 ^{O}C/s. the HCP α' is also enriched in β stabilizer (Lutjering, 2003). The Fig.5.4.4.2 a, represent the martensitic structures. In EBM built Ti-6Al-4V during the isothermal hold at 700 ^{O}C, the martensitic phase decomposes and this decomposition is completed in about 30 minutes (F.X. Gil Mur, 1996). The simulated results in Fig. 5.4.4.2 b and c simulate the decomposition phenomenon.
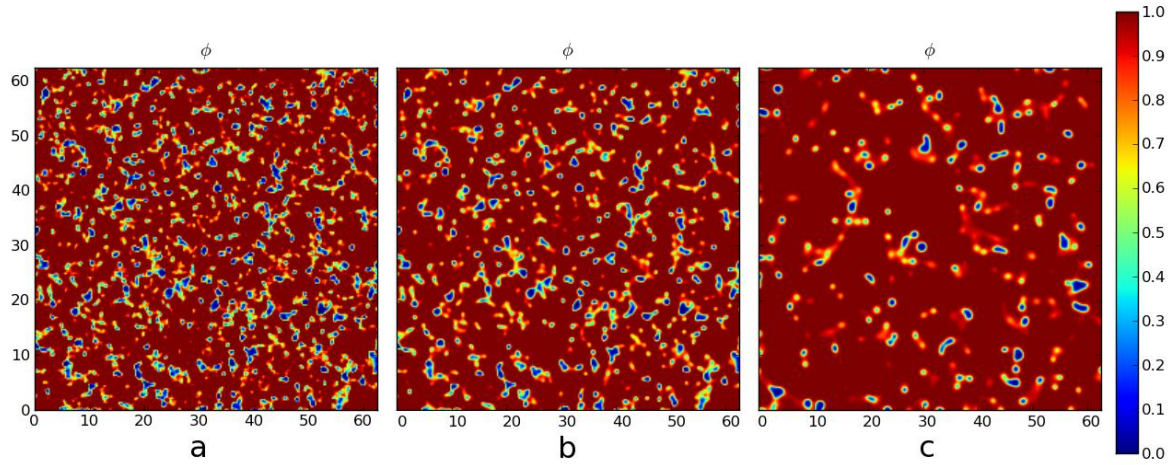
Figure 5.4.4.2: The evaluation of the phase φ at the depth of 1mm; a) at 700 ^{O}C without holding time; b) after annealing for 200 s at 700 ^{O}C; c) after annealing for 1800 s at 700 ^{O}C.

Bibliography:

1. **A. A. Wheeler W. S. Boettinger, and G. B. McFadden** Phase-field model for isothermal phase transitions in binary alloys, PHYSICAL REVIEW A . - 1992. - 10 : Vol. 45. - pp. 7424-7439.

2. **A. Safdar L.-Y. Wei, A. Snis, Z. Lai** Evaluation of microstructural development in electron beam melted Ti-6Al-4V , Materials Characterization. - 2012. - Vol. 65. - pp. 8-15.

3. **A. Suáreza M. J. Tobar, A. Yáñeza, I. Pérez, J. Sampedro, V. Amigó, J. J. Candel** Modeling of phase transformations of Ti6Al4V during laser metal deposition, Physics Procedia . - 2011. - Vol. 12. - pp. 666–673.

4. **Arcam** Home page [Online]. - 2008. - 03 03 2012. - www.arcam.com.

5. **Benoıt Appolaire Ludovic He´richer, Elisabeth Aeby-Gautier** Modelling of phase transformation kinetics in Ti alloys –Isothermal treatments, Acta Materialia 53. - 2005. - pp. 3001–3011.

6. **BERND BAUFELD OMER VAN DER BIEST, and STEVEN DILLIEN** Texture and Crystal Orientation in Ti-6Al-4V Builds Fabricated by Shaped Metal Deposition, Metallurgical and Materials transactions A, volume 41A, . - 2010. - pp. 1917-1927.

7. **Chen Long-qing** Phase field models for microstructure evaluation, Annu. Rev. Mater. Res . - 2002. - Vol. 32. - pp. 113-140.

8. **Cormier Denis, Harrysson Ola and West Harvey** Characterization of H13 steel produced via electron beam melting, Rapid Prototyping Journal 10: 1. - 2004. - pp. 35-41.

9. **D. A. LANGE H. M. JENNINGS, S. P. SHAH** Analysis of surface roughness using confocal microscopy, Journal of Materials Science 28 . - 1993 . - pp. 3879-3884.

10. **D.D. Deligianni N., Katsala, S. Ladas and D. Sotiropoulou, J., Amedee, Y.F., Missirlis** Effect of surface roughness of the titanium alloy Ti-6Al-4V on human bone marrow cell response and on protein adsorption, Biomaterials, Volume 22, Number 11. - 2001. - pp. 1241-1251.

11. **Deckard C.** Methods and Apparatus for Producing Parts by Selective Laser Sintering ,Patent No : 4863538. - USA, october 17, 1986.

12. **F.X. Gil Mur D. Rodrguez, J.A. Planell** Influence of tempering temperature and time on the α' Ti-6Al-4V, Journal of Alloys and Compounds 234. - 1996. - pp. 287-289.

13. **G.P. DINDA L. SONG, and J. MAZUMDER** Fabrication of Ti-6Al-4V Scaffolds by Direct Metal Deposition, Metallurgical and Materials Transactions A. - 2008. - pp. 2914-2922.

14. **GARY CHINGA PER OLAV JOHNSEN, ROBERT DOUGHERTY, ELISABETH LUNDEN BERLI,JOACHIM WALTER** Quantification of the 3D microstructure of SC surfaces, Journal of Microscopy, Vol. 227, Pt 3. - 2007 . - pp. pp. 254–265.

15. **L. Zeng T.R. Bieler** Effects of working, heat treatment, and aging onmicrostructural evolution and crystallographic texture of α, α' α'' and β phases in Ti–6Al–4V wire, Materials Science and Engineering A. - 2005. - Vol. 392. - pp. 403–414.

16. **L.E. Murr S.A. Quinones, S.M. Gaytan, M.I. Lopez, A. Rodela, E.Y. Martinez et al.** microstructure and mechanical behavior of Ti–6Al–4V produced by rapid-layer manufacturing, for biomedical applications, Journal of the Mechanical Behavior of Biomedical Materials 2. - 2009. - pp. 2 0 - 3 2.

17. **Lausmaa Jukka** Surface spectroscopic characterization of titanium implant materials, Journal of Electron Spectroscopy and Related Phenomena 81. - 1996 . - pp. 343-361.

18. **Lore Thijs Frederik Verhaeghe , Tom Craeghs, Jan Van Humbeeck , Jean-Pierre Kruth** A study of the microstructural evolution during selective laser melting of Ti-6Al-4V , Acta Materialia . - 2012. - Vol. 58. - pp. 3303–3312.

19. **Lutjering G.** Book :Titanium. - Berlin : Springer, 2003.

20. **Lutjering G.** Influence of processing on microstructure and mechanical properties of (α+β) titanium alloys , Materials Science and Engineering A 243. - 1998. - pp. 32–45.

21. **M. Peters J. Hemptenmacher, J. Kumpfter and C. leyens** Titanium and Titanium Alloys. - [s.l.] : Wiley-Vch GmbH & Co. KGaA, 2003.

22. **Niinomi Mitsuo** Mechanical properties of biomedical titanium alloys , Materials Science and Engineering A. - 1998. - Vol. 243. - pp. 231–236.

23. **Operational Manual Arcam** Operational Manual. - Götenburg : [s.n.], 2008.

24. **Peter Thomsen Johan Malmström Lena Emanuelsson, Magnus Rene´ Anders Snis** Electron Beam-Melted, Free-Form-Fabricated Titanium Alloy Implants: Material Surface Characterization and Early Bone Response in Rabbits, Journal of Biomedical Materials Research Part B: Applied Biomaterials. - 2008. - pp. 35-44.

25. **S.M. Gaytan L.E. Murr, F. Medina, E. Matrinez, M.I. Lopez, R.B. Wicker** Advanced metal powder based manufacturing of complex components by electron beam melting , Materials Technology. - 2009. - 3 : Vol. 24. - pp. 180-190.

26. **S.S. AL-BERMANI M.L. BLACKMORE, W. ZHANG, and I. TODD** The Origin of Microstructural Diversity, Texture, and Mechanical Properties in Electron Beam Melted Ti-6Al-4V , Metallurgical and Materials Transactions A. - 2010. - Vol. 41 A. - pp. 3422-3434.

27. **Sabine Ponader Eleftherios Vairaktaris, Peter Heinl, Cornelius v. Wilmowsky, Andreas Rottmair, et al.** Effects of topographical surface modifications of electron beam melted Ti-6Al-4V titanium on human fetal osteoblasts, Journal of Biomedical Materials Research Part A. - 2007. - pp. 1111-1119.

28. **Steinbach Ingo** Phase-field models in materials science , Modelling Simul. Mater. Sci. Eng. - 2009. - Vol. 17. - pp. 1-31.

29. **T. Ahmed H. J. Rack** Phase transformations during cooling in α+β titanium alloys, Materials Science and Engineering A 243. - 1998. - pp. 206–211.

30. **Xinhua Wu a Jing Liang , Junfa Mei , C. Mitchell, P.S. Goodwin , W. Voice** Microstructures of laser-deposited Ti–6Al–4V , Materials and Design . - 2004. - Vol. 25. - pp. 137–144.

ELSEVIER

MATERIALS CHARACTERIZATION

Evaluation of microstructural development in electron beam melted Ti-6Al-4V

A. Safdar[a, d,]*, L.-Y. Wei[a], A. Snis[b], Z. Lai[c]

[a]Division of Materials Science, Malmö University, SE-205 06 Malmö, Sweden
[b]Arcam AB, SE 43137, Mölndal, Sweden
[c]Institute of Microtechnology and Nanoscience, Chalmers University of Technology, Sweden
[d]PINSTECH, P.O Nilore, Islamabad, Pakistan

ARTICLE DATA

ABSTRACT

In the current work an investigation of the microstructures of EBM built Ti-6Al-4V test bars has been performed using OM, SEM, TEM and XRD. It has been found that the prior β phase, that formed during the initial solidification, possesses a column shaped morphology with growing direction parallel to built direction. Typical ($\alpha + \beta$) structures namely Widmanstätten α platelets with rod-like β phase formed on the interfaces of the fine α grains, have been observed in the columnar prior β grains. Grain boundary α phase was found to be formed around the boundaries of the columnar prior β grains. Different phases present in the parts, especially the BCC β phases have been characterized. The TEM/EDX results indicate very high V composition in the β phase. Results of TEM/SAED and XRD also revealed that a superlattice structure could be present in the β phase. Phase transformation sequence is discussed according to the processing history and the microstructures observed.

1. Introduction

Due to their excellent combination of mechanical and physical properties Titanium and its alloys especially Ti-6Al-4V, are widely used engineering materials in aerospace, automotive, energy and medical implant industries. Metallic materials, in general, are used as implant materials where the hard tissues are to be replaced like dental root or hip joint etc. [1]. In such applications high fatigue life, strength and comparable Young's modulus are important parameters to be considered [2]. Among the metallic biomaterials used for hard tissue replacement, such as stainless steel and Co–Cr alloys, Ti and its alloys exhibit the most suitable characteristics for biomedical applications because of their light weight, specific strength, high biocompatibility, corrosion resistance and human allergic response [1,2]. Their good biocompatibility is due to excellent corrosion resistance and low toxicity owing

to instant formation of oxide layer [3]. Ti-6Al-4V is a two-phase (α/β) alloy. Microstructure plays an important role in determination of mechanical properties like strength, creep resistance fracture toughness etc. of alloys [4]. Microstructure of Ti-6Al-4V like any other alloy normally depends on chemical composition, processing history and heat treatment [4,5]. The control of texture and microstructure is necessary to control the physical and mechanical properties of Ti-6Al-4V [6].

Direct digital manufacturing (DDM) is the next embodiment of solid free form fabrication (SFF), additive manufacturing (AM) or rapid prototyping (RP). Different DDM techniques include direct light fabrication (DLF), LASER engineering net shape (LENS), direct LASER deposition (DLD) and electron beam melting (EBM). In all these methods metallic objects are produced directly from computer aided design (CAD) files by melting the metallic powder/wire by a high energy focused beam. EBM is one of such methods. EBM system has been

* Corresponding author. Tel.: +46 40 665 7704; fax: +46 40 665 7706.
E-mail address: adnan.safdar@mah.se (A. Safdar).

described in details by [1,7–9]. EBM systems involve building of three-dimensional fully dense or near net-shape metallic structures/objects layer-by-layer in high vacuum environment. This process involves shaping a powder bed and selectively melting the powder to form a three-dimensional solid object, using high energy focused electron beam and multi-axis motion. Each layer is formed by overlapping several melt beds, which are made by continuously overlaying a new bed of powder over the existing layer. One of the advantages of EBM or any DDM process is the possibility to build complex geometries like downward facing surfaces in cooling channels as single unit avoiding machining and welding etc. EBM process is very energy efficient and applicable to highly reflective materials like Aluminum [7].

It is difficult to predict the microstructures of DDM produced metallic objects due to very complex thermal history [10]. Different scientists have studied the microstructures of Ti-6Al-4V produced by different DDM methods including EBM [1,8,10–14]. In this study we have tried to understand the microstructure at different stages of buildup process in EBM produced Ti-6Al-V and to characterize the different phases by using Optical Microscope (OM), Scanning Electron Microscope (SEM), Transmission Electron Microscope (TEM) and X-ray diffractometer.

2. Materials and methods

2.1. Materials

In this study the hexagonal test bars were produced from gas atomized Ti-6Al-4V powder of 25–40 μm size. The length of each test bar was 100 mm with the cross-sectional diameter of 8 mm. The buildup time was approximately 10 h and the chamber temperature (build temperature) was approximately 700 °C. The initial cooling rate from melting temperature to 700 °C was very rapid, while from 700 °C to room temperature when the last layer is deposited was very slow and the cooling time in last step was approximately 8 h.

2.2. Specimen preparation

Three types of surfaces related to the build direction were obtained by mechanical cutting of the bars under flowing cooling solution (Table 1). Samples for microscopic studies were prepared by using standard metallographic preparation methods. For OM studies, the specimens of about 10 mm thickness were grinded and polished mechanically for varying time durations to obtain smooth surface. For SEM and TEM studies, the test bars were first sliced into thickness of about 0.2 mm and subsequently grinded to thickness of 0.15 mm. These slices were punched to get 3 mm diameter disks. These samples were electrochemically polished for 50–70 s duration by using Struers double jet unit using electrolyte A3. The electrolyte solution consists of 600 ml methanol, 360 ml 2-butoxyethanol and 60 ml perchloric acid. The polishing voltage and current during the electrochemical polishing process were 35 V and 125 mA respectively. In the final step of specimen preparation all the samples were etched in Kroll's solution (1% HF, 2% HNO_3, balance distilled H_2O) for varying

Table 1 – Types of surfaces prepared for the microstructural investigations.

Surface type	Surface under study[1]	Description
I		Perpendicular to layer deposition (multiple layers at cross-section)
II		Perpendicular to the layer deposition and Surface type-I (multiple layers along the axis of bar)
III		Parallel to the layer deposition (single layer)

1: with respect to build direction.

time durations, ranging from 350 to 500 s. Samples prepared for optical micrographic studies were also used for XRD analysis.

In this study the microstructures and different phases present in the hexagonal test bars of Ti-6Al-4V, were studied using Nikon Elipse L150 Optical Microscope (OM), FEI QUANTA 200 Environmental Scanning Electron Microscope (SEM) at 20 kV, PHILLIPS CM200 Transmission Electron Microscope (TEM) and Philips X'Pert diffractrometer.

3. Results

3.1. XRD

XRD measurements were carried out in Philips X'Pert diffractometer with Cu, Kα radiations. Diffraction spectrum was taken with thin film collimator (TFC) detector. The XRD pattern was obtained with scan step of 0.01° 2θ, with counting time of 3 s.

Fig. 1 presents the XRD pattern of the sample. Since the known results of the alloy Ti-6Al-4V are not much reported in literature and JCPDS cards are also not available for the alloy, we have to match our pattern for indexing with already published pattern of the alloy in [6,10,15]. The indexing is presented in Table 2. The Bragg's peaks detected in the XRD scan
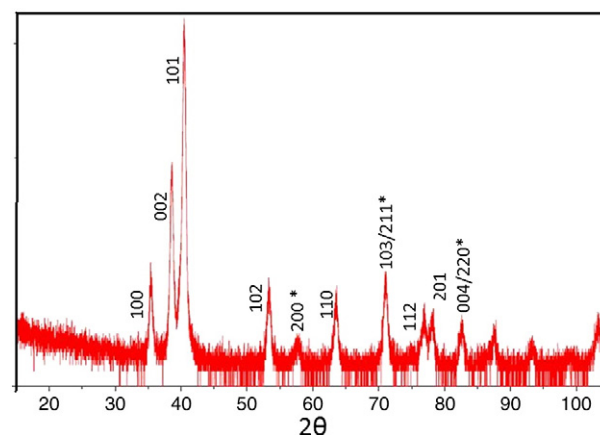
Fig. 1 – XRD pattern for the EBM build Ti-6Al-4V sample.

Table 2 – X-ray diffraction data for the Ti- 6Al-4V.

2θ°	d (nm)	I (counts)	I (relative)	hkl-α	hkl-β
35.33	0.2536	66	11	100	
38.6	0.2332	218	37	002	
39.65	0.2273	43	7		110
40.47	0.2228	585	100	101	
53.29	0.1718	51	9	102	
57.89	0.1592	11	2		200
63.72	0.1459	44	8	110	
71	0.1295	57	10	103	
	0.1326				211
76.9	0.1239	30	5	112	
78.29	0.1220	27	5	201	
82.67	0.1166	22	4	004	
	0.1139				220

belonging to either HCP α-Ti or BCC β-Ti phase are listed in Table 2. No peaks for other phases like orthorhombic martensite (α″) have been observed. From the scan results β phase in the alloy has been characterized by $(200)_\beta$ reflection with inter-planer spacing 'd' of 0.1592 nm. In comparison with the XRD spectra of Ti-6Al-4V alloy produced by conventional methods [6,15] and for direct metal deposition method [10], where both 110 and 200 peaks of β phase were observed distinctly, but in this study there is no distinct peak for 110 plane in the spectrum (Fig. 1) corresponding to the β phase. The XRD results when analyzed with Match! Phase analysis software using Crystallography Open Database (COD), indicated that there is a weak possible peak at 2θ = 39.65° corresponding to the (110) reflection of β phase. The amplitude of Bragg's peak for any {hkl} plane is proportional to the structure factor (F_{hkl}) which is determined by the atomic scattering factor and positional coordinates of the atom in a unit cell of crystalline material. The rearrangement of atoms in crystal lattice such as ordering could cause reduced amplitude of the Bragg peak. The very weak reflection for 110 of the β phase could be caused by an ordered structure or other crystal defects in the EBM produced Ti-6Al-4V alloy. The lattice parameters of the BCC β phase in the EBM built Ti-6Al-4V has been determined to be a = 0.3184 nm. For the α phase in the alloy 'a' and 'c' are 0.2925 nm and 0.4665 nm respectively, with c/a ratio of 1.5948.
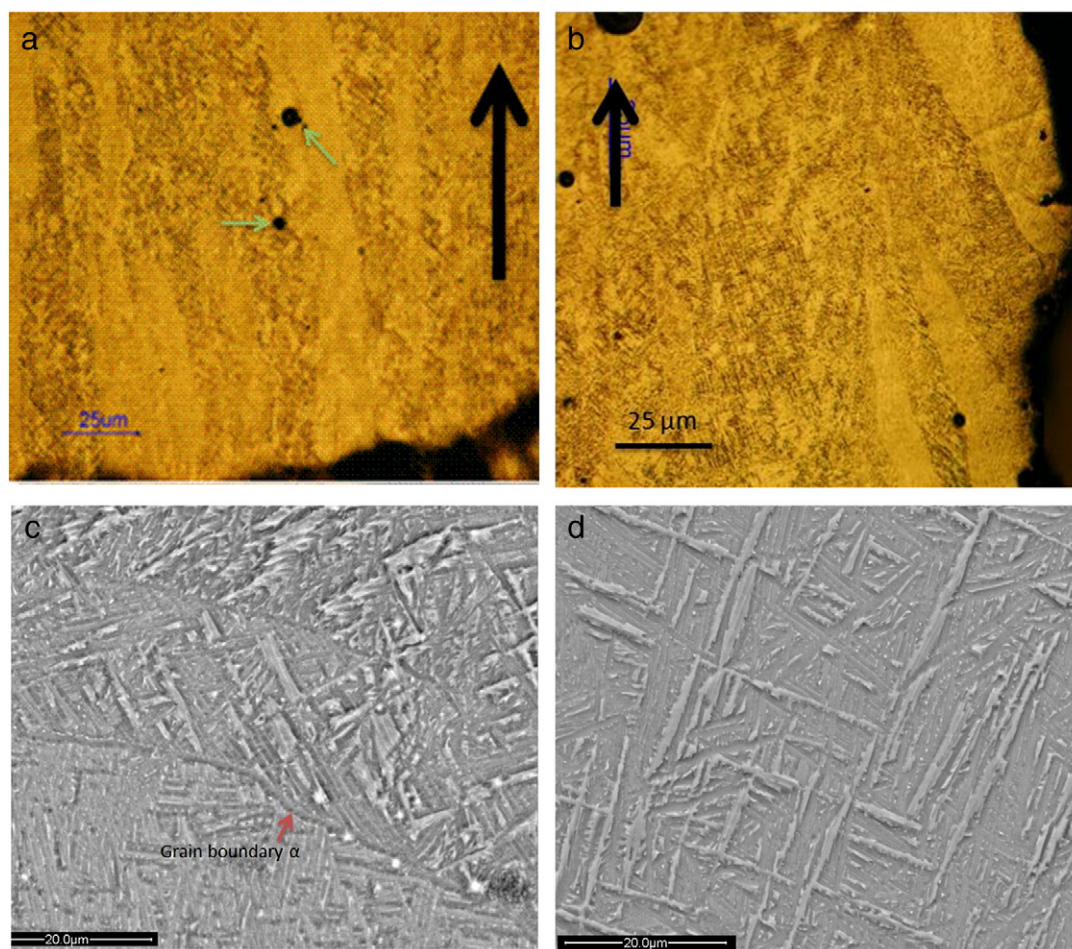
3.2. Microstructure

In general the microstructures of EBM fabricated Ti-6Al-4V consist of very fine microstructure in comparison with the conventional wrought Ti-6Al-4V. The microstructures in EBM Ti-6Al-4V are very similar to the microstructure of Ti-6Al-4V built with other DDM methods [10–12,14] i.e. containing columnar grains of prior β phase growing along the build direction and Widmanstätten α platelets. Fig. 2(a) presents the optical micrograph of type-I surface illustrating the typical microstructure of Ti alloys produced by EBM process. Formation of multiple columnar grains of irregular sizes and shapes was observed in type-I and -II surfaces. In comparison to LASER based or wire based DDM methods no distinctive layers of deposited materials have been observed in the current study. The grains formed inside of the test bar with growing direction tracking the build direction, while in the

case of columnar grains near the surface the growth direction often deviates from the build direction and seems to track the temperature gradient inside the built (Fig. 2(b)). The diameter of these grains ranges from 20 to 200 μm. The diameter of grains decreases with the increase in height of the sample. In all optical/SEM micrographs non-uniformly distributed spherical voids (pores) of 1–6 μm in diameter, as arrowed in Fig. 2(a) have been observed which are due to the presence of Argon (Ar) in gas atomized Ti-6Al-4V powder. These voids in general can be eliminated by standard HIPing process for Ti alloys. The microstructures inside the columnar grains of prior β phase are typical of any (α + β) Ti alloy i.e. the Widmanstätten α platelets of different sizes and orientations as shown in Fig. 2(c). In general the size of α-platelets colony is very small and in majority of cases they are present in singular forms Fig. 2(d). The grain boundary α layer was also found to form along the grain boundaries of the prior β grain as marked in Fig. 2(c).

Fig. 3(a) presents the SEM micrographs of surface parallel to the build direction revealing the α and β phases by compositional contrast in a back scattered electron image (BSI). In a BSI the high contrast is the result of electron scattering from phases of relatively higher contents of heavy elements in the alloy. In the case of Ti-6Al-4V, β stabilizing element Vanadium (V) is the relatively heavy element in comparison to Ti and Al. As previously reported by B. Appolair et al. [16], it was found that β phase in the Ti alloys is enriched in β stabilizer species. Hence the bright spots and lines in the micrographs are the fingerprint of β phase in the EBM built Ti-6Al-4V. As shown in Fig. 3(a) the line shaped β phases were often observed along the α platelets and at the interface of two platelets. The β phases of dot-like morphology were also observed in Fig. 3(a). Fig. 3(b) is a SEM/BSI of type-III surface which is perpendicular to the build direction. Fig. 3(b) is mostly revealing a dot-like morphology for the β phase embedded in the α platelets. The diameter of these bright spots is much less than 1 μm. Considering the morphology of the β phase in type-I and -III surfaces, it can be assumed that the β phase possesses a rod-like shape in EBM produced Ti-6Al-4V. Fig. 3 (b) also reveals the cross-section of the α platelets. The width and thickness of these α platelets range from 5 to 10 μm and 2 to 3 μm respectively. Thicker Widmanstätten α platelets contain several layers of α platelets with β phase formed on the interface of the adjacent layers with more or less regular spacing of approximately 0.5 μm.

Due to the limitations of the SEM spatial resolution, further analysis of the microstructure especially for the fine rod-shaped β phase in the EBM built Ti-6Al-4V requires Transmission Electron Microscopy (TEM) studies. In order to obtain reliable TEM/EDX results and a stronger TEM/SAED pattern for analysis of β phase, specimens were selected from surface type-III, because most of the β rods are more or less vertical to the thin foil plane.

Fig. 4(a) is a bright field TEM image of specimen of surface type-I illustrating the α grains and the rod-like β phase formed on boundaries of α grains. Fig. 4(b) is a selected area electron diffraction (SAED) pattern taken from an α grain in the central region in Fig. 4(a). Solution of the SAED pattern such as shown in Fig. 4(b) indicates that the grain is a α grain with zone axis $[2201]_\alpha$. The bright field image in Fig. 4

Fig. 2 – a) Optical micrograph showing a typical columnar microstructure of Ti-6Al-4V produced by EBM method in type-I surface where the build direction is marked with arrow; b) columnar grain near the surface of the build; c) SEM/SEI of a typical columnar grain; d) α-platelets and α-colonies in surface I. SEM/SEI.

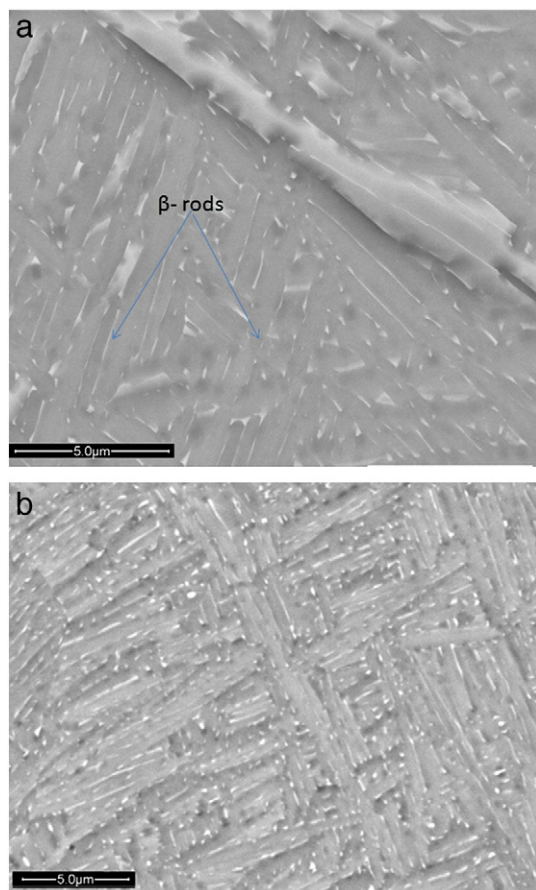(a) also reveals relatively low density of dislocations in the α grain.

TEM investigations for the β phase were performed by using sample of surface type-III. TEM micrographs of rod-shaped β particles and their corresponding SAED patterns are shown in Fig. 5(a–d). The SAED pattern in Fig. 5(c) is relatively complex due to very fine phases in the EBM built Ti-6Al-4V. The SAED pattern and its schematic solution in Fig. 5(d) clearly reveal two SAED patterns from the BCC β phase, one of the pattern can be indexed with $[547]_\beta$ zone axis and another one with $[115]_\beta$ zone axis. The two diffraction patterns have a common row of diffraction spots as shown in Fig. 5(d). A dark field image in Fig. 5(b) taken by a common diffraction beam $(321)_\beta$, reveals two groups of β particle with different orientations, parallel to the foil plane (β_L) and more or less perpendicular to the foil plane (β_T). The bright contrast at the right bottom corner in Fig. 5(b) is due to some extra reflections from other grains that were also enclosed by the objective aperture. The cross-section of the β_T shows an equiaxial morphology.

It has been observed that the reflections from (110), (330) and (550)… planes along [110] direction in the pattern with zone axis $[115]_\beta$ are absent. This phenomenon is consistent with the XRD results shown in Fig. 1, in which the 110 diffraction of the β phase was very weak. The extinction of 110 diffraction is possibly due to the formation of some kind of super lattice or ordered structure in the EBM produced Ti-6Al-4V alloy. Ordering of the β phase probably occurred during the hold at 700 °C. In the ordered β phase V and Ti atoms and perhaps also the Al atoms could occupy their dedicated sites in the lattice instead of a randomly arranged disordered structure. Further work is yet to be performed to solve the atomic position in the supper lattice or the ordered β phase.

Microanalysis of both α and β phases by TEM/EDX was performed by using specimen with foil plane parallel to type-III surface. Quantitative results of the β phase were obtained from several β_T particles. The TEM/EDX analysis of large area of about $10 \mu m^2$ in the thin film was also carried out, which can be treated as an average composition of the specimen, and should be close to the composition of the EBM built alloy. TEM/EDX spectra from the α and β phases are illustrated in Fig. 6(a–b) and the quantitative results are listed in Table 3. A large amount of V (β stabilizers), has been detected in β rods, while in the β phase composition of Al, an α stabilizer in the alloy, is well below the average composition for the alloy. A small amount of iron (Fe) was also detected in the β

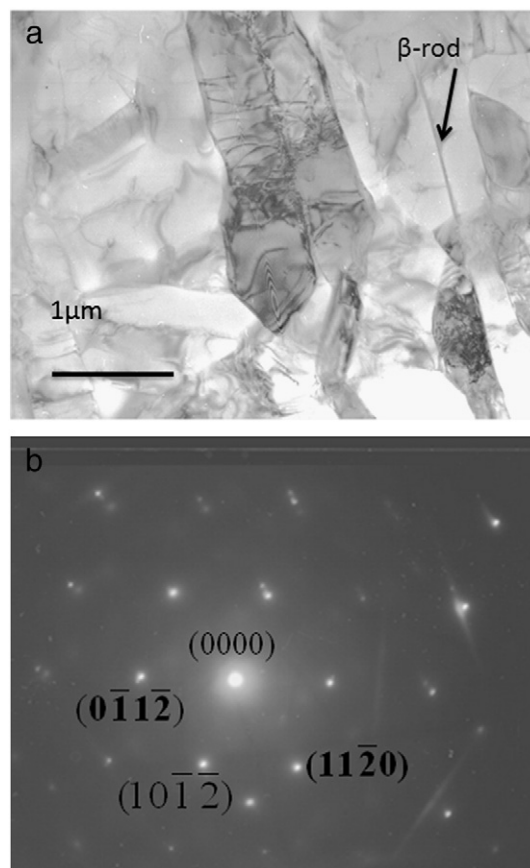Fig. 3 – SEM/BSE images showing typical microstructure in surfaces a) type-I; b) type-III.

Fig. 4 – TEM micrograph of type-I samples. a) Bright field image showing α grains; b) SAED pattren with zone axix $[2\bar{2}01]_\alpha$, taken from an α grain in the central region of (a).

phase. It has been reported that [1,8] a small amount of Fe (about 0.07 wt.%) is present in the Ti-6Al-4V powder. It is expected that Fe will diffuse in to the β phase during its formation since it is also a β stabilizer. While in α grains the composition of V is below the average composition of the alloy. These results indicate that the α+β structures are formed by diffusion controlled transformation in which V diffuses to β phase while Al diffuses to α phase. The Fe is undetectable in the α phase and in the large area of thin foil due to the very low contents. The volume fraction (vol.%) for the rod-shaped β phase in the EBM produced Ti-6Al-4V alloy has been calculated to be about 2.7% according to the TEM/EDX results.

4.   Discussion

The microstructures of Ti-6Al-4V alloys are heat treatment and processing history dependent [4,5]. It is difficult to predict the microstructures of DDM produced metallic objects due to very complex thermal history [10]. For EBM built Ti-6Al-4V, the phase transformation from the liquefied temperature of about 1900 °C to room temperature when the built has been finished is a three-step procedure i.e. 1) rapid cooling from ~1900 °C to ~700 °C; with cooling rate in order of 10^3–10^5 K/s as estimated by S.S.Al-Bermani [13] 2) holding at the build

temperature of ~700 °C; and 3) slow cooling from build temperature to room temperature once the built is finished.

The β transus temperature for Ti-6Al-4V alloy is about 995 ± 20 °C [4,17]. In Ti-6Al-4V, a wide variety of phases in addition to HCP α and BCC β phases, can be generated at different stages of heat treatment and processing such as HCP martensite (α′) and orthorhombic martensite (α″) etc. [6]. The phase transformation from liquefied β phase to room temperature microstructures can take place via two processes.

1) Diffusion controlled transformation:
When the temperature drops below the β transus temperature, high temperature prior β phase (β_p) is transformed in to (α + β) microstructure. The transformation mainly occurred during the isothermal hold at about 700 °C, similar to the isothermal transformation of the wrought Ti-6Al-4V alloys. At first, the grain boundary α phase (α_{GB}) nucleates heterogeneously on the prior β columnar grains [16,17], and grows in directions normal to the grain boundaries to form an α layer. The α_{GB} does not possess a certain orientation relationship with the prior β phase. After the formation of α_{GB}, the Widmanstätten plates start nucleating along the α_{GB} allotriomorphs inside the prior β columnar grains. The nucleation rate according to the classical theory of nucleation depends on the initial temperature and cooling rate. With increased cooling rate the size of α
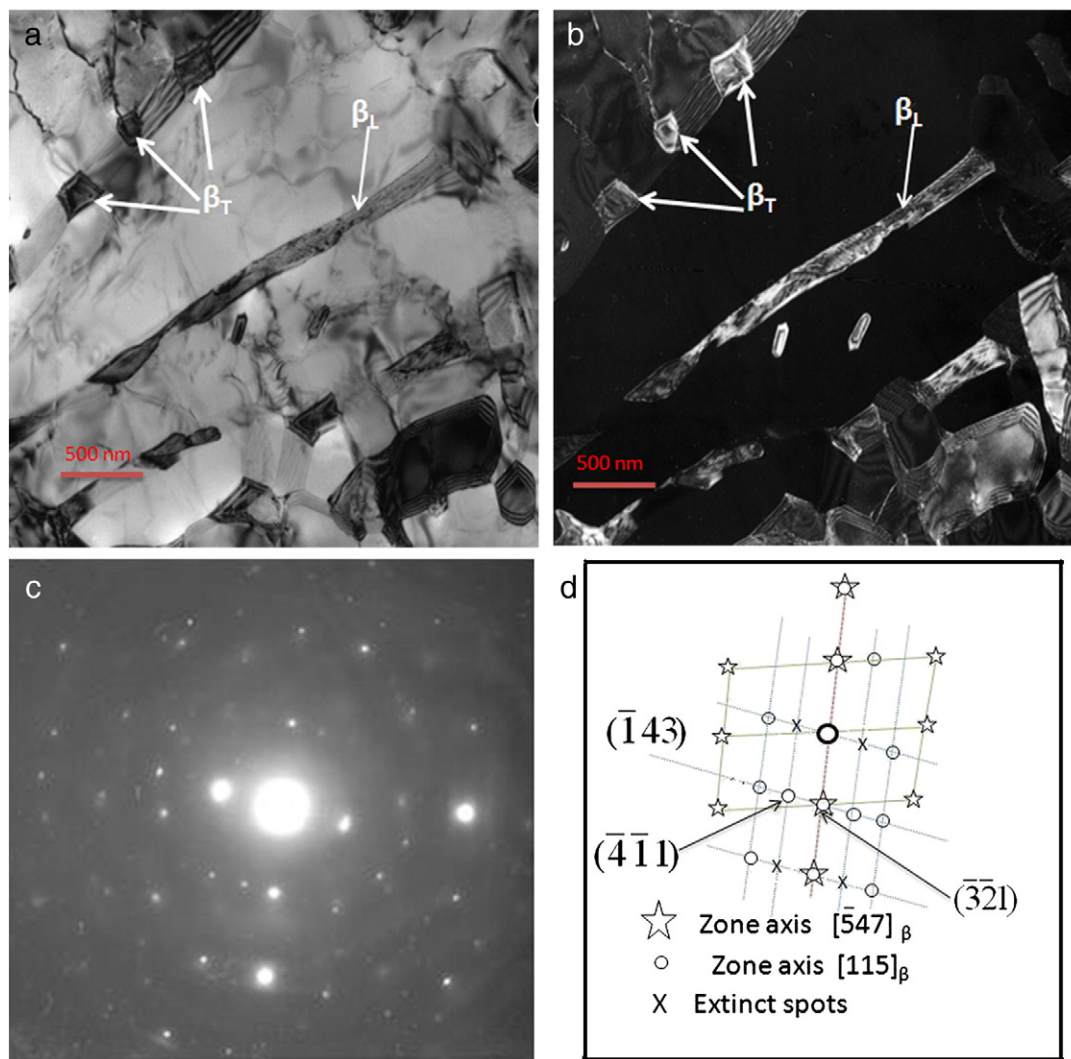
Fig. 5 – Rod-shaped β phase formed on the boundaries of α grains in the EBM produced Ti-6Al-4V alloy. TEM. Type-III surface. a) Bright field image; b) dark field image taken by using a reflection beam $[\bar{3}\bar{2}1]_{\beta}$; c) SAED pattern; d) schematic solution of SEAD pattern in (c).

colony and thickness of α platelet decrease [17]. The α platelets with different orientations satisfying Burger's relationship related to the prior β matrix, grow up and form α platelets colonies of identical crystallographic orientations. In the case of EBM built parts, very fine Widmanstätten α platelets and small colony size rather singular platelets have been observed. Simultaneously, the rod-shaped β phase is formed on the interfaces of α platelets. It is a process in which element partitioning via diffusion is involved wherein α stabilizing elements diffuse to α phase and β stabilizing elements diffuse to β phase. The TEM/EDX in the present study has also shown that the α phase is enriched in α stabilizer Al, and the rod-shaped β phase is enriched in β stabilizer species such as V and Fe. In this process no martensitic transformation at any stage is involved.

2) Transformation involving martensite formation:

According to T. Ahmed et al. [18], if Ti-6Al-4V alloy is rapidly cooled down with cooling rate of more than 410 °C/s from single β phase to (α+β) region, fully martensitic phase (α′) will form. For the EBM produced Ti-6Al-4V alloy studied in this work, the initial cooling rate from ~1900 °C to 700 °C is much higher than 410 °C/s, therefore it is suspected that during this cooling fully martensitic (α′) microstructures would form. Gaytan et al. and Murr et al. [8,19] for EBM built and Thijs et al. [21] for selective laser melted Ti-6Al-4V have reported the formation of martensitic phase. S.S. Al-Bermani [13] also reported martensitic phase in 1–5 mm tall EBM built samples. According to L. Zeng et al. [6] during the hold at ~700 °C two transformations are possible. The first possible transformation is when martensitic phase decomposes to form an (α+β) phase i.e. α′→α+β. The second possible transformation involves formation of α″ phase i.e. α′→α″+β. The transformation of α′ phase to α″ phase is thermodynamically unfavorable due to large lattice strain between two phases owing to the big lattice difference. On the other hand the lattice difference between α and α′ phases is relatively small. As no peaks belonging to the α″ phase have been observed in the XRD,

Fig. 6 – TEM/EDS spectra of phases in EBM built Ti-6Al-4V using thin film of surface type-III a) α-phase b) β phase.

Therefore any martensite formed during the initial cooling, will transform to α+β microstructures during the hold at 700 °C. The transformation of α′ into α+β phases is similar to tempering of the any martensite at elevated temperature. According to F.X. Gil Mur et al. [20] the transformation from a martensite α′ to α+β phase at 700 °C in Ti-6Al-4V alloy is completed in about 30 min which is much shorter than holding time during the build. Therefore it can be concluded that the phase transformation of α′ to α+β is completed during this hold. During the initial cooling a small amount of retained β phase might possibly exist alongside the martensitic α′ phase, and this retained prior β phase, if any, is also transformed to α+β phase during the hold at 700 °C.

Hence the transformation sequence in EBM built Ti-6Al-4V for aforementioned two possible processes can be summarized as:

For diffusion controlled process:

a) During solidification prior β phase (β_p) is formed i.e.; $L \rightarrow \beta_p$.

b) During rapid cooling from high temperature (above β transuses temperature) to 700 °C, β_p transformed to α_{GB} and Widmanstätten plates containing α grains and rod-shaped β phase located on the α grain boundaries.

For transformation involving martensite formation:

a) During solidification prior β phase (β_p) is formed i.e.; $L \rightarrow \beta_p$.

b) If the cooling rate is fast enough from high temperature (above β transuses temperature) to 700 °C, β_p transformed to martensite (α′) phase i.e. $\beta_p \rightarrow \alpha'$.

c) During the hold at 700 °C α′ phase transformed to a+β microstructures i.e. $\alpha' \rightarrow \alpha + \beta$.

Owing to the formation of the α_{GB} layer about the grain boundaries of the prior β columnar grain in EBM built Ti-6Al-4V studied in the current work, it seems the most likely phase transformation process is diffusion controlled. If a fully martensitic phase is formed during the initial cooling in prior β columnar grains, it may not be possible to form the α_{GB} layer around the grain boundaries of the columns. The

Phase	Element							
	Ti		Al		V		Fe	
	wt.%	at.%	wt.%	at.%	wt.%	at.%	wt.%	at.%
α phase	90.5±0.2	86.6	6.1±0.2	10.4	3.4±0.3	3.0	-	-
β phase	66.9±1.5	67.27	1.9±0.1	3.39	29.5±1.5	27.9	1.67±0.06	1.44
Large area	90.6	87.24	5.3	9.05	4.1	3.71	-	-

Table 3 – TEM/EDS analysis of phases in the EBM built Ti-6Al-4V.

-: undetectable.

existence of martensitic phase in 1–5 mm tall EBM built samples as reported by S.S. Al-Bermani [13] can be attributed to the fact that in small samples the built time is very small and doesn't provide enough time to fully decompose the α′ phase.

The nucleation and growth of columnar grains of prior β phase takes place during the initial rapid cooling i.e. this process happens in a very short time and above the β transus temperature. In this study it was observed that the typical height of the prior β columnar grain is much bigger than the thickness of each layer of deposited powder. This shows that melting and solidification of each layer are not single step phenomena. During the build up the melted pool is solidified by ejecting heat in two ways: either by ejecting the heat to the surrounding or to the already built part [12]. During the initial rapid cooling although the previously melted layer is solidified but still it is kept at relatively high temperature and when the second layer is melted over it, due to the very thin layer, the solidified layer also gets some part of the energy and is partially re-melted. Secondly, during the solidification of the second layer it also ejects some heat to the previous layer. This partial re-melting is repeated many times but with each addition of layer the re-melting of previous layers decreases. This heat transfer to layers beneath the melted layer acts as a source of the continuous growing of columnar grain along the build direction. The regularity of geometry of the grain depends upon the cooling rate and cooling path. In the middle part of the build majority of the heat is transferred to the underlying layer therefore more regular geometry columnar grains have been observed. In the case of grains near the surface a good part of energy from molten pool is ejected to the surroundings due to the immediate contact and hence the growth direction of the columnar grain is effected and less regular geometry and deviation of columnar grains of prior β phase from the path fallowing the built direction is observed.

5.   Conclusion

1. In general the uniformity of microstructures across the build has been observed.
2. Spherical voids (pores) of 1–6 μm diameter have been observed in all samples due to the presence of Ar gas in gas atomized alloy powder.
3. In general, microstructures of Ti-6Al-4V consist of columnar grains of prior β phase growing along the build direction. Columnar grains of prior β phase near the surface tend to deviate from the built direction. Inside the prior β grains the α+β structure consists of Widmanstätten α platelets with rod-shaped β phase formed on the boundaries of the α grains.
4. The BCC β phase in EBM built Ti-6Al-4V has been characterized by using XRD and TEM/SAED. The lattice parameter has been measured to be a=0.3184 nm. The average chemical composition of β phase was measured by using TEM/

EDX to be 66.9 wt.% of Ti, 1.9 wt.% of Al, 29.5 wt.% of V and 1.67 wt.% of Fe.
5. An ordered structure or a superlattice structure possibly exists in BCC β phase.
6. The lattice parameters of the HCP α phase has been measured to be a=0.2925 nm and c=0.4665 nm with c/a ratio of 1.5948. The average chemical composition of α phase measured by TEM/EDX to be 90.5 wt.% of Ti, 6.1 wt.% of Al, and 3.4 wt.% of V.

REFERENCES

[1] Murr LE, Esquivel EV, Quinones SA, Gaytan SM, Lopez MI, Martinez EY, et al. Mater Charact 2009;60:96–105.
[2] Niinomi M. J Mech Behav Biomed Mater 2008;I:30–42.
[3] Ponader S, Vairaktaris E, Heinl P, Wilmowsky CV, Rottmair A, Körner C, et al. J Biomed Mater Res A 2008;4:1111–9.
[4] Dinga R, Guo ZX, Wilson A. Mater Sci Eng A 2002;327:233–45.
[5] Lutjering G. Mater Sci Eng A 1998;243:32–45.
[6] Zeng L, Bieler TR. Mater Sci Eng A 2005;392:403–14.
[7] Cormeir D, Harrysson O, West H. Rapid Prototyping J 2004;10(1):35–41.
[8] Gaytan SM, Murr LE, Medina F, Martinez E, Lopez MI, Wicker RB. Mater Technol 2009;24(3):180–90.
[9] Parthasarathy J, Starly B, Raman S, Christensen A. J Mech Behav Biomed Mater 2010;3:249–59.
[10] Dinda GP, Song L, Mazumder J. Metall Mater Trans A 2008;39A:2914–22.
[11] Wu X, Liang J, Mei J, Mitchell C, Goodwin PS, Voice W. Mater Des 2004;25:103–9.
[12] Wu X, Liang J, Mei J, Mitchell C, Goodwin PS, Voice W. Mater Des 2004;25:137–44.
[13] Al-Bermani SS, Blackmore ML, Zhang W, Todd I. Metall Mater Trans A 2010;41A:3422.
[14] Baufeld B, Van der Biest O, Dillien S. Metall Mater Trans A 2010;41A(8):1917–27.
[15] da Silva SLR, Kerber LO, Amaral L, dos Santos CA. Surf Coat Technol 1999;116–119:342–6.
[16] Appolaier B, Héricher L, Gautier EA. Acta Mater 2005;53:3001–11.
[17] Lutjering G. Titanium. Berlin: Springer Verlag; 2003. p. 30. 33.
[18] Ahmed T, Rack HJ. Mater Sci Eng A 1998;243:209–11.
[19] Murr LE, Quinones SA, Gaytan SM, Lopez MI, Rodela A, Martinez EY, et al. J Mech Behav Biomed Mater 2009;2:20–32.
[20] Gil Mur FX, Rodríguez D, Planell JA. J Alloys Compd 1996;234:287–9.
[21] Thijs L, Verhaeghe F, Craeghs T, Humbeeck JV, Kruth J-P. Acta Mater 2010;58:3303–12.

Effect of Process Parameters Settings and Thickness on Surface Roughness of EBM Produced Ti-6Al-4V

A. Safdar[1,*], H.Z. He[1], Liu-Ying Wei[1], A. Snis[2] Luis E. Chavez de Paz[3]

1. Division of Materials Science, School of technology, Malmö University, SE-205 06 Malmö, Sweden.

2. Arcam AB, SE 43137, Mölndal, Sweden

3. Department of oral biology, Faculty of Odontology, Malmö University, SE-205 06 Malmö, Sweden.

Abstract:

Ti-6Al-4V is one of the most attractive materials being used in aerospace, automotive and medical implant industries. Electron beam melting is one of the direct digital manufacturing methods to produce complex geometries of fully dense and near net shape parts. EBM system provides an opportunity to built metallic objects with different processing parameter settings like beam current, scan speed, probe size on powder etc. Surface roughness of the test slabs produced with different parameter settings and thickness has been studied under confocal microscope. It has been observed that every part produced by EBM system has detectable surface roughness. The surface roughness parameter R_a varies between 1-20µm for different samples depending upon the process parameter setting and thickness. The Ra value increases with increasing sample thickness and beam current, and decreases with increase in offset focus and scan speed. Response surface methodology was used to develop a multiple regression model to correlate the effect of variation in EBM process parameters settings and thickness of parts on surface roughness of EBM produced Ti-6Al-4V.

Keywords: Ti-6Al-4V, EBM, Surface Roughness, R_a, Response Surface Methodology, Multiple Regression Model, Confocal Microscope,

1. Introduction:

Titanium and its alloys especially Ti-6Al-4V, are widely used engineering materials in many fields due to their excellent combination of mechanical and physical properties. One of their major areas of application is medical implant industry. Among the metallic biomaterials such as stainless steel and Co-Cr alloys, Ti and its alloys exhibit the most suitable characteristics for biomedical applications because of their better biocompatibility, specific strength, corrosion resistance and comparable young's modulus [1,2]. Their good biocompatibility by virtue of the excellent corrosion resistance and low toxicity, is the result of instant formation of oxide layer [3]. A key issue in materials used in dentistry and orthopedic implants is how material influences and, is influenced by the biological surroundings which results from the contact between the material and biological system [3,4]. The surface properties, surface chemistry, surface energy, topography and roughness of the implant material influence the initial cell response at the cell material interface, ultimately affecting the rate and quality of new tissue formation [5]. Higher levels of cellular attachments have been found on rough surface of titanium with irregular morphologies. Cell grown on rougher surfaces exhibited increased production of collagen,

prostaglandin E_2 and transforming growth factors β [5]. It has been found by Deligianni et al [5] that the human bone marrow can detect changes in roughness of the order of 0.6 μm. for the titanium dental implants Wennerberg et al has found that the surface roughness of about 1-2 μm has strongest bone response[6]. Surface roughness is also related to wear and friction property of the material and hence is related to the life time of the implant. Hence surface roughness is an important property of any material to be considered as biomaterial. The surface roughness of the material depends upon the manufacturing method [3,7], and environment and hence it is controllable either during fabrication or by post processing.

Direct digital manufacturing (DDM) is the next embodiment of solid free form fabrication (SFF), additive manufacturing (AM) or rapid Prototyping (RP). Different DDM techniques include direct light fabrication (DLF), LASER engineering net shape (LENS), direct LASER deposition (DLD) and electron beam melting (EBM). In all these methods metallic objects are produced directly from computer aided design (CAD) files by melting the metallic powder by utilizing focused high energy beam. EBM is one of such methods. EBM system has been described in details by [2,8,9].

One of the advantages of EBM or any DDM process is the possibility to build complex geometries like downward facing surfaces in cooling channels as single unit avoiding machining and welding etc. EBM process is very energy efficient and applicable to highly reflective materials like Aluminum [8]. The other advantages of using electron beam based DDM systems for fabrication of 3D metallic structures include purity of deposit due to controlled atmosphere, reduced segregation due to rapid quench rates, reduced heat affected zone due to small melt pools, verifiable deposition conditions due to imaging and feedback process control and possible 5-axis control [10]. The five controllable axes are the beam energy, scan speed, the offset focus (probe size on the powder) and 2D scanning on the powder bed. The above mentioned controllable parameters are jointly referred as the processing parameters of the system. As the quality standards require optimized set of processing condition for assurance of quality and uniformity of microstructures [2], The EBM or DLD process offers considerable potential with regards to the control of metallurgical structure and texture as multiple set of process parameter settings can be used [11].

In EBM systems each component/ part is build in two steps [8]. Firstly the outer part / boundary is melted and is referred as contour. The contour provides an interface between the actual build and the surrounding powder. A contour melting also provides an opportunity to have good surface structure. In second step of melting the actual part is build within the contours. This part is normally referred to as Squares. Contours are normally melted with relatively low scan speed and beam current than squares.

Roughness is the measure of the texture of a surface and is quantified by the vertical deviations of a real surface from its ideal form. There are many different roughness parameters used in literature. By convention every 2D roughness parameter is represented by ''R'' followed by additional characters in the subscript depending upon the mathematical/ statistical method used for calculation. R_a is defined as the arithmetic average of absolute values of each point's deviation from the mean line and is by far the most common parameter used to characterize the roughness. Other common characterizing parameters include, R_q (root mean square deviation), and R_{sk} (skewness) etc [12].

Confocal microscope (CM) has wide ranging applications in the field of biological micrography. The ability of CM to create an image with in-focus areas appearing as bright spots/ area while out of focus area as dark spots / areas, leads to its application in computation/ analysis of surfaces in materials science. The CM has the ability to obtain a series/ stack of optical sections, taken at different focal planes. Therefore CM can generate a "through-focus" image with "infinite" depth of field. This ability helps the confocal microscope in finding a unique role in imaging non-flat or translucent specimens. CM also has the ability to create topographic maps by constructing an image from a series of optical sections taken of a rough surface [13]. The actual surface area of the specimen can be estimated by geometric construction of the surface represented by the topographic map. Once surface area is computed, roughness of the surface can be characterized.

The objective of this study is to determine and understand the effect of part's thickness and variation in process parameter settings of EBM system on surface roughness/ topography of EBM fabricated Ti-6Al-4V metallic parts. A mathematical model based upon response surface methodology (RSM) is developed to study the variation of surface roughness with changing process parameter settings.

2. Materials and Methods:

2.1 Materials:

In this study four sets of rectangular test slabs each of contours and squares (Fig. 1) were produced by melting Ti-6Al-4V powder by using Arcam's S12 EBM system under different process parameter settings. Each set consists of three slabs of approximately 55x50 mm in two directions (x, y) (Fig. 1,2). Each test slab in the set is of different thickness (w). Each set has different process parameter settings as described in table 1.

To study the influence of different processing parameters, such samples are chosen that have similar build up environment, except the parameter of interest. The details of selected samples is listed in Table 2. Samples were obtained from two different planes of the slabs. The planes are illustrated in Fig. 2. Planes parallel to build direction were of major interest and accordingly the thin plane (of varying thickness) is marked as Surface one (S-I) and 55mm wide plane is marked as surface-II (S-II).

Surface roughness coefficients (R_a & R_q) of each as build surface of square and contour were quantified by using Nikon Confocal Microscope (CM) images and image analysis codes. Surface morphology of different test slabs was studied by using Nikon Elipse L150 Optical Microscope (OM) and EVOLS10 Environmental Scanning Electron Microscope (ESEM).

2.2. Methods:

In current study as build surfaces of samples were studied under Eclipse TE2000 inverted confocal LASER scanning microscope(CLSM) (Nikon Corporation, Japan), and EVOLS10 Environmental Scanning Electron Microscope (ESEM). For CM studies samples were stained with Propidium Iodide (PI). During the initial scanning an area of about $2cm^2$ from plane S–II was scanned thoroughly with 200x magnification. The

optical section of each scan was 639 x 639 µm^2. Comparison of the result obtained from all the optical sections revealed no significant difference in numerical value of R_a over the entire area of the sample. For the sake of optimization it was decided to obtain a representative area of each slab by scanning the surface in shape of 4x4 adjacent areas of 639x639µm^2. Hence the total representative area is about 6.25 mm^2. Each area is represented by a stack of about 20-40 pictures taken at different heights levels (slices) depending upon the surface/ area under study. The thickness of each slice was 10µm.
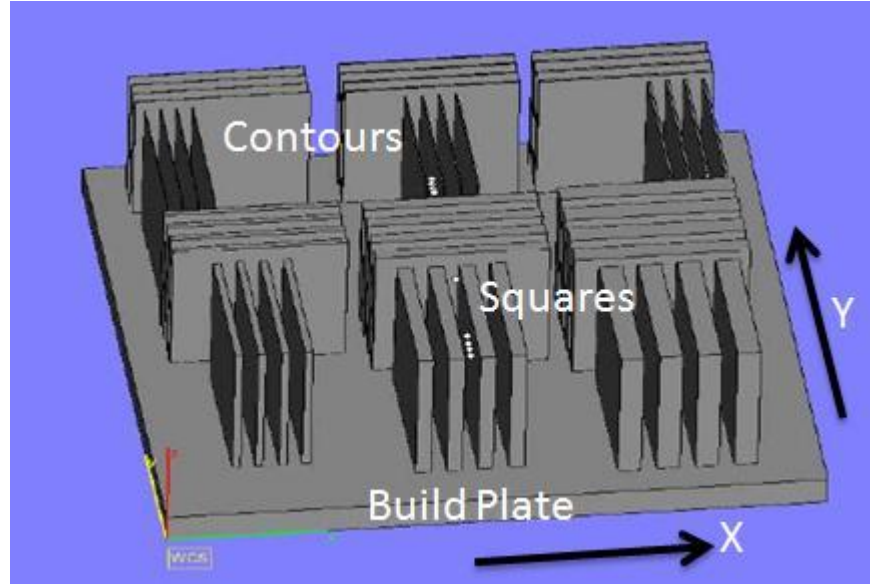
Figure 1. Schematic representation of Sample build up
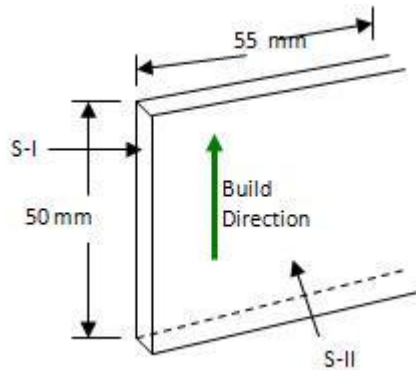
Figure 2. Schematic representation of test slab.

Table 1. Parameters settings of different test slabs

Theme/part		Scan Speed (mm/s)	Current (mA)	Offset Focus (mA)
Contour 1		250	4	10
Contour 2		250	6	10
Contour 3		250	4	25
Contour 4		250	6	25
Square 1	Contour	180	8	15
	Square	575	9	15
Square 2	Contour	180	8	15
	Square	650	9	15
Square 3	Contour	180	8	30
	Square	575	9	30
Square 4	Contour	180	8	30
	Square	650	9	30

Table 2. Selection of samples for comparative studies

S_No	Sample No	Width (mm)	Scan Speed (mm/ Sec)	Focus Offset (mA)	Current (mA)	Experiment
1	C1X2	2.09	250	10	4	Current
2	C2X1	2.10	250	10	6	
3	C1X1	1.29	250	10	4	Thickness
4	C1X3	1.59	250	10	4	
5	S1X1	3.50	$180^{*}/575^{**}$	15	$8^{+}/9^{++}$	Thickness
6	S1X3	7.42	180/575	15	8/9	
7	S3X3	7.42	180/575	30	8/9	Offset focus
8	S1X3	7.46	180/575	15	8/9	
9	S2X3	7.37	180 /650	15	8/9	Scan speed in squares
10	S1X3	7.42	180/575	15	8/9	

* Scan speed for the contour part   ****** Scan speed for the square part

\+ Beam current for contour part melting ++ beam current for the square part melting.

For quantitative analysis different Matlab routines developed by different scientists were initially tested but imageJ routine SurfCharJ plugin developed by Chinga et al 2003 [12] for supercalendered papers (SC) was found more suitable and consistent in results. The plugin is based on several developed routines for surface assessment, and provides global and local roughness analysis, gradient analysis, domain segmentation, surface leveling and directional analysis [12]. The plugin calculate roughness coefficient R_a and R_q by using the following equations respectively [12].

$$Ra = \frac{1}{N_x N_y} \sum_{i=1}^{N_x} \sum_{j=1}^{N_y} |z_{ij}|, \qquad R_q = \left[\frac{1}{N_x N_y} \sum_{i=1}^{N_x} \sum_{j=1}^{N_y} |z_{ij}|^2 \right]^{1/2}$$

While calculating the roughness coefficient value in both cases, the value was calculated for each picture in the stack. The average value of R_a or R_q for each stack is calculated and assigned to it. The average of 4x4 adjacent stack's average value was considered to be the representative value for each sample.

2.3 Response Surface Methodology (RSM):

Response surface methodology (RSM) is a collection of mathematical and statistical techniques useful for the modelling and analysis of problem in which a response of interest is influenced by several variables and the main object is to optimize this response [14,15].

A first order surface response model with "n" number of independent variable (x_1, x_2…,x_n) with single response "Y" can be expressed as fallows

$$Y = \beta_o + \beta_1 x_1 + \beta_2 x_2 + \ldots + \beta_n x_n + e$$

$$Y = \beta o + \sum_{i}^{n} \beta i \, xi + e \quad \text{(Where i= 1,2,…,n)}$$

The above equation is also known as first order or multiple regression model, where coefficients β_o, β_1,β_n are the regression coefficients. First order model is normally sufficient when the response is linear function of independent variables. The first order model approximation of any function is reasonable when the function is not too curved in the region and the region is not too big either [14]. If the response function is curve then second or higher order models are used.

In this study the experimental data obtained is used as inputs for the development of first order multiple regression model. The proposed linear model correlates the relationship between the surface roughness and the process parameters of EBM system.

3. Results:

3.1 Experimental Results:

In this study it was observed that every sample produced by EBM system has visible/ detectable surface roughness irrespective of parameter settings and thickness of the sample. Many granular partially melted powder particles were found attached to the surface. Fig. 3(a, b) is a SEM micrograph of the as built surface-II, showing partially melted powder or sintered powder attached to the surface. These powder particles are major contributor in producing rough surface. In surface-II (Fig. 3(a)) some valleys parallel to melt plate have also been observed. The width and depth of theses valleys is different at different points. The inter valleys spacing is much larger than the width of each deposited layer of powder during buildup process. A mountain-valley structure is observed in cross-sections of the samples which were cut parallel to build direction Fig. 4 (a-c), illustrating the overflow of molten pool.
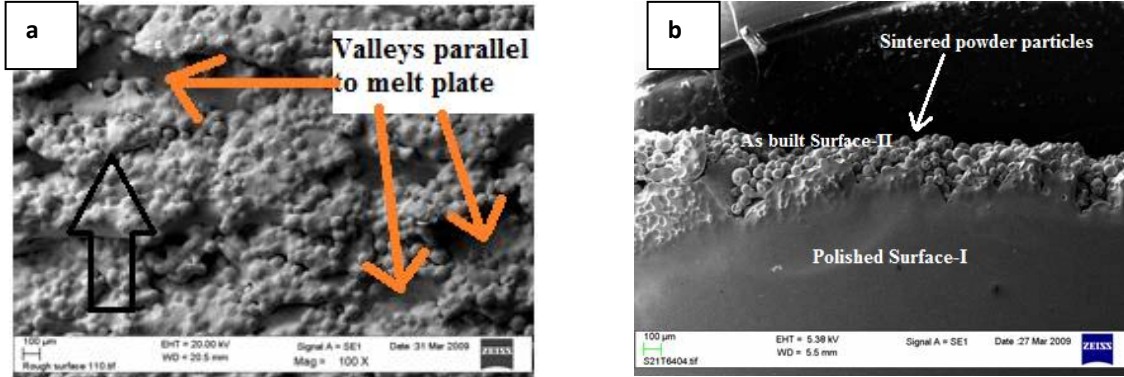
Figure 3. SEM micrograph of surface morphology of the as built slab a) as built S-II b) cross-section of S-I illustrating the partially melted powder particles attached to surface -II
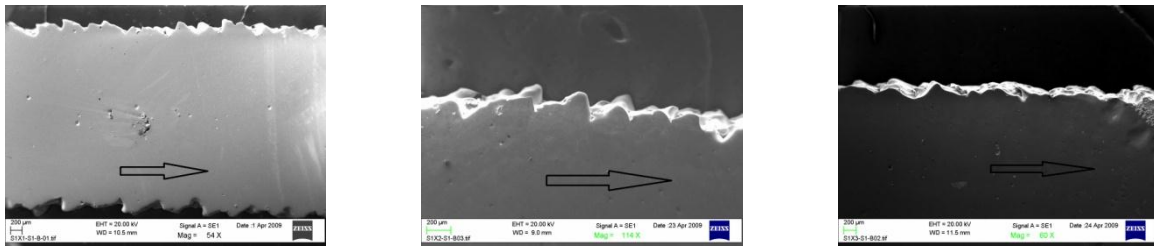
Figure 4: Cross section of the S-I illustrating inharmonic mountain-valley structure for sample with thickness of a) 3.5 mm;   b) 5.5 mm; c) 7.5 mm.

The quantification of surface roughness parameter R_a and R_q was done by using SurfCharJ plugin developed by Chinga et al [12]. The summary of the results is presented in table 3. The comparative results of each parameter are discussed afterwards.

Fig. 5 represents the R_a results graphically where the average value of R_a at different adjoining areas of the samples is plotted against the area numbers. For every sample sixteen (4x4) adjoining areas were selected as representative area for comparative studies. Different image processing softwares were used to reconstruct a representative 3D image of the actual surface presented in Fig. 6.

As in all the graphs presented in the Fig. 5 shows that for every area the value of R_a is always either larger or smaller than the R_a value of corresponding area of the other sample. This enables us to make a safe conclusion about which sample has comparatively higher or lower R_a or R_q value. The results of every parameter of interest are discussed below.

To study the effect of Thickness of slab on surface roughness, samples from both contours and squares were studies. Squares samples S1X2 and S1X3 were 5.5mm and 7.5mm thick respectively. The selected contours C1X1 and C1X3 were 1.3 mm and 1.6mm thick respectively. The average R_a value of S1X3 was 9.98μm while for S1X2 it is 4.25μm. Similar trend was observed in case of contours samples of C1X1 and C1X3. The average R_a values for C1X3 and C1X1 are 7.92μm and 17.25μm respectively. Therefore it can be concluded that with increasing thickness, the surface gets rougher.

To study the effect of beam current, offset focus and scan speed different samples were selected and studied. All these parameters have direct influence on the energy density of the melt pool which can be defined as the amount of energy per unit volume at particular time. The energy density of the melt pool increases with increase in beam current and decrease with increase in scan speed and offset focus. In this study it was observed that individual parameter effect is correlated to the energy density of the beam spot as increased energy density resulted in rougher surface.

To study the effect of beam current contour samples C1X2 and C2X1 built with beam current of 4mA and 6mA respectively were selected. The average R_a values for C1X2 and C2X1 are 4.45μm and 7.72μm respectively. Therefore the samples build with higher beam current or higher energy density have higher R_a value.

To study the effect of scan speed square samples S1X3 and S2X3 built with scan speed of 575 mm/sec and 650 mm/Sec in square regions respectively, were selected. The average R_a values for S1X3 and S2X3 are 9.98μm and 5.77μm respectively. Hence the sample build with higher scan speed or lower energy density has lower R_a and R_q values than the sample build with high scan speed.

To study the effect of offset focus contours C1X3 and C3X2, built with offset focus values of 10mA and 25mA respectively, were selected. The average R_a values for C1X3 and C3X2 are 17.25μm and 1.65μm respectively. Hence the low offset focus or high energy density resulted in a very high R_a value in comparison to high offset focus value.

Table 3. Summary of result for R_a and R_q calculations.

PARAMETER	Sample Name	Parameter Value	Avg. R_q (μm)	Avg. R_a (μm)
Thickness	S1X2	5.42 mm	10.57	4.29
	S1X3	7.42 mm	19.04	9.98
Thickness	C1X1	1.29 mm	18.85	7.92
	CIX3	1.59 mm	29.72	17.25
Current	C1X2	4 mA	12.07	4.45
	C2X1	6 mA	19.83	7.72
Scan speed	S1X3	575 mm/ Sec	19.04	9.98
	S2X3	650 mm/ Sec	12.98	5.77
Offset focus	C1X3	10 mA	29.72	17.25
	C3X2	25 mA	6.21	1.65
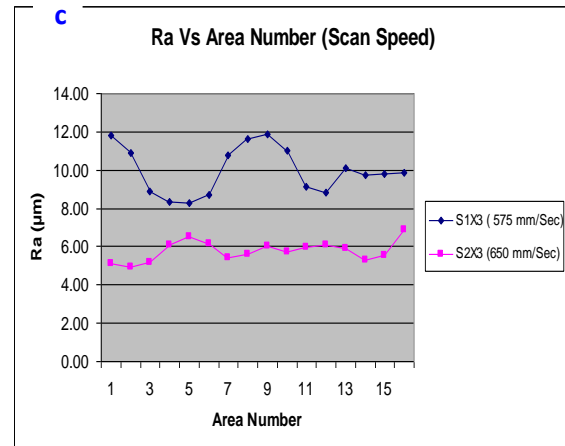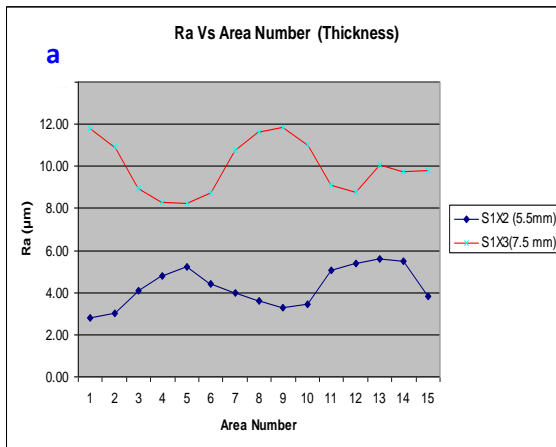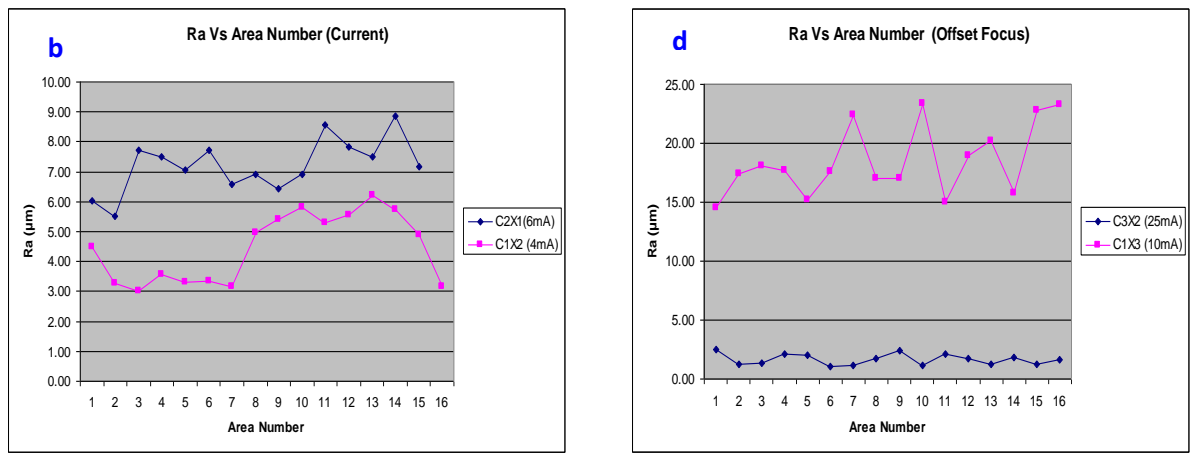
Figure5: Plot of R_a Vs area number for comparative study of two samples a) thickness of 5.42mm and 7.42 mm; b) current of 4mA and 6mA; c) scan speed of 575 mm/ Sec and 650 mm/ Sec; d) offset focus of 10mA and 25mA.
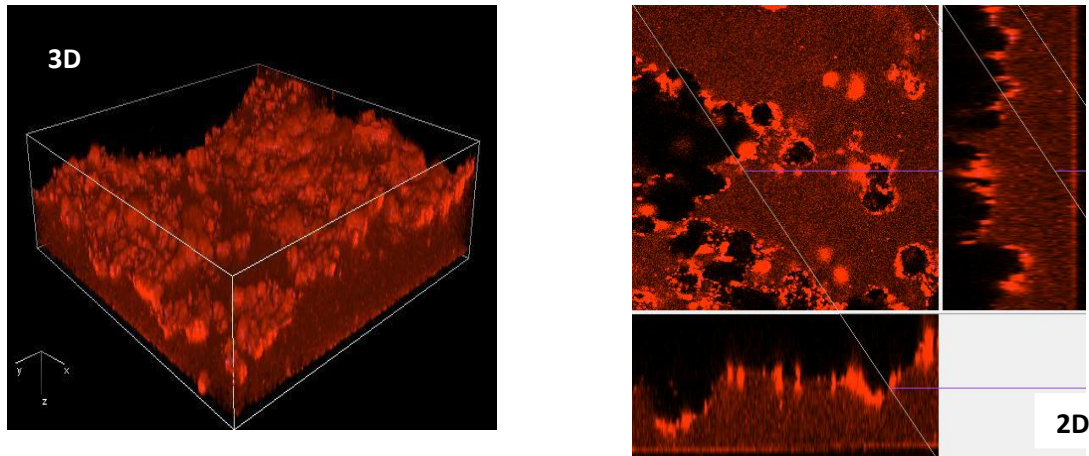
Figure 6: a) 3D reconstruction of surface topography (639 x 639 μm). b) 2D view of the surface at $X=X_i$ & $Y=Y_i$

3.2 Response Surface Method (RSM)

3.2.1 Model Calculations:

In general the multiple regression model in matrix form is written as [16] ,

$$y = X\beta + e$$

Where 'y' is a (qx1) vector of observations, 'X' is a (kxq) matrix of level of independent variables, 'β' is a (qx1) vector of regression coefficients and 'e' is an (1xk) vector of random errors. Where k is number of times experiment are repeated, and q = n+1 where 'n' is the number of independent variable in the system. If 'X' is a (q x q) matrix then the linear system $y = X\beta + e$ has a unique solution given by

$$\beta = (X^T X)^{-1}. X^T y,$$

10

and estimated regression equation is given as [16]

$$y = X\beta$$

The first order linear regression equation representing the surface roughness as function of sample thickness (A), beam current (B), scan speed (C) and offset focus (D), on the basis of above method can be written as

$$Ra = 4.85 + 7.8\,A + 4.2B - 10.5C - 0.5D$$

Fig. 7 presents the comparison between the experimental and model predicated values.

Comparison between the Experimental & Predicted Results
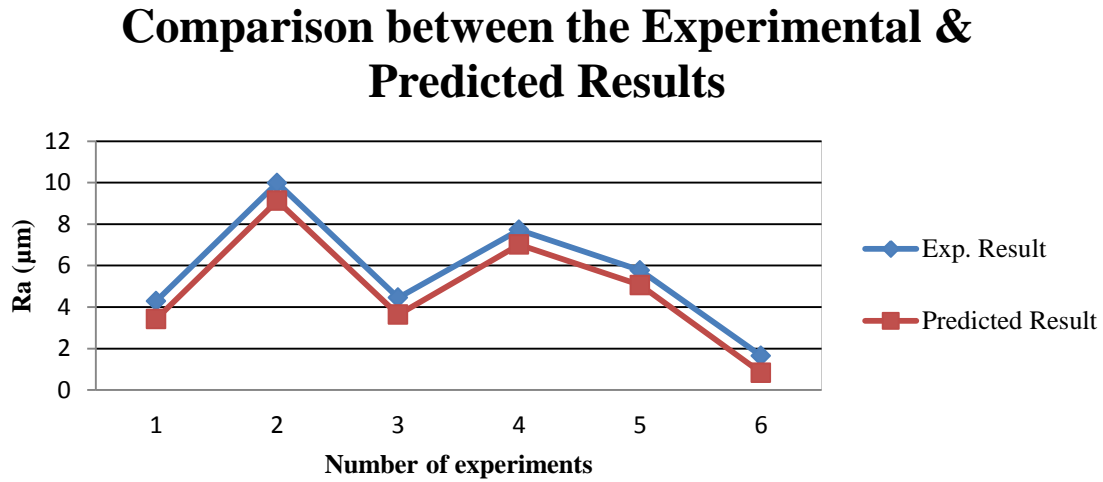
Figure 7: Comparison between the experimental and predicted results.

3.2.2 Model Adequacy Checking:

Model adequacy was checked by analysis of variance (ANOVA) and calculation of R^2 and adjusted R^2. R^2 lies in the interval [0,1] and measure percentage of the variation of 'y' around 'mean value of y'. More closer the value of R^2 to 1 , better the estimation of regression equation fits the sample data.

Results on ANOVA for the response function of the Ra are presented in table 4. The test for the significance of the regression is applied to determine if the relationship between the dependent variables y (Ra) and independent variable (A,B,C,D) exists. The proper hypothesis against which test were conducted are

H_O: $\beta_0 = \beta_1 = \beta_2 = \beta_3 = \beta_4 = 0$ Vs

H_1: $\beta_0 = \beta_1 = \beta_2 = \beta_3 = \beta_4 \neq 0$

Analysis were carried out for a significance value of 10%. The critical value of $F_{0.10,4,1}$ is 55.833 . As the calculated value of F (118.14) > $F_{0.10,4,1}$, therefore the H_o can be rejected therefore it imply that at least one of the independent variables contributes significantly to the model.

To check how well the estimated model fits the data is done by calculation of the value of R^2 and adjusted R^2 which are 0.997 and 0.989 respectively. As the values of both R^2 and adjusted R^2 are statistically significant for the response function therefore there is no sufficient reason to reject the proposed equation.

Table 4: ANOVA table for response function of the Ra

Source	DF	SS	MS	F	P
Regression	4	42.248	10.562		
Errors	1	0.089	0.0894	118.14	
Total	5	42.338			

4. Discussion:

Every sample produced by EBM systems has visible and detectable surface roughness. Similar results have been reported by S. Ponader et al and P. Thomson et al [3,6] for EBM built Ti-6Al-4V parts, by G.P Dinda et al [17] for DLD fabricated Ti-6Al-4V scaffolds and B. Vanddenbroucke et al [18] for selective laser melting method. Hence it can be said that rough surfaces are inherent feature of any DDM products. In all the above mentioned studies the reported R_a and R_q values are of the order of 20μm and 30μm respectively. In our studies it was observed that the R_a and R_q values vary for the samples of different thickness and for samples built with different parameter settings. The R_a and R_q values in our case are bit lower than the reported values in [3,17,18]. The possible reason for this difference could be the thickness of the samples, the samples used in [3,17] are thicker than our thickest samples and other build parameters are also not reported.

The possible sources of the rough surface of the DDM/ EBM produced parts can be attributed to many factors which are inherent of these powder based systems. One of the possible sources of rough surface is the sintered powder attached to the surface as shown in Fig. 3(a,b). In every powder based DDM system, there is always a lot more than required pre-heated powder available on the build table. The high temperature of the melt pool (~1900 °C) acts as the source of powder sintering. On the other hand this situation is same for every part built with different parameter settings, hence it cannot be the only source of difference between R_a values of different samples. This mechanism plays an important role in

producing a rough surface and the contribution of other factors like processing parameter's values are basically additive in nature.

The other factor which can be the possible source of rough surface is the size and energy density of the melt pool produced by the electron beam at the turning point for the scan i.e. the end of the build / part. The energy density (ρ) of the melt pool (watt Sec /m^3) is the function of beam power (P), scan speed (S.S) and offset focus. The energy density can be written as

$$\rho = \frac{P}{(S.S)(t)(h)}$$

Where 't' is the thickness (mm) of the added layer and *'h' (mm)* is the hatch spacing between two adjacent layers [18].

At the surface of build the melt pool acts like a source for the sintering phenomenon. Molten pool with high energy density enhances the sintering phenomenon by providing more energy. In this case sintering phenomenon can occur to many layers of powder particles in the vicinity that results in increased amount of sintered powder on the surface, thus resulting in rougher surface. Some overflow from melt pool at the surface also contributes in producing rough surface. Molten pool with high energy density also results in a bit bigger over flow and bigger mountain valley structure which contributes significantly to the roughness measurement. This over flowed melted metal appears as mountain-valley structure on solidification as shown in Fig 4(a-c).

The effect of high R_a value for samples produced by higher beam current and low scan speed and offset focus values can be explained on the basis of energy density of the melt pool. The higher beam current,   and low scan speed and offset focus results in melting pool of relatively high energy density. This high energy melting pool enhances the sintering phenomenon by providing more energy to sinter more powder from the surroundings. In the case of slow scan speed relative longer time at the turning point also contribute in sintering phenomenon. In the case of high offset focus the beam is not sharply focused and hence energy density of the pool decreases.

For the cases of difference in surface roughness due to sample thickness, it is due to the amount of total heat of the built, as the thicker gets the sample the amount of heat energy increase which is used as source for the sintering phenomenon.

RSM is found to be a successful technique to perform variation analysis of surface roughness with respect to variation in process parameter setting of EBM system. The first order multiple regression model found to be adequately represent the resulting surface roughness with experimental results. It is evident from the developed equation that increasing sample thickness and beam current results in increase of Ra value while same in scan speed and offset focus has decreasing effect, which are in accordance with the experimental observations. From the equation it is also evident that sample thickness, scan speed and beam

current have relatively more effect on roughness value then the offset focus. With the model obtained equation, a designer can subsequently select the best combination of sample thickness and process parameter values to achieve desired surface roughness.

Conclusion:

The process parameter settings and sample thickness have a strong effect on the surface roughness of the produced parts. The value of surface thickness variable R_a varies between 1-20μm for different samples, depending upon the process parameter setting and thickness. The surface roughness increases with increasing sample thickness and beam current, while it decreases with increase in offset focus and scan speed.

RSM is found to be successful technique to perform variation analysis of surface roughness with respect to variation in process parameter setting of EBM system. The first order multiple regression model found to be adequately represent the resulting surface roughness with experimental results.

References:

1. M. Niinomi, Mechanical biocompatibilities of Titanium alloys for biomedical applications, Journal of the mechanical behavior of biomedical materials I (2008) pp. 30-42.

2. L.E. Murr et al, Microstructures and mechanical properties of electron beam-rapid manufactured Ti-6Al-4V biomedical prototypes compared to wrought Ti-6Al-4V, Materials Characterization 60(2009) pp. 96-105

3. S. Ponader et al, Effect of topographical surface modification of electron beam melted Ti-6Al-4V titanium on human fetal osteoblasts, Journal of Biomedical Materials Research part A, 4(2008), pp. 1111-1119.

4. J. Lausmaa, Surface spectroscopic characterization of Titanium implant materials, Journal of Electron microscopy and related phenomena 81 (1996) pp. 343-361.

5. D.D. Deligianni et al, effect of surface roughness of the titanium alloy ti-6Al-4V on human bone marrow cell response and on protein adsorption, Biomaterials 22 (2001) pp. 1241-1251.

6. A. Wennerberg et al, Effect of titanium surface topography on bone integration : a systematic review, Clinical oral implant. Res 20 (Suppl 4),2009,172-184

7. P. Thomsen et al, electron beam melted, free-form-fabricated Titanium alloy implant: material surface characterization and early bone response in rabbits, Journal of biomedical materials research. Part B, Applied biomaterials, Vol 90B Issue 1(2009), pp 35-44

8. D. Cormeir et al, Characterization of H13 steel produced via electron beam melting, rapid prototyping Journal, Volume 10 number 1 (2004) pp 35-41

9. S.M. Gaytan, Advanced metal powder based manufacturing of complex components by electron beam melting, Material technology Volume 24 number 3 (2009), pp 180-190.

10. K. P. Cooper, Direct Digital Manufacturing with layer by layer melt deposition processes Supplemental proceedings Vol.1 TMS 2009.

11. A.N. Kalinyuk et al, Microstructure, texture and mechanical properties of electron beam melted Ti-6Al-4V, Material Science and Engineering A, 346 (2003), pp. 178-188

12. G. Chinga et al, Quantification of 3D microstructure of SC surfaces, Journal of Microscopy 227 (2007) pp. 254-265.

13. D.A. Lange et al, Analysis of Surface roughness using confocal microscopy, Journal of Materials Science 28 (1993), pp. 3879-3884.

14. D.C. Montgomery, design and analysis of experiments: response surface methods and design. New Jersy: John Wiely and Sons iInc. 2005

15. D. Pai et al, Application of response surface methodology on surface roughness in grinding of aerospace materials (6061Al-15Vol% SiC25p), APRN Journal of Engg. And applied Sciencies, Vol 5, No 6, 2010, pp 23-28

16. N. Braddely, The surface response methodology, M.Sc Thesis 2007, pp 8.

17. G.P. Dinda et al, Fabrication of Ti-6Al-4V scaffolds by Direct Metal Deposition, Metallurgical and Materials Transactions A 39A(2008) pp. 2914-2922.

18. B. Vandenbroucke et al, Selective laser melting of biocompatible metals for rapid manufacturing of medical parts, rapid prototyping Journal, Volume 13 number 4 (2007) pp 196-203.

Effect of Process Parameters Settings and Thickness on Microstructures of EBM Produced Ti-6Al-4V

A. Safdar[1*], Liu-Ying Wei[1], H.Z. He[1] , A. Snis[2]

1. Division of Materials Science, School of technology, Malmö University, SE-205 06 Malmö, Sweden.

2. Arcam AB, SE 43137, Mölndal, Sweden

Abstract:

In the current study the effect of sample dimensions and process parameters of EBM system on microstructure of the EBM built Ti-6Al-4V has been investigated using optical microcopy and scanning electron microscopy. The process parameter includes beam current, scan speed, offset focus and scan length. In general it was observed that the microstructures of EBM built Ti-6Al-4V consist of columnar grains of prior β phase. Inside the columnar grain typical (α+β) structures namely Widmanstätten α platelets with rod -like β phase formed on the interfaces of the fine α grains has been observed. Grain boundary α layer is found to be formed along grain boundary of prior β columnar grain. It has been found that with increasing thickness of the test slab, beam energy density and scanning length, the diameter of prior β columnar grain increases and they follow the build direction. The columnar grain diameter also decreases with increase in height. With increasing thickness and beam energy density α platelets get coarser.

Keyword: Ti-6Al-4V, EBM, process parameters, microstructure, SEM, OM

1. Introduction:

Over the past two to three decades, many solid freeform fabrication techniques have been investigated to fabricate fully dense and near net shape metal parts for variety of applications, in a way that material efficiency and lead-time are improved, targeting reductions in the cost of fabrication and lead-time compared to conventional methods. Direct Digital Manufacturing (DDM) is the next embodiment of solid free form fabrication (SFF), additive manufacturing (AM) or rapid prototyping (RP). Different DDM techniques include direct light fabrication (DLF), LASER engineering net shape (LENS), direct LASER deposition (DLD) and electron beam melting (EBM). The basic concept behind all additive manufacturing techniques is to take mass produced raw material, and through the use of an innovative processing technique, generate a finished component minimizing the use of specialized or dedicated tools. According to S.S Al-Bermani et al. (2010), In comparison to conventional methods all the DDM methods have the advantage of reduced material waste, shorter lead times, and minimum or zero tooling cost and most importantly high component complexity. Electron Beam Melting (EBM) is one of such DDM/ AM methods. According to D. Cormeir et al. (2004), EBM process is very energy efficient and posses' high coupling efficiency with deposited materials and thus applicable to highly reflective materials such as aluminum, and AM process also provides an opportunity to build complex geometries like downward facing surfaces and complex functional parts as a single unit, avoiding machining and welding etc. The free form nature of the AM methods

1

attracts the application in addition to conventional industries like medical implant, energy and aerospace, as well as in new fields of sports goods, modern art sculptures and fashion jewelry manufacturing.

L.E. Murr et al. (2009) have described the EBM system in details. EBM systems involve building of three-dimensional fully dense or near net-shape metallic structures/ objects in high vacuum environment. This process involves shaping a powder bed and selectively melting the powder to form a three-dimensional solid object, using high energy focused electron beam and multi-axis motion. In EBM systems each component/ part is build in two steps. Firstly the outer part / boundary are melted and are referred to as "Contour". The contour provides an interface between the actual build and the surrounding powder. Contour melting also provides an opportunity to have good surface structure. In the second step of melting the actual part is build within the contours. This part is normally referred to as "Squares".

Due to their excellent combination of mechanical and physical properties titanium and its alloys especially Ti-6Al-4V, are widely used engineering materials in aerospace, automotive, energy and medical implant industries. The mechanical properties of Ti-6Al-4V show strong dependence on the metallurgical microstructures. According to L. Zeng et al. (2005), the control of texture and microstructure is necessary to control the physical and mechanical properties of Ti-6Al-4V. Furthermore as discussed by G. Lutjering (2008), the microstructures of TI-6Al-4V are processing history and heat treatment dependent. This provides an opportunity to fabricate objects/parts with desired microstructures and mechanical properties by using a set of optimized fabrication process.

EBM process is a complex procedure depending upon different processing parameter of the system, ranging from beam power and size to scan speed and scanning direction / scanning strategy. The final microstructures of EBM built Ti-6Al-4V or any material are the result of complex combination of different processing parameters of the system. There is a possibility to obtain somewhat different microstructures in EBM built Ti-6Al-4V parts built with different set of processing parameters. This is possible due to the fact that the different set of processing parameters provides somewhat different built environment and cooling conditions. The thickness of the samples influences the heat flow during the initial and final cooling i.e. either cooling is done via the already solidified substrate or surroundings. The cooling rate in both cases is different as more rapid cooling is possible via the substrate than surroundings. The variation in beam current, scan speed and offset focus (beam spot size on powder bed) influence the energy density of the beam at any point at particular instance of time. The energy density of the beam is the function of beam power, scan speed and offset focus. The energy density increases with increase in beam power but decreases with increase in spot size and scan speed. The build is kept at around $700^{\circ}C$ until it is finished, this further leads to the fact that different parts of the same build have spent different time at this temperature, which can lead to different microstructures along the build direction.

As mentioned by L.E. Murr et al. (2009), the quality standards requires optimized set of processing condition for assurance of quality and uniformity of microstructures, the EBM or DLD process offers considerable potential with regards to the control of metallurgical structure and texture as multiple set of process parameter settings can be used. L.E. Murr et al. (2009), has compared the microstructures and mechanical properties of EBM built and wrought Ti-6Al-4V. S.M. Gaytan, et al. (2009), has discussed the microstructures of EBM built complex Ti-6Al-4V components. J. Parthasarathy et al. (2010) has studied the mechanical properties of porous titanium structure built with EBM method. Xinhua Wu et al. (2004) have studied the microstructures of Ti-6Al-4V produced by direct LASER fabrication methods. G.P. Dinda et al. (2008) have studied the microstructures, surface morphology and mechanical properties of Ti-6Al-4V scaffolds produced by direct Metal deposition method. The main focus of the above mentioned articles is to study the microstructures and mechanical properties; however the effect of variation in different process parameters on development of microstructures has not been studied to any great extent. In another similar study Xinhua Wu et al. (2004) and have studied the effect of different parameter setting of laser power, laser scanning rate and powder layer size of direct LASER fabrication methods on microstructures of Ti-6Al-4V components. L. Thijs et al. (2010) have studied the effect of laser power, scanning velocity (scan speed), powder layer thickness and hatch spacing on microstructures of Ti-6Al-4V fabricated via selective Laser melting. Studies similar to L. Thijs et al (2010) & Xinhua Wu et al. (2004), are missing for the Ti-6Al-4V produced via EBM. The object of this study is to investigate and understand the effect of different process parameters of EBM system such as beam current, beam offset focus, scan speed, on microstructures of EBM fabricated Ti-6Al-4V test slabs mainly by using optical microscope (OM) and scanning electron microscope (SEM).

2. Materials and Methods:

In this study four sets of rectangular test slabs each of contours and squares (Fig. 1) were produced by melting Ti-6Al-4V powder by using Arcam's S12 EBM system under different process parameter settings. Each set consists of three slabs of approximately 55mm x50 mm in two directions (x, y). Each test slab in the set is of different thickness (w).

The contours are thin slabs of various thicknesses ranging from 1-2 mm. Squares are relatively thick slabs in which both contours and squares are fully melted. The thickness of square slabs varies from 3.5-7.5 mm and is melted with relatively high scan speed and beam current. Process parameter settings are altered between the four sets according to the description in table 1. To study the effect of scanning length, samples of 10x10mm dimension and approximately 30mm high, were prepared from another build (see Fig 2).

In this study un HIPed and un-machined samples were studied. To study the influence of different processing parameters, samples were obtained from the slabs produced under different parameter settings. To reduce the influence of other parameters on experimental results, such samples were chosen that have similar build up environment except the parameter of interest. The details of selected samples are listed in Table 2. Planes parallel to build direction were of

major interest and accordingly the thin plane (of varying thickness) is marked as Surface one (S-I) and 55mm wide plane is marked as surface-II (S-II). The planes of a test slab are schematically illustrated in Fig. 3.
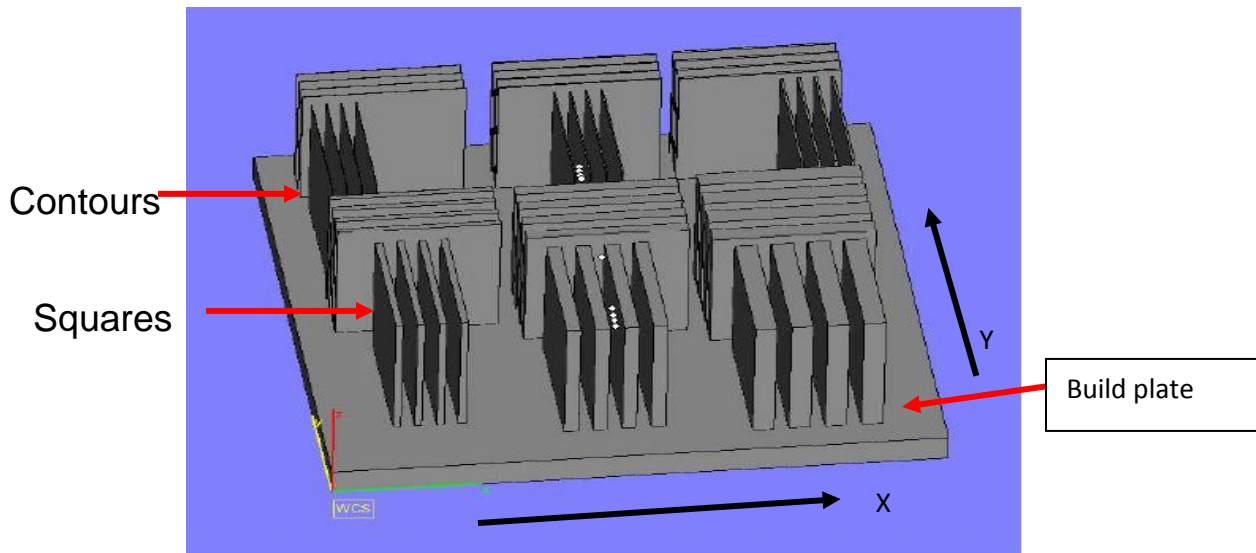
Figure 1: Schematic representation of **S**ample build up

Figure 2: Schematic representation of sample build up for scan length studies, scan length of a) 50mm   b) 10mm
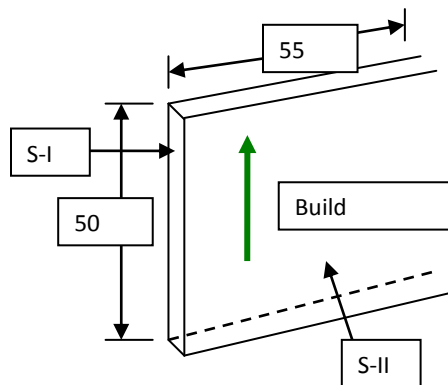
Figure 3: Schematic representation of test slab and placement of samples.

Table 1: Parameters settings of different slabs

Test Slab	Sample code	Scan Speed (mm/s)	Current (mA)	Offset Focus (mA)
Contour 1	C1	250	4	10
Contour 2	C2	250	6	10
Contour 3	C3	250	4	25
Contour 4	C4	250	6	25
Square 1 Contour	S1	180	8	15
Square		575	9	15
Square 2 Contour	S2	180	8	15
Square		650	9	15
Square 3 Contour	S3	180	8	30
Square		575	9	30
Square 4 Contour	S4	180	8	30
Square		650	9	30

Samples selected from different parts of the slabs for microstructure studies were prepared using standard metallographic procedures in similar conditions. Samples for optical and electron microscopic studies were first cut into 2mm thick slices of about 1cm^2 area. These slices were then step wise grinded mechanically under flowing water by using silicon carbide papers of grit size from 220 to 800 to get thickness of about 1.5mm. During the grinding, while changing to finer grit paper, the orientation of the sample was switched by 90° to remove the scratches left by previous paper. These samples were then electrochemically polished for 4-5 minutes duration by using Struers double jet unit using electrolyte A3 (600ml methanol, 360ml 2-butoxyethanol and 60ml perchloric acid). The electrochemical polishing voltage and average current was 35V and ~400mA respectively. Samples mounted on plastic epoxy, were grinded by using silicon carbide papers of grit size from 220 to 800 stepwise in same way as the small samples, but at the final step they were grinded with 9μm diamond suspension particles to obtain smooth surface. In the next step, the samples were mechanically polished with OP suspension containing 0.04 μm particles of Al_2O_3 in H_2O_2 with pH of 9.8, for different time durations depending upon surface conditions. The average time of OP polishing was about four to five minutes. In the final step all samples were chemically etched for different time durations of 2-7 minutes, by using Kroll's solution (01% HF + 02% HNO_3 + dis.H_2O).

Microstructures of different test slabs were studied by using Nikon Elipse L150 Optical Microscope (OM) and EVOLS10 Environmental Scanning Electron Microscope (ESEM) operating at accelerating voltage of 20 KV.

Table 2: Selection of samples for comparative studies

No	Sample Code	Width (mm)	Scan Speed (mm/ Sec)	Focus (mA)	Current (mA)	Placement on plate	Experiment
1	C1X2	2.09	250	10	4	X	Current
2	C2X1	2.10	250	10	6	X	
3	S1Y1	3.46	180*/575**	15	8+/9++	Y	Width
4	S1Y2	5.50	180/575	15	8/9	Y	
5	S1Y3	7.41	180/575	15	8/9	Y	
6	S1X1	3.50	180/575	15	8/9	X	
7	S1X2	5.50	180/575	15	8/9	Y	
8	S1X3	7.42	180/575	15	8/9	X	
9	S3X3	7.42	180/575	30	8/9	X	Offset Focus
10	S1X3	7.42	180/575	15	8/9	X	
11	S2X3	7.40	180 /650	15	8/9	X	Scan Speed in Squares
12	S1X3	7.42	180/575	15	8/9	X	

* **:** Scan speed for the contour part   ****:** Scan speed for the square part

+ : Beam current for contour part   ++: beam current for the square part.

3. Results:

3.1. Build Defects:

The EBM system due to its nature and mode of operations is susceptible to introduce many defects in the EBM built materials. The sources of these defects can be attributed to the poor beam control resulting in poor melting and undesired porosity. As the energy density of the beam depends upon different process parameter like beam current, offset focus and scan speed therefore variation in these parameters has the potential to vastly influence the build quality.

In this study more or less defect free built has been achieved irrespective of parameter settings. The only significant defects were observed in squares samples of S3 and S4, when the offset focus was changed from 15mA to 30mA. In this case the buildup with higher offset focus was not fully successful and sample was quite badly melted, and undesired porosity of about 11 vol % was observed (Fig. 4 a). Similar build defects have also been reported by S. M. Gaytan et al. (2009) for non optimized melting process parameters.

In addition to above mentioned build defect non-uniformly distributed spherical voids (pores) of 1-6µm in diameter have been observed in all micrographs (Fig. 4b). These pores are result of Argon (Ar) gas trapped in the gas atomized Ti-6Al-4V powder and can be removed by using standard HIP process for Ti alloys.
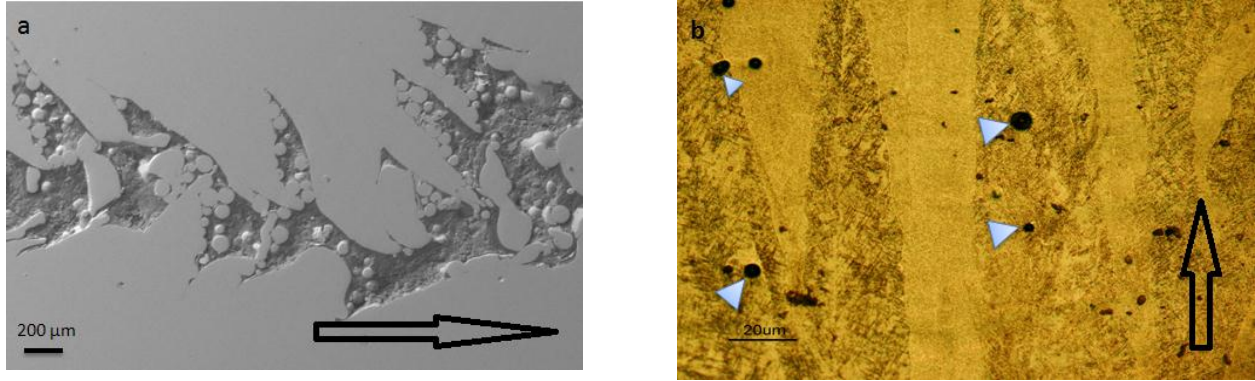
Figure 4: Example of build defects; a) undesired porosity and unmelted powder particles in sample built with offset focus of 30mA; b) non uniformly porosity due to trapped Ar gas marked with small triangles. (Build direction is marked by block arrow in all micrographs)

3.2 Microstructures:

In general the microstructures of EBM fabricated Ti-6Al-4V, consist of columnar grains of prior β phase growing along the build direction across multiple build layers and Widmanstätten α platelets. These microstructural features were observed in all samples irrespective of process parameter settings or thickness of test slab. The size, shape regularity and number of prior β columnar grains are different in samples built under different parameter settings and samples with different thickness. The summary of the microstructural observations is presented in table 3.

The microstructures inside the prior β columnar grains are typical of any (α+β) Ti alloy i.e. the Widmanstätten α platelets of different sizes and orientations, and the grain boundary α layer (α_{GB}) along the grain boundary of prior β grain are observed. The length of α platelets depends upon the diameter of prior β columnar grain. In general, the α platelets colony size is not uniform and very small, rather in majority of the cases α platelets are present in singular form.

The β phase formed in the transformed prior β grain in the EBM produced Ti-6Al-4V has been characterized by A. Safdar et al. by using Transmission Electron Microscopy (TEM). In EBM produced Ti-6Al-4V β phase appears as rod like structure formed on the grain boundary of the α platelets and generally grows along the build direction. The diameter of β phase rods is about 200 nm and is almost same in all the samples. The distance between two β phase rods varies between 0.5-2µm.

The difference observed in the microstructural observations can be attributed to the different factors affecting the microstructural development i.e. the geometrical effects, the power density of the beam and scanning strategy.

**Table 3:** Summary of microstructural observations:

Parameter	Sample code	Parameter value	Grain diameter (µm)	Grain boundary α thickness (µm)	Widmanstätten α platletes		Rod like β phase diameter (µm)
					Width (µm)	Length (µm)	
Thickness	S1Y1	3.5 mm	3-5	1	1-2	8-25	0.2
	S1Y2	5.5 mm	10-40	1-3	1-3	5-60	0.2
	S1Y3	7.5 mm	20-70	1-3	1-4	5-60	0.2
Current	C1X2	4 mA	2-13		1-2	60	0.2
	C2X1	6 mA	2-13		1-2	60	0.2
Scan Speed	S1X3	575 mm/Sec	5-50	1-3	1-4	40	0.2
	S2X3	650 mm/sec	6-35	1-3	1-4	20	0.2
Offset Focus	S1X3	15 mA	5-50	1-3	1-4	3-25	0.2
	S3X3	30mA	6-35	1-3	1-4	3-15	0.2
Scanning Length	SSL	10 mm	2-5	4	4	30	0.2
	LSL	50 mm	2-10	5	2	20	0.2

3.2.1 Geometrical effects:

To study the geometrical effect, microstructures of samples built with different thickness, and from different position across the build were studied. In general it was observed that with increasing thickness of the test slab the diameter of prior β columnar grain increases and microstructures become coarser. With the increasing thickness the prior β columnar grains get a more regular shape and have regular orientation along the build direction (Fig. 5(a-c)). It is also observed that with increasing thickness the number of prior β columnar grains increases, and in some cases especially in bottom part of sample more than one grains are so close to each other that they looks like a bunch growing parallel to built direction, as illustrated in Fig. 5c and Fig 7a. The columnar grains in the centre part of the slab seem more regular in growing direction i.e more or less parallel to build direction. While in the case of columnar grains near the surface and in the thinnest sample the growth direction often deviates from the build direction, see Fig 5 (a-c). Similar trends was observed when two surfaces of same built were compared, the wider surface (S-II) has characteristics of thicker sample in comparison to narrower surface, see Fig. 5c

and Fig. 7a. In thicker samples (Fig. 6 (a,b)) the grain boundary α phase ($α_{GB}$) is quite smooth and regular and α platelets are fairly regularly arranged, although the α platelets are longer and coarser in thicker samples. While the α platelets exhibits un even and wavy morphology in thinner samples, see Fig. 6a.

To study the effect of height along the build direction on the microstructure, Bottom part sample is taken from the area less than 5 mm above the start plate while the top part is from the area of slab at about 10mm of the top of test slab. It was observed that the diameter of prior β columnar grain decreases with the increase in height, and the bunch of columnar grains is quite big in bottom part, see Fig. 7(a,b).
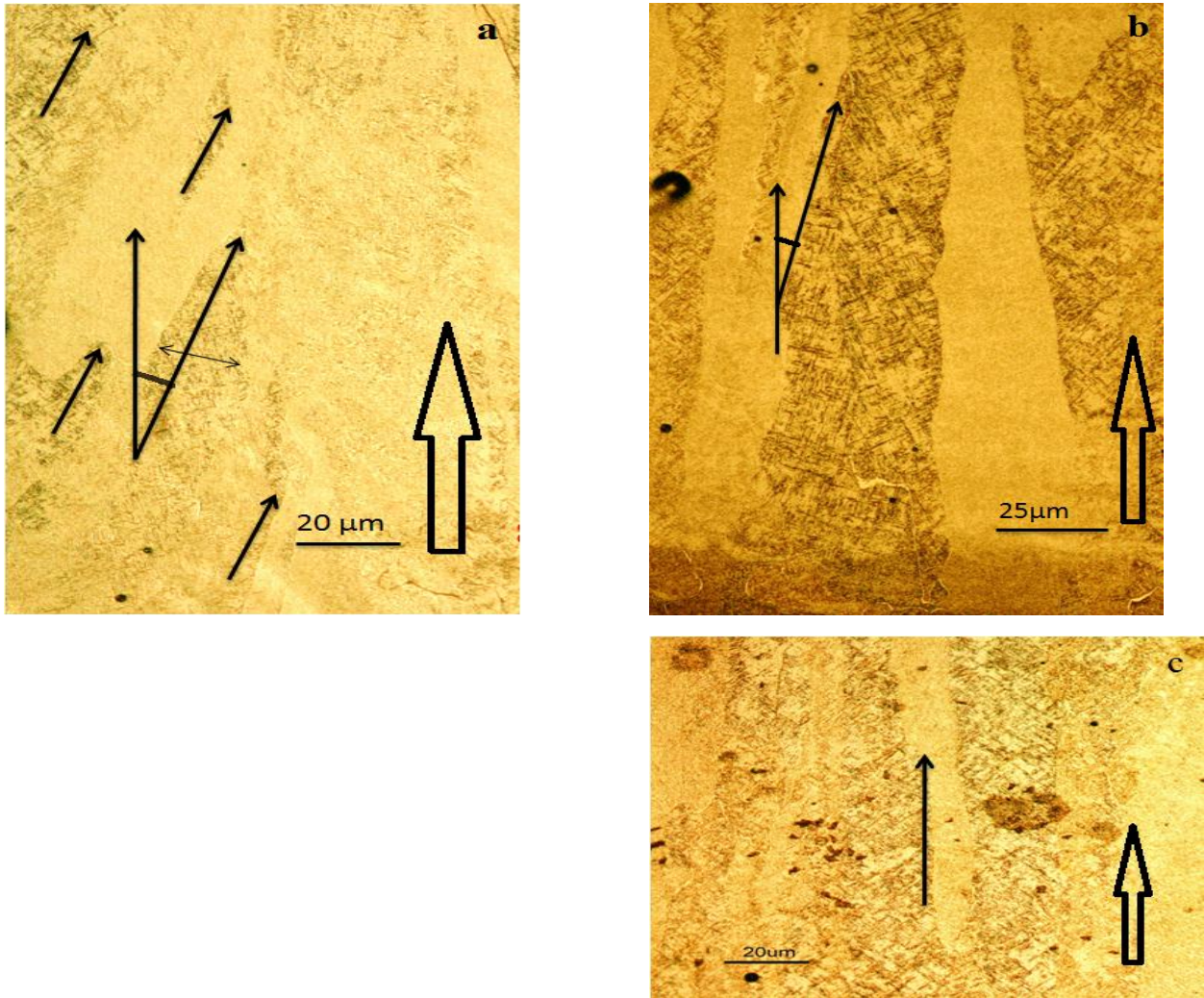
Figure 5: Optical Micrograph illustrating the general microstructures of S-I samples built with scan speed of 575 mm/sec, current of 9mA and offset focus of 15mA and with thickness of **a) 3.5mm, b) 5.5 mm, c) 7.5 mm.** (solid arrows indicates the growing direction angle of columnar grain in all optical micrographs)

9
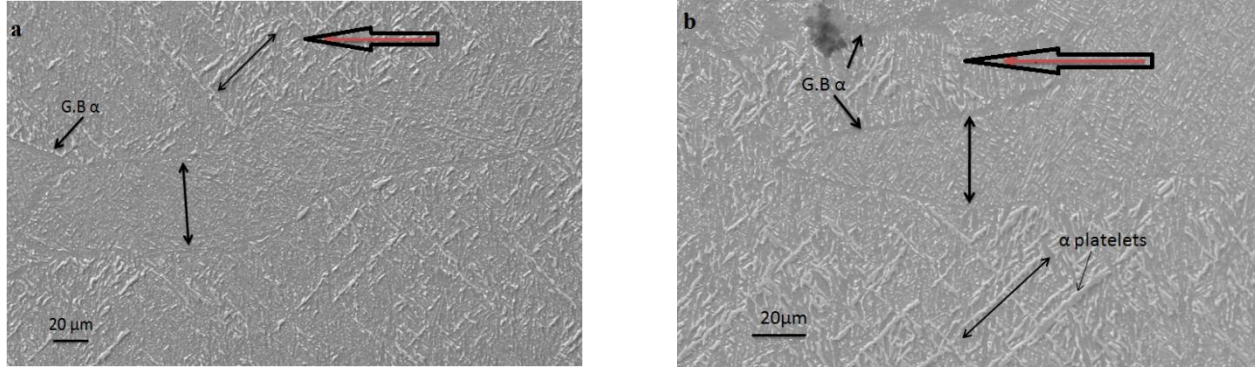
Figure 6: SEM (secondary electron image) micrographs illustrating the general microstructure in the top part of S-I of samples built with scan speed of 575mm/sec, beam current of 9mA and offset focus of 15mA and with thickness a) **5.5 mm, b) 7.5 mm.**(↔ : width of columnar grain and length of α platelets)
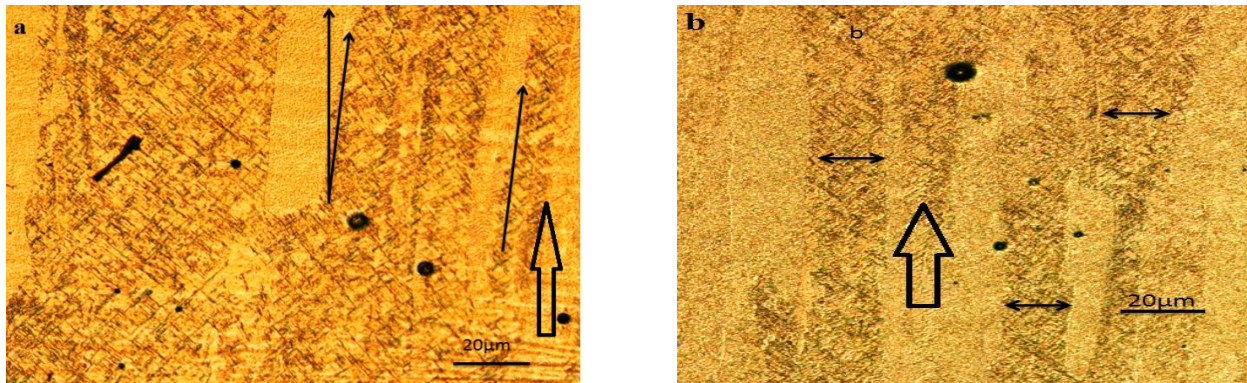
Figure 7: Optical micrographs illustrating the microstructures of the top and bottom part of **S-II** in the 7.5 mm thick samples build with beam current of 9mA, scan speed 575 mm/sec and offset focus of 15mA; a) Bottom part, b) Top part.

3.2.2 Energy Density of the Beam:

As discussed earlier, the energy density of the beam is the function of beam current, scan speed and offset focus. The energy density of the beam increases with increase in beam current but decreases with increase in scan speed and offset focus. Comparative study of microstructures was done for each individual parameter of current, scan speed and offset focus.

In general it has been observed that with increase in energy density the number of columnar grains increases (Fig. 8 a,b). The grain boundary α layer is smoother in sample with high energy density, see Fig 6b, but in case of low energy density the grain boundary α layer is wavy, see Fig. 9b. The bunch size of the columnar grain is higher for builds with higher energy density, See Fig. 7a and Fig. 8a. It has also been observed that with decrease in energy density the columnar grains are somewhat tilted (about 20°) in direction of scanning, while in case of higher energy density they follow the build direction (Fig. 7a & 9a).
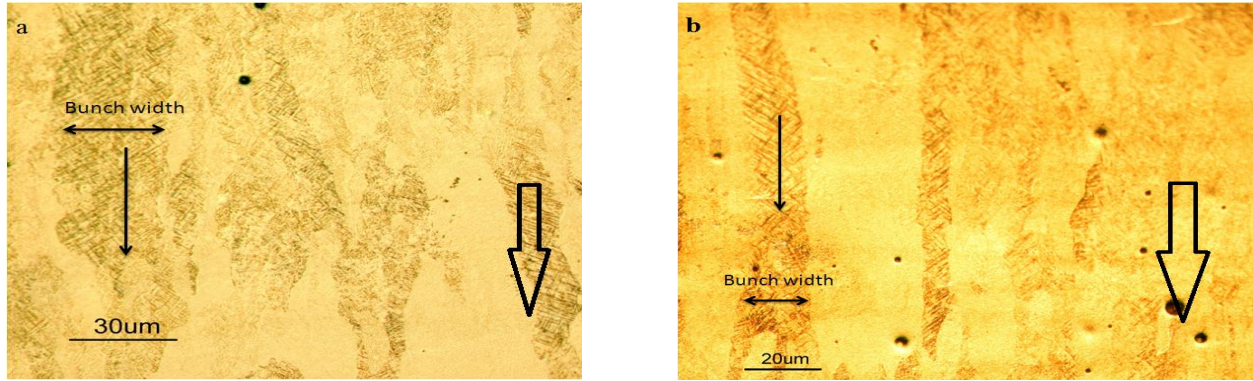
Figure 8: Optical micrographs taken from the bottom part of S-II of samples built with scan speed of 250 mm/s, offset focus 10 mA, slab thickness of 2.1 mm and beam current of **(a)** 6 mA (High energy density), (b) 4 mA (Low energy density).
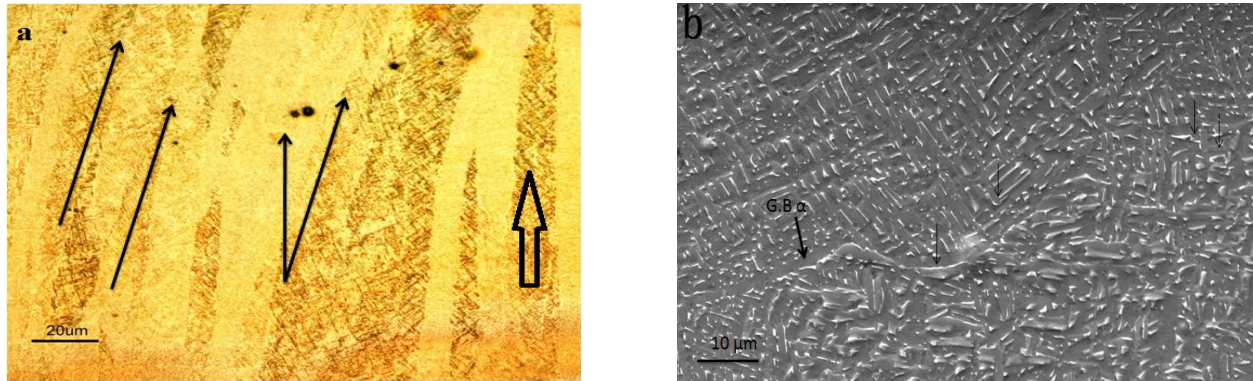
Figure 9: Micrograph illustrating the general microstructures in sample built with **low energy density** a) Optical, b) SEM.

3.3.3 Scanning length:

Fig. 10 is the optical micrograph of two samples produced with different scanning lengths, as illustrated in Fig2. From these optical micrographs it is evident that the scanning length has quite an effect on the size and geometry of prior β columnar grains. For the samples with short scanning length the grains are long but are not very thick and their diameter ranges between 2-5µm. While for the samples with long scanning length the geometry of the grains is quite irregular. The diameter of prior β grains varies irregularly along the build direction, in some cases the variation is as large as 10 µm. The respective grains boundaries in both cases are quite smooth and regular.

SEM micrograph in Fig. 11 illustrates the α+β microstructures in both samples. The thickness and length of α platelets increases with decrease in scan length, while the width of α_{GB} remains unaffected by scanning length. For the case of low scanning length in some cases relatively bigger α platelets colony size is observed.
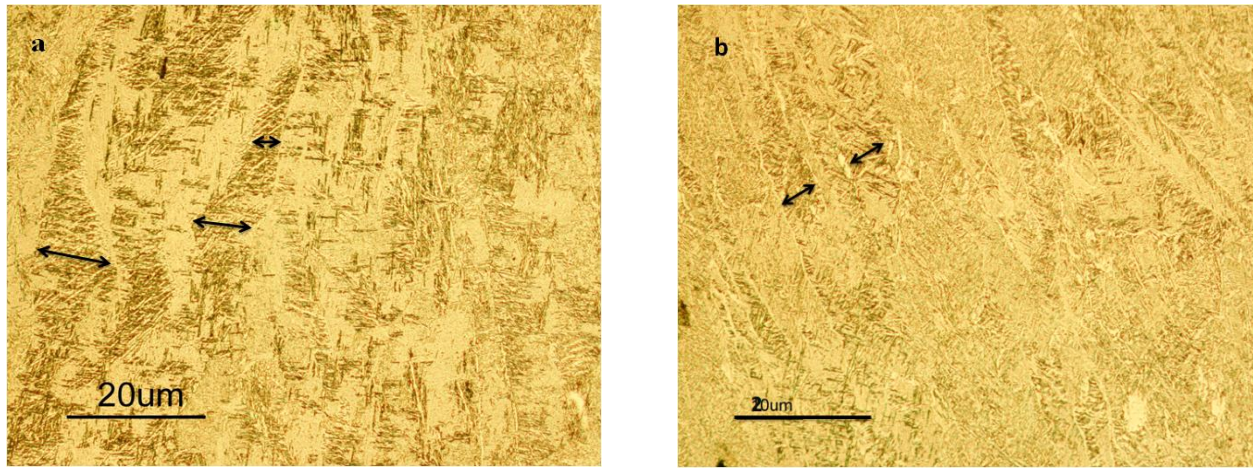
Figure 10: Optical micrograph illustrating the general microstructures of **S-II** the samples build with scan length of **a) 50mm b) 10 mm**
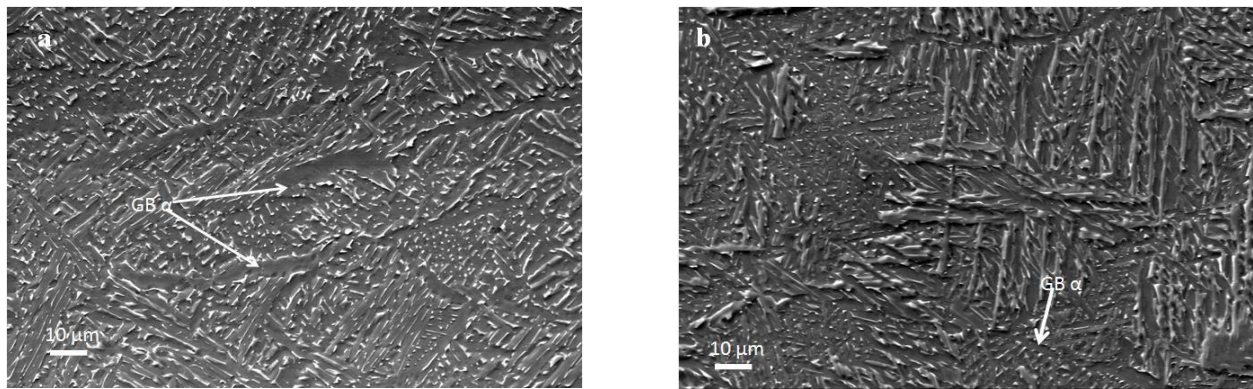
Figure 11: SEM micrograph illustrating the general microstructures of S-II the samples build with scan length a) 50mm b) 10 mm

4. Discussion:

The microstructures of Ti-6Al-4V alloys are heat treatment and processing history dependent. As mentioned by G.P. Dinda et al. (2008), It is very difficult to predict the microstructures of DDM produced metallic objects due to very complex thermal history. For EBM built Ti-6Al-4V, the phase transformation from liquefied temperature of about 1900 $^{\circ}$C to room temperature after the built is finished is a three-step procedure i.e. Rapid cooling from ~ 1900 $^{\circ}$C to 700 $^{\circ}$C , isothermal hold of the build at 700 $^{\circ}$C for entire duration of build and slow cooling from 700 $^{\circ}$C to room temperature.

The microstructures observed in all the cases are similar in general outlook and are dominated by columnar grains of prior β phase. Inside the prior β grains the α+β structure consists of widmanstätten α platelets and rod like β phase formed on the grain boundaries of α platelets. It has been observed in this study that the thickness and process parameter setting has

strong effect on the shape and size of columnar grain e.g. with increasing thickness of the sample the diameter and height of the grains increases and also has more regular geometry growing in parallel to the build direction. While considering the effects of process parameter settings the height and diameter of the prior β grain increases with increase in energy density which is function of scan speed, beam current and offset focus.

As concluded by L. Thijs et al. (2010) the heat conduction direction during the solidification determines the orientation of the prior β grain in Ti-6-Al-4V produced via selective laser melting method. Similar explanation can be used for the grains produced in EBm methods due to similarities in both methods mode of operation. The formation of columnar grain takes place during the initial rapid cooling i.e. this process happens at high temperature. The regularity in columnar grain's geometry depends upon the cooling rate, cooling path and melt pool size. In EBM or any AM process it is very difficult to keep track of heat transfer, therefore the exact heat flow path could not be determined. Hence it is difficult/ impossible to predict the exact location and size of prior β columnar grain. For different parameter settings and thickness of the sample, the difference in grain diameter and geometry can be attributed to the difference in heat transfer in each case. For the case of thinner samples due to immediate contact with the surrounding powder the columnar grains tends to tilt towards the outer sides of the build and deviation from build direction is observed. In thicker samples tiltation of grain near the surface is also due to the heat flow. In the case of thicker samples, due to relatively big size of the build, especially in the central part of the build the heat flow is only possible in one direction i.e. towards the base plate, and hence more straight columnar grains are observed. Due to multiple remeltings during addition of every new thin layer the columnar grains get more smooth shape and coarser microstructures are observed. Similarly in the case of builds with higher energy density, the builds exhibits larger and coarser columnar grains.

In the case of studying the effect of scanning length although the samples are thicker than the samples used for other process parameters setting study, the columnar grains observed in these samples are much thinner. Also in these samples no bunching phenomenon is observed which was usually observed in thicker samples. The scanning lengths in the case of other build cover across the whole melt plate which is about 150 mm. If we consider all the samples, it is observed that with increasing scan length the columnar grains become thicker and coarser. The reason for the difference observed is due to the fact that at turning point the scan speed of the beam is increased and hence energy density of the beam decreases. For smaller scan length this turning point area with low energy density beam, contributes significantly in total area of the build surface, hence smaller and thinner columnar grains are observed. In the case of long scanning length turning points are far away and almost all the build is built with relatively high beam energy density and hence thicker columnar grains and bunches are observed. The other possible reason for this difference is the time delay between the arrivals of successive beams. In short scanning length the time difference between two successive arrivals of the beam at certain point is very short and gives shorter time for the melt pool to solidified, while in case of long scanning length this time interval is bit longer. The long time delay between two successive

remeltings provides an opportunity for previous layer to get stable, and results in bit coarser microstructures.

According to B. Appolaier, et al. (2005) the formation of the grain boundary α and widmanstätten α platelets starts when the temperature drops below the β transus temperature. In the case of EBM built parts, due to the rapid initial cooling rate the very fine widmanstätten α platelets and small colony size have been observed. S.S. Al-Bermani et al. (2010) speculated that the martensitic phase could form when the alloy Ti-6Al-4V was rapidly cooled down to 700 ^{o}C from 1900 ^{o}C. If any martensitic phase α´ formed during the initial rapid cooling, the α´ phase would be unstable in the build due to long hold at 700 ^{o}C. During the isothermal hold at about 700 ^{o}C, tempering of the martensitic phase occurred, and α+β structure could formed. According to F.X.Gil Mur et al. (1996), the transformation from a martensite α´ to α+β phase at isothermal hold at 700°C in Ti-6Al-4V alloy is completed in about 30 minutes. The cooling rate for all the samples was identical and the test slabs were kept at 700°C for much longer than 30 minutes, therefore the final microstructures in the EBM produced parts should be α+β structure. The difference in length of α platelets is due to the different size of prior β columnar grains. The α platelets nucleate at grain boundary and grow up until these meet another α colony or platelets which originated from other nucleation site. Hence the maximum possible length of platelet is less than that of prior β grain, and α platelets of different lengths have been observed.

The β phase rods are also formed during the formation of α+β structures at isothermal hold when the temperature falls below the β transus temperature. Since the cooling rate and isothermal hold is similar for all samples in every build, no difference in diameter of the β phase rods is observed in all the samples irrespective of the thickness or process parameter setting.

In this study more or less similar microstructures inside of prior β columnar grains have been observed in all the samples irrespective of parameter settings. The only significant difference was observed when the offset focus was changed from 15mA to 30mA. In this case the build with higher offset focus was quite badly melted with undesired porosity of 11 vol%. In the case of other parameter settings the variation in setting was not big enough to introduce any significant difference. Therefore it can be said that the operational window used in this study is bit limited.

5. Conclusion:

The results of this study can be summarized as:

- Spherical voids (pores) of 1-6μm diameter have been observed in all samples due to the presence of Ar gas in gas atomized alloy powder.

- In general, microstructures of Ti-6Al-4V consist of columnar grains of prior β phase growing along the build direction. Inside the prior β grains the α+β structure consist of widmanstätten α platelets and rod like β phase formed on the boundaries of α grains.

- The height and diameter of prior β columnar grain is affected by the sample thickness and process parameter. The diameter of columnar grain ranges from 2µm to 70µm. The height and diameter of the prior β columnar grain increase with increase in thickness and energy density of the beam.

- The diameter of prior β columnar grains increase with increase in scanning length.

- The length of α platelets is in the range of 3-60µm for different samples depending upon the diameter of prior β columnar grain. In the samples having bigger and more regular columnar grain of prior β phase, the length of α platelets higher.

- In general the uniformity of microstructures inside the prior β columnar grains has been observed in all the samples irrespective of process parameter setting or thickness.

- The β phase appears as rod-like structure formed on grain boundaries of the α grain, with growing direction parallel to build direction in majority of the cases. The diameter of β rods is 0.2µm and is uniform in all samples irrespective of the sample thickness and process parameter setting. The distance between two parallel β rods is about 0.5-2 µm.

6. ACKNOWLEDGMENTS

References:

- A. Safdar , L-Y. Wei, A. Snis & Z. Lai , Evaluation of microstructural development in Electron Beam Melted Ti-6Al-4V, Materials Characterization 65 (2012) 8–1 5

- B. Appolaier, L. Héricher, E.A. Gautier, modelling of phase transformation kinetics in ti alloys – isothermal treatments, Acta Materialia 53(2005) 3001-3011

- B. Baufeld, Omer van der Biest and Steven Dillien, Texture and crystal orientation in Ti-6Al-4V builds fabricated by shaped metal deposition, Metallurgical and Materials Transactions A, 41A(2008) 1917-1927.

- Denis Cormeir, Ola Harrysson & Harvy West, Characterization of h13 steel produced via electron beam melting, Rapid prototyping Journal, Volume 10 number 1 (2004) 35-41

- F.X. Gil Mur et al, Influence of tempering temperature and time on the α´-ti-6al-4v martensite, Journal of Alloys and compounds 234(1996) 287-289.

- G. Lutjering, Influence of processing on Microstructure and mechanical properties of (α+β) titanium alloys, Material Science & Engineering A 243 (1998) 32-45.

- G.P. Dinda, L. SONG, and J. MAZUMDER, Fabrication Of Ti-6Al-4V Scaffolds By Direct Metal Deposition, Metallurgical and Materials Transactions A, 39A (2008) 2914-2922.

- J. Parthasarathy, B. Starly, S. Raman, A. Christensen, Mechanical evaluation of porous titanium (ti6al4v) structures with electron beam melting (ebm), Journal of Mechanical Behavior of Biomedical Materials 3(2010), 249-259

- L.E. Murr, E.V. Esquivel**, S.A. Quinones**, S.M. Gaytan**, M.I. Lopez**, E.Y. Martinez**, F. Medina **, D.H. Hernandez**, E. Martinez**, J.L. Martinez**, S.W. Stafford**, D.K. Brown**, T. Hoppe**, W. Meyers**, U. Lindhe & R.B. Wicker**, , microstructures and mechanical properties of electron beam-rapid manufactured Ti-6Al-4V biomedical prototypes compared to wrought Ti-6Al-4V, Materials Characterization 60(2009) 96-105

- L. Zeng & T.R. Bieler, Effect of working, heat treatment and aging on microstructural evaluation and crystallographic texture of α,α´,α´´ and β phases in Ti-6Al-4V wire , Material Science and Engineering A, 392(2005), 403-414.

- L. Thijs Frederik, Verhaeghe, Tom Craeghs , Jan Van Humbeeck, Jean-Pierre Kruth, A study of the microstructural evolution during selective LASER melting of Ti-6Al-4V, Acta Materialia 58 (2010) 3303-3312.

- S.M. Gaytan, L.E. Murr, F. Medina, E. Martinez, M.I. Lopez, R.B. Wicker, Advanced metal powder based manufacturing of complex components by electron beam melting, Material technology Volume 24 number 3 (2009), 180-190.

- S.S. Al-Bermani M.L. BLACKMORE, W. ZHANG, I. TODD, The origin of Microstructural diversity, texture and mechanical properties in electron beam melted Ti-6Al-4V, Metallurgical and Materials Transactions A, VOLUME 41A, 2010, 3423-3434

- Xinhua Wu, R. Sharman J. Mei, W. Voice , Microstructure and properties of laser fabricated burn-resistant Ti alloy, Material and Design 25(2004) 103-109

- Xinhua Wu Jing Liang, Junfa Mei, C. Mitchell, P.S. Goodwin, W. Voice , Microstructures of laser-deposited Ti-6Al-4V, Materials & Design 25(2004) 137-144

Phase field modelling of phase transformation in electron beam melted Ti-6Al-4V

A. Safdar[a], P. Ståhle[b,*], M. Fisk[a]

[a]*Malmö University, Division of Material Science, 205 06 Malmö, Sweden.*
[b]*Faculty of Engineering, Lund University, Division of Solid Mechanics, 221 00 Lund, Sweden.*

Abstract

Electron Beam Melting (EBM) is one of the additive manufacturing method. Ti-6Al-4V is one of the most used industrial alloys in high performance industries. EBM method due to its unique methodology provides different processing environments and heat treatments than conventional fabricational methods. In this study, phase field modelling approach has been successfully applied to study the microstructure development in Ti-6Al-4V produced by EBM method.

Keywords: Microstructure evolution, Cahn-Hilliard equation, Diffusion, Decomposition of martensite, EBM.

1. Introduction

High performance alloys used for aerospace, biomedical and other industrial applications are typically accompanied by high price tags. Over the past three decades, many solid freeform fabrication techniques have been investigated to fabricate fully dense and near net shape metal parts for variety of applications. The main focus of these technologies is to improve the material efficiency and lead-time compared to conventional methods. Direct Digital Manufacturing (DDM) is the next embodiment of solid free form fabrication (SFF), additive manufacturing (AM) or rapid prototyping (RP). Examples of DDM processes includes Electron Beam Melting (EBM), Laser Engineered Net Shaping (LENS), Selective Laser Sintering (SLS) and direct metal laser melting. These technologies represent a generation of processes that uses different energy beams, e.g. laser and electrons, to selectively consolidate metal alloy powders into parts having virtually any geometric shape.

---

*Corresponding author. Tel.: +46 46 222 3990
Email addresses: `adnan.safdat@mah.se` (A. Safdar), `per.stahle@solid.lth.se` (P. Ståhle), `martin.fisk@mah.se` (M. Fisk)

Titanium and its alloys - especially Ti-6Al-4V - are widely used engineering materials in aerospace, automotive, energy and biomedical industries due their excellent combination of mechanical and physical properties [1, 2]. Titanium is not a rare metal, but the high cost of processing titanium metal makes it to one of the candidate materials to be used in DDM process. In DDM processes the parts are built very close to their final shape, thus a very small amount of material is removed in finish machining, which improves the material efficiency and reduces costs of the process.

Microstructure plays an important role in determination of mechanical properties like strength, creep resistance, fracture toughness, etc. of alloys [3]. The microstructure of Ti-6Al-4V, like any other alloy, normally depends on chemical composition, processing history and heat treatment [4]. In order to simulate microstructural changes, A. SuaŽrez et al. [5] has developed a non-linear transient thermo-metallurgical model to study the phase transformation in Ti-6Al-4V fabricated by laser metal deposition by applying the finite element method. Y. Fan et al. [6], has developed a finite element model for the phase transformation in Ti-6Al-4V during laser forming. In [7], a finite element model which couples heat transfer calculations, phase transformation kinetics and internal stress calculations to simulate laser powder deposition of a titanium alloy is presented. The model was applied to study the effect of the deposition parameters on the microstructure, hardness and residual stresses. In [8], the authors have solved a detailed thermal model using the finite element method to obtain adequate knowledge for the optimization of EBM build process. The literature survey suggest that no attempt has been made to simulate the microstructure evolution in any one of the comercially available DDM methods by applying the phase filed modelling approach.

In this work, phase field modelling of microstructure development in EBM-built Ti-6Al-4V has been performed by using Cohn-Hilliard equation. A phase field model investigate the phase transition in a system by treating the system as a whole [9]. The temperature history plays an important role in the final microstructure and a martensitic phase has been observed during experiments for top layers in the build of small size. The temperature distribution inside the EBM build body is calculated in order to find the correct input data to the computational model. The modelled microstructure shows good agreement with observations.

2. Experimental procedures

In this section an overview of the working of EBM system and the resulting microstructures in Ti-6Al-4V will be presented. The figures are representative microstructures and the work has been done previously by the authors in the work [10].

2.1. EBM system

Electron Beam Melting (EBM) is one of the DDM methods. EBM process is highly energy efficient and posses' high coupling efficiency with deposited materials and is applicable to highly reflective materials. L.E. Murr *et al.* [11] and D. Cormeir *et al.* [12] have described the EBM system and process in details. This process involves shaping a powder bed and selectively melting the powder to form a three-dimensional solid object, using high energy focused electron beam and multi-axis motion. The advantages of using electron beam systems include purity of deposit, reduced segregation, reduced heat affected zones and the ability to achieve high component complexity.

The EBM system consists of an electron beam generating system (Electron Gun), a build chamber and a computer system to control the whole process. Electron Gun generates an electron beam of $\sim 500\,\mu$m in diameter and an energy density of $\sim 100\,\mathrm{kW/cm^2}$ [11, 13]. The beam is focused on the build table by electromagnet focusing lenses. During the build up process, an approximately $100\,\mu$m thin layer of powder of particle size of $40-100\,\mu$m is spread over the build table. The electron beam scans the powder bed multiple times with controllable speed known as scan speed. It is controlled by deflection coils according to a predefined Computer Aided Design (CAD) file. After successful melting of one layer, the build table is lowered according to the thickness of next layer ($100\,\mu$m). A new layer of powder is then spread over the lowered table and already built part. During the deposition and melting of a new layer, already solidified layers undergoes repeated heating and cooling, which results in multiple remelting and phase transformations depending upon their distance from the top layer. The phase transformation sequence in EBM built Ti-6Al-4V has been discussed by A. Safdar *et al.* [10]. The phase transformation in EBM built alloys can be summarized as a three step procedure:

1. Rapid cooling from approximately $1900\,^\circ$C to $700\,^\circ$C; with cooling rate in order of $10^3 - 10^5\,\mathrm{K/s}$ as estimated by [13].
2. Holding at the build temperature of approximately $700\,^\circ$C until the build is finished.
3. Slow cooling from build temperature to room temperature once the built is finished.

As discussed above, the multiple remelting and cooling of deposited layers plays an important role in determination of final microstructures of the finished part. Therefore, it is important to model and study the temperature distribution during the process to fully understand the parameters which effects the final microstructure. This is done is section 3.1.

2.2. Microstructure of EBM produced for Ti-6Al-4V

Ti-6Al-4V is a two phase alloy. It has room temperature microstructures consisting of Hexagonal Close Packed (HCP) α-phase and Body Centered

Cubic (BCC) β-phase. EBM is a complex process depending upon different parameters of the system, ranging from beam power and beam size to scan speed and scanning direction/scanning strategy. The final microstructures of EBM built material are the result of the complex combination of processing parameters of the system. The samples presented in this study is 5.5 mm thick and has been built with beam current of 9 mA, scan speed of 575 mm/s and an offset focus of 15 mA. Several studies has been conducted to discuss the microstructures of EBM melted Ti-6Al-4V like S.S. Al-Bermani *et al.* [13] and L.E. Murr *et al.* [11]. In general, microstructures consist of columnar grains of prior β-phase growing along the build direction. The $\alpha+\beta$ structure consisting of widmanstätten α-platelets and rod shaped β-phase, has been observed inside the prior β-grains [10]. Figure 1 is a Scanning Electron Microscope (SEM) image using Secondary Electron (SE), illustrating the typical columnar grain of prior β-phase and grain boundary alpha phase ($\alpha_{G.B.}$). Figure 2 is a Back Scattered Electron (BSE) image illustrating the rod shaped β-phase along with the α-platlet. According to [10] the Transmission Electron Microscope (TEM)/Energy Dispersive Xray (EDX) results shows that the weight percentage of vanadium (V) in the β-phase is approximately 30 wt.%, which is much higher then the average composition of the 4 wt.%. Whereas, the weight percentage of aluminum (Al) in the β-phase is about 2 wt.%, which is much below the average composition of 6 wt.%. Therefore, it can be assumed that the β-phase in EBM build Ti-6Al-4V is enrich of V and during the microstructure development V diffuses to the β-phase whereas Al diffuses out of the β-phase. In same study, the volume fraction (vol.%) for the rod shaped β-phase has been calculated to be approximately 3 %.
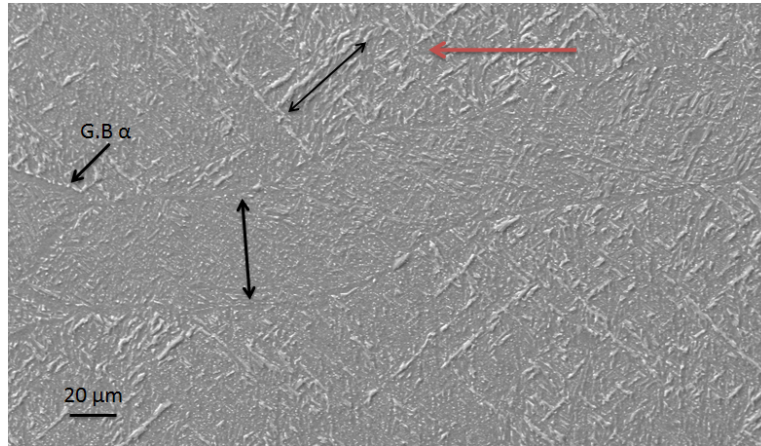

Figure 1: SEM/SEI illustrating general microstructure of EBM melted Ti-6Al-4V. Red arrow indicates the build direction and thick black arrow indicates the diameter of the columnar grain. Also the grain boundary alpha phase ($\alpha_{G.B.}$) is pointed out. The thin black arrow indicates the length of the alpha platelets.
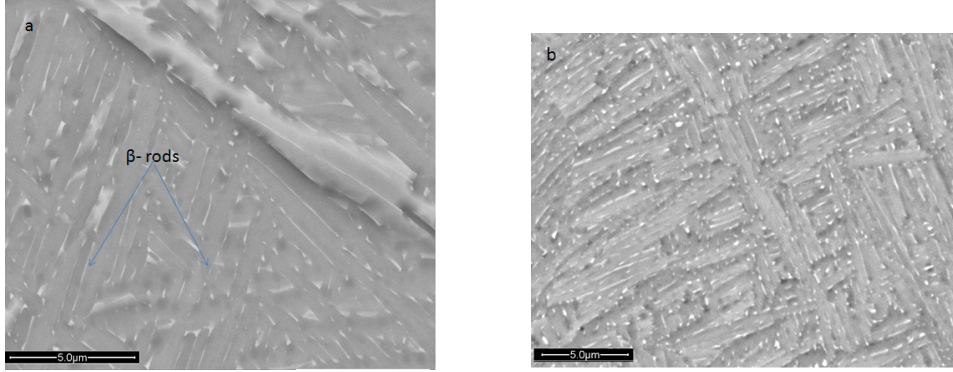
Figure 2: SEM/SBE image illustrating the β - phase rods and α - platelets; a) parallel to build direction; b) perpendicular to build direction.

3. Theoretical background

In this section, the steady state temperature distribution inside a semi-infinite body is solved in order to estimate the heat flow into the body during the melting process. The temperature history is used as boundary value during the simulation of the microstructure evolution. Theoretical background of phase field modeling is also presented.

3.1. Temperature distribution in the body

In the EBM system the energy source is in the form of a sharply focused electron beam that moves along the surface of the body. Therefore, the melting of the Ti-6Al-4V powder is confined to a small region as compared to the total built size. The heat flux and temperature distribution in the body is assumed to be governed by Fourier's laws of heat transformations. Combining these the transient temperature distribution inside a body can be computed from the equation [14]

$$\bar{\nabla} \cdot \lambda \bar{\nabla} T = \rho c_p \frac{\partial T}{\partial t} \, , \tag{1}$$

where λ, ρ and c_p are the thermal conductivity, the density and the specific heat capacity of the material respectively. The material is assumed to be homogeneous. Thus, it is obvious that the temperature distribution depend only on a single material parameter $\kappa = \lambda/\rho c_p$.

For the following analysis, the body is assumed to be semi-infinite and occupying the region $x \geq 0$ as is schematically represented in Fig. 3. Heating is assumed to occur in a semi-circular region that moves with a constant speed v along the body surface y. The heated region has the diameter d and its center is moving along the positive y-axis, so that its position at any

5

time t is given by $y = vt$ and $x = z = 0$. This constitutes a steady state condition.

The following relation

$$\frac{\partial}{\partial t} = -v\frac{\partial}{\partial y}, \tag{2}$$

eliminates time from Eq. (1), which can be rewritten as

$$\bar{\nabla}^2 T + \frac{v}{\kappa}\frac{\partial T}{\partial y} = 0. \tag{3}$$

By substituting $T = e^{-vy/2\kappa}R(x, y, z)$ in Eq. (3), the equation takes the form

$$\bar{\nabla}^2 R - \frac{v^2}{4\kappa^2}R = 0. \tag{4}$$

This equation is isotropic in the sense that it does not contain any directional variation. Further the boundary conditions, given by the point source that is stationary in the moving coordinate system as stated by Eq. (2), provide no directional variation. Thus, a solution of spherical symmetry is anticipated for R. The known solution to Eq. (4), for $R = R(r)$ where $r = \sqrt{x^2 + y^2 + z^2}$, is provided by [15],

$$R(r) = C_1\frac{e^{vr/2\kappa}}{r} + C_2\frac{e^{-vr/2\kappa}}{r} = 0. \tag{5}$$

In this case is $C_1 = 0$ since an influx of heat to the origin $r = 0$ is not expected. The resulting temperature distribution becomes

$$T(x, y, z) = C_2\frac{e^{-v(y+r)/2\kappa}}{r}. \tag{6}$$

The coefficient C_2 is given by the power of the heat source. A convenient way to obtain C_2 is to compute the energy stored in a thin disk far behind the moving heat source, e.g. at $x \geq 0$ and $y = y_s \to \infty$. Let the thickness of the disk be $v\mathrm{d}t$, where $\mathrm{d}t$ is a time increment. The heat energy stored in the disk is equal to the heat generated by the beam during the time increment $\mathrm{d}t$. The following relation is used

$$P\mathrm{d}t = \rho c_p \int_{-\infty}^{\infty}\int_{0}^{\infty} T(x, y_s, z)\mathrm{d}x\mathrm{d}z\, v\mathrm{d}t =$$

$$= \rho c_p \int_{0}^{\infty} C_2\frac{e^{-v(y_s+r)/2\kappa}}{r}\pi R\mathrm{d}R\, v\mathrm{d}t, \tag{7}$$

where $R = \sqrt{x^2 + z^2}$. Here $r^2 = y_s^2 + R^2$ implying that $r\mathrm{d}r = R\mathrm{d}R$, which gives

$$P\mathrm{d}t = \pi\rho c_p C_2 \int_{|y_s|}^{\infty} e^{-v(y_s+r)/2\kappa}\mathrm{d}r\, v\mathrm{d}t =$$

$$= 2\pi\mathrm{d}t\rho c_p C_2 \kappa e^{-v(y_s+|y_s|)/2\kappa} = 2\pi\mathrm{d}t\rho c_p C_2 \kappa \ \text{since}\ y_s \leq 0 \qquad (8)$$

The coefficient C_2 is determined to $P/2\pi\rho c_p\kappa = P/2\pi\lambda$. The temperature distribution becomes

$$T(x,y,z) = \frac{P}{2\pi\lambda}\frac{e^{-v(y-r)/2\kappa}}{r}. \qquad (9)$$

which is in agreement with the Rosenthal equation [13]. The above equation can be used to reconstruct the temperature history of each added layer of the material in the EBM process, see Fig. 3. The computed temperature history is used as an input to the phase field model, which is described below.
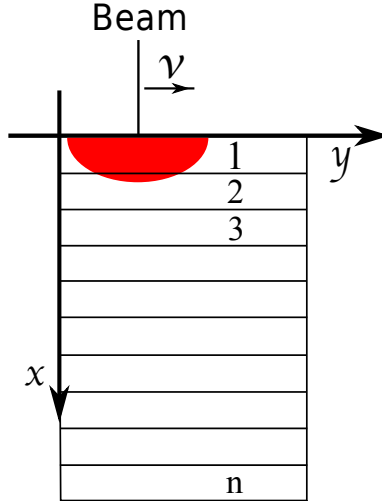

Figure 3: Schematical representation of the EBM process. The numbers represent each added layer of about $100\,\mu$m.

3.1.1. Phase field simulations

Microstructures are compositional and structural inhomogeneity that may consist of spatially distributed phases of different compositions and/or crystal structures. The microstructure evolution in a system takes place in such a way that the total free energy of the system is reduced [16]. Simulations of the microstructure evolution requires numerical methods. Conventional approaches known as sharp interface models treats the boundary between two compositional or structural domains as a sharp interface, over which a field variable varies discontinuously [9]. In an alternative approch, known as phase fiels modeles, the system is considered as whole irrespective

of the transition boudary. The phase field model uses a set of field variables that are continuous across the interfacial regions and their spatial distribution describes the microstructure in the material. In the intermediate phase the variable has a smooth transition between the values that describes the receptive phases. The phase-field method has emerged as a powerful computational approach to model and predict microstructure evolution in materials.

During phase transformation, Ti-6Al-4V changes from BCC structure β-phase to $(\alpha + \beta)$ phase at a transus temperature of about $995 \pm 5\,°\mathrm{C}$ [17]. In the EBM process this transformation occurs during the first rapid cooling. The microstructures of EBM built Ti-6Al-4V presented in section 2.2 indicates that the microstructural evaluation is a diffusion based process, in which the β-stabilizing element, i.e. V diffuses into the the β-phase and α-stabilizing element, i.e. Al diffuses out. This process can be simulated by using the Cahn-Hilliard equation, which models spinodal decomposition. In spinodal decomposition a homogeneous mixture of two or more components are separated into distinct regions representing each component. The Cahn-Hilliard equation can be written as

$$\frac{\partial \phi}{\partial t} = \nabla \cdot D \nabla \left(\frac{\partial f}{\partial \phi} - \varepsilon^2 \nabla^2 \phi \right) \tag{10}$$

where f is the double-well free energy function chosen to be

$$f = \frac{1}{2} a^2 \phi^2 \left(1 - \phi \right)^2 \tag{11}$$

where $\varepsilon^2 \nabla^2 \phi$ is the gradient energy term. ϕ represent the conserved ordered parameter of interest. The free energy term, f, affect the sharpness between the two distinct components, whereas the gradient energy term favor the intermediate value between two distinct components. In our studies ϕ represents the V in the range of $3 - 30\,\mathrm{wt.\%}$, which corresponds to the α- and β-phases in the alloy respectively.

4. Results and discussion

4.1. Temperature distribution in the body

The heat distribution in the body has been calculated for a set of process parameters in the range known as standard operating parameters. In this study, the beam power $P = 240\,\mathrm{W}$ corresponding to beam current of $4\,\mathrm{mA}$, the scan speed of $v = 575\,\mathrm{mm/s}$ and the beam diameter of $0.5\,\mathrm{mm}$ has been used. The time lag between two successive beams is $0.26\,\mathrm{s}$ for a built table of $150\,\mathrm{mm}$. Ten successive beam scans at a particular point are considered to be sufficient to melt the powder layer completely, which is followed by a holding time of 10 seconds. This delay is due to the addition of new powder

8

layer. The thermal and physical data used is presented in Table 1. The material parameter, κ, is $2.93\,\text{mm}^2/\text{s}$.

Equation (9) is used to estimate the temperature distribution when a new layer is added over the exciting structure. The results are presented in Fig 4. It is clear that layers just beneath the melted layer undergoes phase transformation as the temperature in second and third layer is over the β-transus temperature. The layers further down also experience multiple heating and cooling until a steady build temperature is attained and effect of new layer is negligible. In this study, the effect is tenth layers, which are $1\,\text{mm}$ beneath the melted layer.

Table 1: Physical data for Ti-6Al-4V used in computation of temperature distribution in the body.

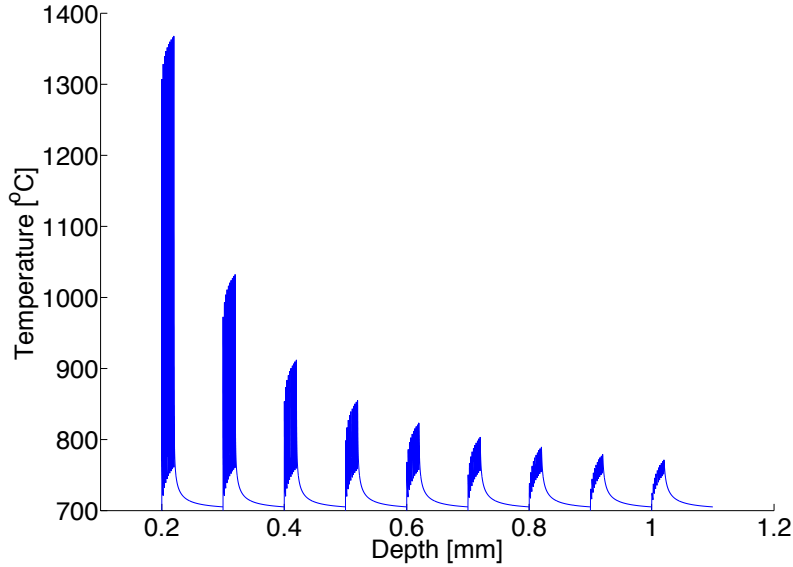| Physical/Thermal property	SI-units
Heat capacity, c_p	$530\,\text{J/kgK}$
Heat conductivity, λ	$7\,\text{W/m\,K}$
Density, ρ	$4507\,\text{kg/m}^3$

Figure 4: Temperature history from 2:nd to 10:th layer when a new layer is added. The small temperature peaks corresponds to the ten successive beams. The holding implies that the temperature almost drops to the build temperature of $700\,^\circ\text{C}$.

4.2. Phase field simulations

The microstructures in the deposited material is simulated using phase-field model. Each layer has experienced multiple phase transformations, heat

and cooling cycles as described in section 4.1. As the final microstructure of the Ti-6Al-4V are processing and heat treatment dependent, hence different parts in the build - especially the top layers - has experienced different holding time, which can result in somewhat different microstructures. Al-Bermani *et al.* [13] has reported the formation of martensitic structure in the top part of small sample of about 5 mm tall, due to less holding versus building time at 700 °C.

Three different simulated microstructures of the layer 1 mm beneath the melted layers are presented in Fig. 5; a) no annealing (zero holding time), b) annealing for 200 s at 700 °C and c) annealing for 1800 s at 700 °C. Thus, the layer has experienced multiple cycles of heating and cooling corresponding to Fig. 4 before achieving a stabile temperature of about 700 °C. The microstructure development is a two step process. In the first step of rapid cooling, the β-phase is transformed into a HCP α'-martensite phase [13], which is supersaturated in β-stabilizer V [17]. During the annealing, the α'-martensite phase decomposes into $(\alpha + \beta)$-phase. According to F. X. Gil Mur *et al.* [18], the decomposition of α'-martensite is completed in about 30 minutes for annealing temeperature of 700 °C.

The simulated microstructure agree very well with the observed microstructure. In Fig. 5 a), martensitic microstructures are shown, where none or very less diffusion has occurred due to rapid cooling. During the annealing process shown in Figs. 5 b) and c), diffusion based transformation to $(\alpha + \beta)$-phase takes place. The simulations has shown that plenty of martensitic microstructure is left after an annealing time of 200 s. The martensitic structure is fully decomposed after 30 minutes annealing. During the annealing process, the diffusion of V in Ti matrix follows Arrhenius law with an activation energy $Q = 165\,\text{kJ/mol}$ and a diffusivity constant $D_0 = 0.48 \cdot 10^{-6}\,\text{m}^2/\text{s}$ [19].
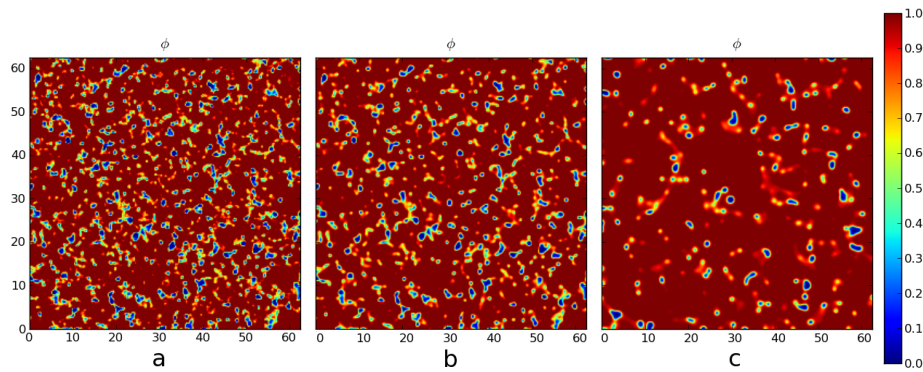

Figure 5: The evolution of the phase ϕ at the depth of 1 mm a) at 700 °C without holding time (rapid cooling) b) after annealing for 200 s at 700 °C c) after annealing for 1800 s 700 °C. The phase $\phi = 1$ corresponds to the composition of $V = 3\,\text{wt.}\%$ and the phase $\phi = 0$ corresponds to the composition of $V = 30\,\text{wt.}\%$.

5. Conclusions

The microstructure was studied in the EBM built Ti-6Al-4V using phase field modelling. The temperature history plays an important role in the final microstructure and a martensitic phase has been observed during experiments for top layers in the build of small size. This was successfully modelled by applying the temperature history onto the Cahn-Hilliard equation by solving the steady state temperature distribution inside the build when a new layer is added. This study has shown that it is possible to simulate phase transformations and microstructre development and can be modeled using Cahn-Hillard equation in phase field approch.

References

[1] M. J. Donachie, S. J. Donachie, Superalloys : a technical guide, 2nd Edition, ASM, Materials Park, 2002.

[2] C. Leyens, M. Peters, Titanium and titanium alloys: fundamentals and applications, Wiley-VCH, Weinheim, 2003.

[3] R. Ding, Z. Guo, A. Wilson, Microstructural evolution of a Ti-6Al-4V alloy during thermomechanical processing, Materials Science and Engineering: A 327 (2) (2002) 233 – 245.

[4] G. Lütjering, Influence of processing on microstructure and mechanical properties of $(\alpha+\beta)$ titanium alloys, Materials Science and Engineering: A 243 (1-2) (1998) 32 – 45.

[5] A. Suarez, M. Tobar, A. Yanez, I. Perez, J. Sampedro, V. Amigo, J. Candel, Modeling of phase transformations of Ti6Al4V during laser metal deposition, Physics Procedia 12, Part A (0) (2011) 666 – 673.

[6] Y. Fan, P. Cheng, Y. L. Yao, Z. Yang, K. Egland, Effect of phase transformations on laser forming of Ti-6Al-4V alloy, Journal of Applied Physics 98.

[7] A. Crespo, A. Deus, R. Vilar, Modeling of phase transformations and internal stresses in laser powder deposition, in: R. Vilar, O. Conde, M. Fajardo, L. O. Silva, M. Pires, A. Utkin (Eds.), XVII International symposium on gas flow, chemical lasers and high power lasers, Vol. 7131, 2009.

[8] M. Zäh, S. Lutzmann, Modelling and simulation of electron beam melting, Production Engineering 4 (2010) 15–23.

[9] A. A. Wheeler, W. J. Boettinger, G. B. McFadden, Phase-field model for isothermal phase transitions in binary alloys, Phys. Rev. A 45 (1992) 7424–7439.

[10] A. Safdar, L.-Y. Wei, A. Snis, Z. Lai, Evaluation of microstructural development in electron beam melted Ti-6Al-4V, Materials Characterization 65 (0) (2012) 8 – 15.

[11] L. Murr, E. Esquivel, S. Quinones, S. Gaytan, M. Lopez, E. Martinez, F. Medina, D. Hernandez, E. Martinez, J. Martinez, S. Stafford, D. Brown, T. Hoppe, W. Meyers, U. Lindhe, R. Wicker, Microstructures and mechanical properties of electron beam-rapid manufactured ti-6al-4v biomedical prototypes compared to wrought ti-6al-4v, Materials Characterization 60 (2) (2009) 96 – 105.

[12] D. Cormier, O. Harrysson, H. West, Characterization of h13 steel produced via electron beam melting, Rapid Prototyping Journal 10 (1) (2004) 35–41.

[13] S. Al-Bermani, M. Blackmore, W. Zhang, I. Todd, The origin of microstructural diversity, texture, and mechanical properties in electron beam melted Ti-6Al-4V, Metallurgical and Materials Transactions A 41 (2010) 3422–3434.

[14] H. S. Carslaw, J. C. Jaeger, Conduction of heat in solids, 2nd Edition, Oxford University Press, Oxford, 1959.

[15] G. B. Arfken, Mathematical methods for physicists, 3rd Edition, Academic Press, San Diego, 1985.

[16] D. A. Porter, K. E. Easterling, Phase transformations in metals and alloys, 2nd Edition, Chapman & Hall, London, 1992.

[17] G. Lütjering, J. C. Williams, Titanium, Springer, Berlin, 2003.

[18] F. G. Mur, D. Rodriguez, J. Planell, Influence of tempering temperature and time on the α'-Ti-6Al-4V martensite, Journal of Alloys and Compounds 234 (2) (1996) 287 – 289.

[19] J. Murdock, C. McHargue, Self-diffusion in body-centered cubic titanium-vanadium alloys, Acta Metallurgica 16 (4) (1968) 493 – 500.